FERMILAB-THESIS-2016-28

UNIVERSIDAD DE GUANAJUATO

División de Ciencias e Ingenierías Campus León

Neutrino - Electron Scattering in MINERνA for Constraint NuMI Flux at Medium Energy

Tesis que presenta

M.F. Edgar Valencia-Rodríguez

Para obtener el grado de
DOCTOR EN FÍSICA

Asesores de Tesis
Dr. Julián Félix,
Co-asesor Dr. Jorge Morfín

· December 2015 ·
Batavia, IL, USA

Operated by Fermi Research Alliance, LLC under Contract No. DE-AC02-07CH11359 with the United States Department of Energy

A mis padres, quienes sacrificando sus gustos y necesidades me han apoyado incondicionalmente.

Acknowledgments

This thesis would not have been possible without the help and support of many people. I would like to thank all of those who have contributed to the large amount of work that has made this thesis possible and those who have shared their knowledge and advise.

To Dr. Julián Félix, for give me the oportunity to participate on the MINERνA as a collaborator from Universidad de Guanajuato, and for help me to get support for my 2 year of stay at Fermilab, Thanks a lot Dr. Félix.

To Dr. Jorge Morfin, for give us the oportunity to stay at Fermilab for a long time, and for his advisory.

To Dr. Jaewon Park, for help me on my first steps on the MINERνA Data and MC analysis, for his useful advisory, for his technical recomendations and for everyting I learned in software.

To the MINERνA collaborators, for their advisory and useful comments.

To Rectoría General from the Universidad de Guanajuato for the financial support.

To Consejo Nacional de Ciencia y Tecnología (CONACyT), for the Beca Mixta that was used as ramp to get an long stay at Fermilab, and for the support emanated from the projects 223179, CB-2013-01 and Fondo SEP CONACyT.

I thank to my family. Thank you for your great support and and unlimited amount of understanding. No words can express my gratitude to you.

To my wife and our son, for their patience and motivation to continue moving forward.

To Dr. Trung Le, for his software help and for the interesting physics dis-

cutions.

To Latin American Group: Dr. Aaron Higuera, Dr. David Martinez, Dr. Kenyi Anapa and Dr. Laza Rakotondravoitia.

I would like to thank my committee for their patience and understanding regarding the lateness of this thesis and for their useful comments.

Abstract

MINERνA Experiment (http: // minerva.fnal.gov/), developed in Fermilab, studies the interactions between neutrinos and atoms, to determine the nuclear effects and the neutrino cross section of interactions,giving indications for the right development of the oscilation and dispersion neutrino theory. MINERνA is quasiacronim of Main Injector ExpeRiment:ν-A.

This work is centred to demostrate a tool to constrain the muon neutrino flux using neutrino electron scattering studies at the MINERνA Experiment in the medium energy; about 6 GeV Neutrino electron scattering helps to reduce flux normalization uncertainties on MINERνA′s absolute cross-section measurements. The electron is detected via an electromagnetic shower, produced by a single outgoing electron with a very forward angle.

We will describe how the single electron, and the expected signal events, are isolated using a simulation of neutrinos produced by the medium energy beam.

Contents

Chapter 1

INTRODUCTION

Particle physics is the study of fundamental properties of matter and interactions. It seeks to provide the ultimate answer to the questions "what is that made of?" and "how was it made?". The scattering of one particle by another has been one of the most successful tools in discovering answers to these questions and understanding the most basic building blocks of the universe.

Scattering has provided proof for the existence of increasingly fundamental constituents of matter: atoms $\rightarrow$ nuclei $\rightarrow$ nucleons $\rightarrow$ quarks. The Standard Model of particle physics is the most complete explanation of the subatomic universe, but it does not describe all phenomena.

The neutrino was postulated originally by Pauli in 1930, and since then, the neutrino has played a prominent role in our understanding of Nuclear and Particle Physics. From its postulation, scientist have detected and measured neutrinos from different sources, man made and natural.

From the experimetal evidences and some inferences that we can made from them, comes an understanding of how neutrinos interact with the matter. The correct knowledge of neutrino interaction cross sections is an important and necesary knowledge in neutrino measurement.

The main remarkable feature of neutrino electron scattering is that it is highly directional. The outgoing electron is emitted at very small angles with respect to the incomming neutrino direction.

Experimentally, neutrino electron scattering measurement is a very dificult task, due to the smallness of its cross section ($\sim 10^{-42}\text{cm}^2$) and to the presence of abundant competing background processes which cannot be totally eliminated on an event by event basis.

1.1 The Standard Model

Around of 1973-1974, the ideas put forward earlier by Weinberg and Salam and by Glashow, on electroweak unification gradually led to the formulation of the so-called Standard Model. It explains three of the four observable forces: the electromagnetic, strong, and weak forces, and defines 16 fundamental particles. There are three types of particle: bosons, quarks, and leptons. On the Figure 1.1 are shown the Familie of Particles on the Standard Model.

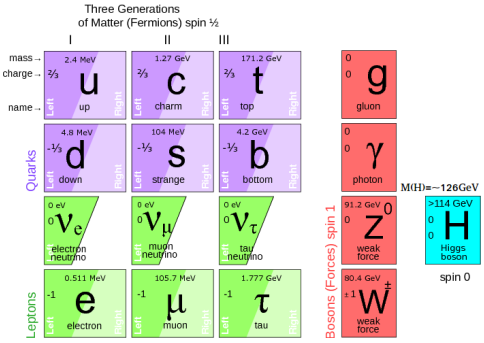

Figure 1.1: The Standard Model is a kind of periodic table of the elements in particle physics.

The Lagrangian Model is based on the gauge group $SU_2 \times U_1$. The left-handed fermions from SU_2 doublets, while the right-handed fermions are in SU_2 singlets. Of the four original gauge fields, three acquire mass by the spontaneous breaking of gauge symmetry, via the Higgs mechanism, and become the massive W^+, W^- and Z^0 bosons.

One of the original gauge bosons, which is left massless, is identified with the photon. The fermions of the theory are the leptons and the quarks. The theory would have triangle anomalies unless the fermions in the theory had appropriate hypercharges such that all the anomalies cancel among themselves.

The hypercharge assignments are such that cancellation of anomalies does indeed take place. The fact that the quarks carry color is irrelevant for the electroweak sector; in summing over the colors, one gets only a numerical factor for the number of colors. Quarks and leptons are fermions, which have half-integer spin.

There are 6 quarks and 6 leptons, which come in pairs that are repeated for three generations. The quark generations are up (u) and down (d), charm (c) and strange (s), top (t) and bottom (b). There two types of leptons: charged and neutral (electron, muon, tau; electron neutrino, muon neutrino, tau neutrino). See Figure 1.1. For each of these particles there is an antiparticle.

The lepton generations are electron (e) and electron-neutrino (ν_e), muon (μ) and muon-neutrino (ν_μ), tau (τ) and tau-neutrino (ν_τ). For each one of the fermions, exists an anti-particle that carries the opposite quantum numbers [2].

The quarks also have strong interactions. For dealing with this part, use was made of the Lagrangian for QCD wich was avaliable from the work of Fritzsch, Gell-Man and Leutwyler and Gross and Wilczek and Politzer. Since QCD is also renormalizable, adding it to the electroweak theory produced a renomarlizable gauge field theory wich is capable of dealing with electroweak and strong interaction. This is the Standard Model [1].

Calculations of strong interactions corrections to electroweak theory, called QCD corrections are feasible in the realm of high energies where the strong interaction effects are small, due to the asymptotic freedom of QCD, and perturbation theory can be used. The time was ripe for mounting experiments to test the predictions of the standard model.

The Standard Model cannot explain all observed phenomena. The most obvious shortcoming is that it does not attempt to explain gravity. But the Standard Model also fails to explain some subatomic behavior, although was constructed to do so.

1.2 Neutrino History

Even since the early days of discovery of β radioactivity, several people were involved with further investigations of the properties of the β particles. It was discovered that β particles of both signs (electrons and positrons), are emitted in β decays.

Early crude measurements of β^- energy, by absorving them in thin foils, showed to be electrons. The energy measurements of β particles were continually improved by construction of magnetic spectrometers an other methods.

At the same time, progress was being made in more precise measurements of

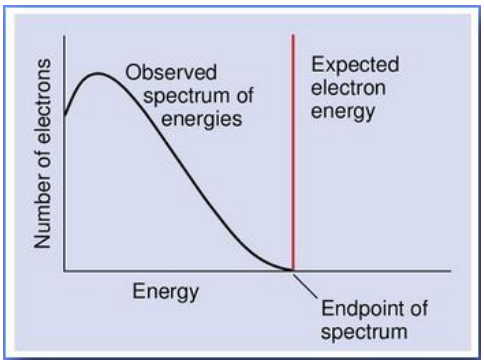

Figure 1.2: Beta decay energy spectrum [5].

atomic masses using mass spectrographs. It was established from a number of such measurements that although the nucleus undergoing the β transformation was in a definite state and the product nucleus was in a definite state, so the emitted β particle had a continuous distribution of energies.

Measurements showed that the energies of the β particle continuosly ranged from very low energies to a maximum energy E_{Max}, (the end point energy of the β spectrum), where E_{Max} is equal to energy difference between the parent nuclear and the product nuclear states. This observations were very puzzling, because it seemed to imply lack of energy conservation in this process. In the Figure 1.2 is showed the β decay energy spectrum.

By energy and spin conservation, the decay was believed to be a two-body process,

$$n \to p + e^- \quad \text{then} \quad E_e \frac{m_n^2 + m_e^2 - m_p^2}{2m_n}, \tag{1.1}$$

where E_e is the energy of the ejected electron in the rest frame of the neutron and m_n, m_p, and m_e are the neutron mass, proton mass, and electron mass [5].

Pauli on 1930, who was not willing to abandon the energy conservation, came up with the idea that possibly a neutral invisible particle is emitted along with the β particle. Originality Pauli called "neutrons" to this particles.

He suggested that the two particles together share the energy difference between the initial and the product nucleus consistent with the conservation of energy and momentum. If such a neutral particle did indeed exist, its mass, as deduced from the energy distibution of the β particles at the end point, showed that it was consistent with being zero within experimental errors.

It was thus assumed that it was a particle of zero rest mass. Enrico Fermi proposes "neutrino" as the name for Pauli's postulated particle. He formulates a quantitative theory of weak particle interactions in which the neutrino plays an integral part.

Because the nuclear states are also characterized by definite values of angular momentum, the neutrino along with the β particle must serve to conserve the angular momentum. The β-decay reaction is now described as

$$n \rightarrow p + e^- + \bar{\nu}, \qquad E_e \in \left[m_e, \frac{m_n^2 + m_e^2 - (m_p^2 + m_{\bar{\nu}}^2)}{2m_n} \right], \tag{1.2}$$

where the presence of the neutrino kinematically allows the electron to have a continuous energy spectrum [5].

In terms of the angular momenta involved, measurements showed that, either both the initial and product nuclei had integer angular momenta, or both had half-odd integer angular momenta, never otherwise.

This is only possible if the β particle and the neutrino together carry off integral units of angular momenta. Because the electrons has an intrinsic spin (1/2), the neutrino too must posses a half-odd integer spin, that is, it must obey Fermi-Dirac statistics, like the electron. For definiteness and simplicity, it was postulated to have a spin (1/2) like the electron.

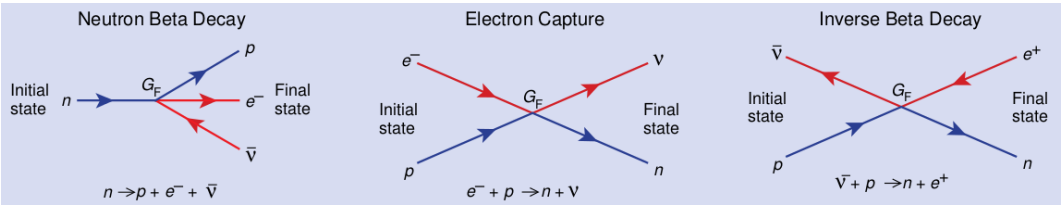

Figure 1.3: Left: Neutron Beta decay, this is the Pauli proposal. Center: Electron Capture. Right: Inverse Beta decay, reaction used by Reines and Cowan on reactor experiment. [5].

The neutrino eluded direct observation for a long time after Pauli's suggestion; persistent efforts, led to a direct observation of its properties by the use of some remarkable methods.

There is little relationship between neutrons proposed by Pauli and particles called neutrons in these days. They are completely different. Unfortunately or fortunately the expected particle was highly elusive, no mass, no charge, or no

strong interaction with matter.

This was the result of an small cross-section ($\sigma_\mu \sim 10^{-44} cm^2$), for about 25 years there were efforts to detect them. The possibility that a neutrino interacts with matter is very small. A lead block would need a length of a light year, to stop half of the neutrinos that passes through.

In the mid 1950's, Reines and Cowan had succeeded in detecting free antineutrinos for first time. The source of antineutrinos was a nuclear fision reactor. These were incident on a large target containing a liquid scintillator rich in hydrogen and induced the reaction $\bar{\nu}_e + p \rightarrow e^+ + n$ [12].

The ocurrence of this reaction was confirmed by the detection of the gamma pulse from the annihilation of the positron, followed by a delayed gamma pulse from the capture of the neutron on the proton in the target; the delay time being the slowing down time of the neutron prior to its capture.

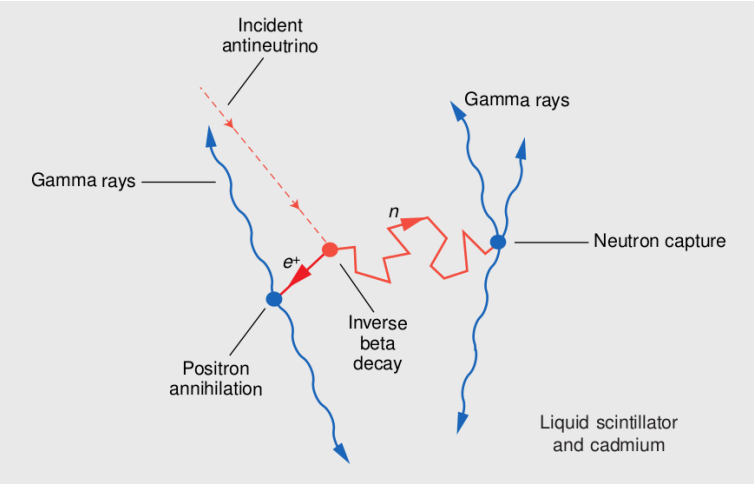

Figure 1.4: The indirect detection of antineutrinos by Reines and Cowan in 1956 [5].

In 1957, Nishijima pointed out the need for a new property characterizing masslesss neutrinos. The decay of the muon into an electron with no associated neutrinos (for example, $\mu \rightarrow e + \gamma$) has been searched for and not found. This transformation would be forbidden if the muon and the electron carried different lepton number, and these numbers were requiered to be separately conserved.

Since muon-decay to electron plus two neutrinos is observed, the two neutrinos cannot be identical; one neutrino must carry off electron lepton number

and the other must carry off muon lepton number, such that each type of lepton number can be conserved in the decay. The electron and its neutrinos from a family and the muon and its neutrino form a second family. These families are said to carry electron flavor and muon flavor, respectively.

The existence of a muon neutrino distinct from the electron neutrino was experimentally established by Lederman, Schwartz and Steinberger in 1963, using neutrinos from pions and kaons decays. These neutrinos produced only muons through interaction with nuclei of a target, and no electrons were produced.

1.3 Electroweak Interactions

One of the consequences of the electroweak unification, was the prediction of the neutral counterpart Z^0 of the charged weak gauge bosons $W^{\pm}$ with comparable couplings to fermions. This would mean that there must exist neutral current reaction, $\mu_\nu + nucleus \rightarrow \mu^- + X$, in which a muon and hadrons are produced in the final state, there must also occur the neutral current process $\nu_\mu + nucleus \rightarrow \nu_\mu + X$.

The neutrino will not be seen, and the signature for a neutral current process will be the appearance of hadrons alone in the final state. Exactly such events were seen in the Gargamell bubble chamber exposed to the neutrino beam at CERN. Events corresponding to the elastic scattering $\bar{\nu}_\mu e^- \rightarrow \bar{\nu}_\mu e^-$ were also observed.

These experiments showed that neutral current effects were indeed being observed. To get a quantitative measure of the effects, more sensitive experiments were planned.

Experimenters at SLAC measured the parity-violating asymmetry in the scattering of polarized electrons of a deuteron target. This involves measuring the difference between the Deep Inelastic Scattering (DIS) cross section for right and left handed electrons on deuterons $e_{R,L}d \rightarrow eX$.

A good measurement of this asymmetry yielded an accurate value fo the weak mixing angle.

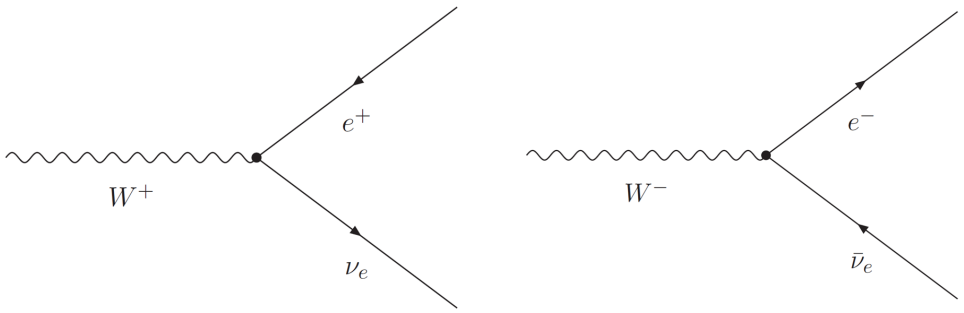

Figure 1.5: The $W^{\pm}$ boson diagrams. Left: W^+ described by Equation 1.3. Right: W_- decribed by Equation 1.4.

1.3.1 Isospin and Hypercharge

From the Figure 1.5 we recall the form of the charged currents:

$$\begin{aligned} J_\mu = J_\mu^+ &= \bar{u}_\nu \gamma_\mu (1/2)(1-\gamma^5) u_e \\ &= \bar{\nu} \gamma_\mu (1/2)(1-\gamma^5) e = \bar{\nu}_L \gamma_\mu e_L, \end{aligned} \tag{1.3}$$

$$\begin{aligned} J_\mu^+ = J_\mu^- &= \bar{u}_e \gamma_\mu (1/2)(1-\gamma^5) u_\nu \\ &= \bar{e}_L \gamma_\mu \nu_L, \end{aligned} \tag{1.4}$$

where the + and − superscripts are to indicate the charge-rasing and the charge-lowering character of the currents, respectively. The subscript L is used to denotate left-handed spinors and records the $V-A$ nature of the charged currents. Here, we have used the particle names to denote the Dirac spinors ($\bar{u}_\nu = \bar{\nu}$, $u_e = e$, etc).

We can rewrite these two charged currents in a suggestive 2D form, introducing the doublet:

$$\chi_L = \begin{pmatrix} 0 \\ e_- \end{pmatrix}_L \tag{1.5}$$

and the "step-up" and "step-down" operator $\tau_\pm = \frac{1}{2}(\tau_1 \pm i\tau_2)$:

$$\tau_+ = \begin{pmatrix} 0 & 1 \\ 0 & 0 \end{pmatrix} \quad \text{and} \quad \tau_- = \begin{pmatrix} 0 & 0 \\ 1 & 0 \end{pmatrix} \tag{1.6}$$

here, the τ's are the usual Pauli spin matrices. Then, now charged currents (equations 1.3 and 1.4) can be rewrite as

$$J_\mu^+(\chi) = \bar{\chi}_L \gamma_\mu \tau_+ \chi_L \quad \text{and} \quad J_\mu^-(\chi) = \bar{\chi}_L \gamma_\mu \tau_- \chi_L \tag{1.7}$$

Anticipating a possible $SU(2)$ structure for the weak currents, now we can introduce neutral current of the form

$$\begin{aligned} J_\mu^3(\chi) &= \frac{1}{2}\bar{\chi}_L\gamma_\mu\tau_3\chi_L \\ &= \frac{1}{2}\bar{\nu}_L\gamma_\mu\nu_L - \frac{1}{2}\bar{e}_L\gamma_\mu e_L. \end{aligned} \tag{1.8}$$

The Equation 1.8 can be reduced as

$$J_\mu^i(\chi) = \frac{1}{2}\bar{\chi}_L\gamma_\mu\tau_i\chi_L \quad \text{with} \quad i = 1, 2, 3 \tag{1.9}$$

whose corresponding charges

$$T^i = \int J_0^i(\chi)d^3\chi, \tag{1.10}$$

generate an $SU(2)_L$ algebra:

$$\left[T^i, T^j\right] = i\epsilon^{ijk}T^k. \tag{1.11}$$

The subscript L on $SU(2)$ is to indicate us that the weak isospin current couples only left-handed fermions.

Now, it is possible introduce j_μ^{em} in an attempt to save the $SU(2)$ symmetry. Note that neither of the neutral currents J_μ^{NC} or j_μ^{em} respects the $SU(2)_L$ symmetry. The idea is to form two orthogonal combinations which do have definite transformation properties under $SU(2)_L$; one combination, J_μ^3, is to complete the weak isospin triplet J_μ^i, while the second, j_μ^Y, is unchanged by $SU(2)_L$ transformations.

j_μ^Y is called the weak hypercharge current and is gived by

$$j_\mu^Y = \bar{\psi}\gamma_\mu Y\psi, \tag{1.12}$$

where the weak hypercharge Y is defined by

$$Q = T^3 + \frac{Y}{2}. \tag{1.13}$$

That is.

$$j_\mu^{em} = J_\mu^3 + \frac{1}{2}j_\mu^Y. \tag{1.14}$$

Just Q generates the group $U(1)_{em}$, so the hypercharge operator Y generates a symmetry group $U(1)_Y$. Thus, it has been incorporated the electromagnetic intersection, and as a result the symmetry group has been enlarged to

Lepton	T	T^3	Q	Γ
ν_e	1/2	1/2	0	-1
e_L^-	1/2	-1/2	-1	-1
e_R^-	0	0	-1	-2

Quark	T	T^3	Q	Γ
u_L	1/2	1/2	2/3	1/3
d_L	1/2	-1/2	-1/3	1/3
u_R	0	0	2/3	4/3
d_R	0	0	-1/3	-2/3

Tabla 1.1: Weak Isospin and Hypercharge quantum numbers for leptons and quarks [7].

$SU(2)_L \times U(1)_Y$.

In a sense, now it has been unified the electromagnetic with the weak interaction. However, rather than a single unified symmetry group, there are two groups, each with an independent coupling strength. So, in addition to e, we will need another coupling to fully specify the electroweak interaction.

The proposed weak isospin and weak hypercharge scheme is mathematically an exact copy of the original Gell-Mann-Nishijima scheme for arranging strange particles in $SU(2)$ hadronic isospin multiplets. The names "weak isospin" and "weak hypercharge" are taken from this analogy.

The $SU(2)_L \times U(1)_\Gamma$ proposal was first made by Glashow in 1961, long time before the discovery of the weak neutral current, and was extended to accommodate massive vector bosons ($W^\pm$, Z^0) by Weinberg in 1967 and Salam in 1968. It is frequently referred as the "Standar Model for Electroweak Interactions".

Since we have a product of symmetry groups, the generator Y must commute with the generators T^i. As a consequence, all the members of an isospin multiplet must have the same value of the hypercharge.

It is possible to incorporate quarks into the scheme. The weak isospin current J_μ^i couples only on doublets of left-handed quarks $(u, d)_L$; were $T = 1/2$ was assigned to q_L and $T = 0$ to q_R.

The quantum number are showed on the Table 1.1.

1.3.2 The Basic Electroweak Interaction

To complete the unification of the electromagnetic and weak interactions, now it is needed to modifiy the current-current form of the weak interaction

$$M = \frac{4G}{\sqrt{2}} J^{\mu} J^{+}_{\mu}, \tag{1.15}$$

and the invariant amplitude for an arbitrary neutral current process

$$M_{NC} = \frac{4G}{\sqrt{2}} 2\rho J^{NC}_{\mu} J^{NC\mu}. \tag{1.16}$$

Now, assuming that the current-current structure is an effective interaction which results from the exchange of massive vector bosons with only a small momentum transfer. The QED form for the basic interaction is

$$-ie(j^{em})^{\mu} A_{\mu}. \tag{1.17}$$

Just as the electromagnetic current is coupled to the photon, we assume that the electroweak current is coupled to vector boson.

The standard model consists of an isotriplet of vector fields W^i_{μ}, coupled with strength g to the weak isospin current J^i_{μ}, together with a single vector field B_{μ} coupled to the weak hypercharge current j^Y_{μ} with strength conventional taken to be $g'/2$.

The basic electroweak interaction is therefore

$$-ig(J^i)^{\mu} W^i_{\mu} - i\frac{g'}{2}(j^{\Gamma})^{\mu} B_{\mu}. \tag{1.18}$$

The fields

$$W^{\pm}_{\mu} = \sqrt{\frac{1}{2}}(W^1_{\mu} \mp iW^2_{\mu}), \tag{1.19}$$

describe massive charged bosons $W^{\pm}$, whereas W^3_{μ} and B_{μ} are neutral fields.

The electromagnetic interaction on Equation 1.17 is embedded in Equation 1.18. Indeed, it is generated the masses of the boson by symmetry breaking, the two neutral fields W^3_{μ} and B_{μ} must mix in such a way that the physical states are

$$A_{\mu} = B_{\mu} \cos\theta_W + W^3_{\mu} \sin\theta_W, \tag{1.20}$$

$$Z_{\mu} = -B_{\mu} \sin\theta_W + W^3_{\mu} \cos\theta_W, \tag{1.21}$$

where θ_W is called the Weinberg or Mixing Angle (although Glashow was the first to introduce the idea). The equations 1.20 and 1.21 for massless and massive interactions, respectively. Then now, it may be possible to write the electroweak neutral current interaction

$$\begin{aligned} -igJ^3_\mu(W^3)^\mu - i\frac{g'}{2}j^Y_\nu B^\mu = & \\ & - i\left(g\sin\theta_W J^3_\mu + g'\cos\theta_W\frac{j^Y_\mu}{2}\right)A^\mu \\ & - i\left(g\cos\theta_W J^3_\mu - g'\sin\theta_W\frac{j^Y_\mu}{2}\right)Z^\mu. \end{aligned} \tag{1.22}$$

The first term is the electromagnetic interaction, and so, the expression in the bracket on the Equation 1.17 must be

$$ej^{em}_\mu = e(J^3_\mu + \frac{1}{2}j^Y_\mu). \tag{1.23}$$

Therefore,

$$g\sin\theta_W = g'\cos\theta_W = e. \tag{1.24}$$

That is the mixing angle in the equations 1.20 and 1.21 is given by the ratio of the two independent group coupling constant, $\tan\theta_W = g'/g$.

With the equations 1.23 and 1.24, it is possible to express the weak neutral current interaction of 1.22 in the form

$$-i\frac{g}{\cos\theta_W}\left(J^3_\mu\sin^2\theta_w j^{em}_\mu\right)Z^\mu \equiv -i\frac{g}{\cos\theta_W}J^{NC}_\mu Z^\mu. \tag{1.25}$$

It is this definition:

$$J^{NC}_\mu \equiv J^3_\mu - \sin^2\theta_W j^{em}_\mu, \tag{1.26}$$

which relates the neutral current J^{NC} to the weak isospin current $\mathbf{J}$.

The electromagnetic interaction a $U(1)$ gauge symmetry with coupling e; "sits across" weak isospin as follows: an $SU(2)_L$ symmetry with coupling g; and weak hypercharge as follows: a $U(1)$ symmetry with coupling g'. The two couplings, g and g' can be replaced by e and θ_W, where the parameter θ_W is to be determined experimentally.

As summary, the observed neutral currents can be expressed as

$$j^{em}_\mu = J^3_\mu + \frac{1}{2}j^Y_\mu \quad \text{and} \quad J^{NC}_\mu - J^3_\mu - j^{em}_\mu\sin^2\theta_W, \tag{1.27}$$

in terms of currents J^3_μ and j^Y_μ belonging to symmetry groups $SU(2)_L$ and $U(1)_\Gamma$, respectively. The right-handed component of J^{NC}_μ, that was the original problem, has been arranged to cancel with that in $j^{em}_\mu \sin^2\theta_W$ to leave a pure left-handed J^3_μ of $SU(2)_L$, where $\sin^2\theta_W$ is to be determined by experiment.

Of course, the same $\sin^2\theta_W$ must be found in all electroweak phenomena.

1.3.3 The Effective Current-Current Interaction

The charged current phenomena could be explained by invariant amplitudes of the form

$$M_{CC} = \frac{4G}{\sqrt{2}} J^\mu J^\dagger_\mu, \tag{1.28}$$

and using the Equation 1.9, it is possible to get

$$J_\mu \equiv J^+_\mu(\chi) = \bar{\chi}_L \gamma_\mu \tau_+ \chi_L = \frac{1}{2}(J^1_\mu + iJ^2_\mu). \tag{1.29}$$

For an interaction preceeding via the exchange of a massive charged boson, rewriting the basic charged current interaction, (Equation 1.18) as

$$-i\frac{g}{\sqrt{2}}(J^\mu W^+_\mu + J^{\mu\dagger} W^-_\mu), \tag{1.30}$$

to get the Equation 1.30, an identity given by the Equation 1.31 was used

$$\frac{1}{2}(\tau_1 W^1 + \tau_2 W^2) = \sqrt{\frac{1}{2}}(\tau_+ W^+ + \tau_- W^-), \tag{1.31}$$

with $W^\pm$ on the Equation 1.19, it is possible to get

$$M^{CC} = \left(\frac{g}{\sqrt{2}} J_\mu\right)\left(\frac{1}{M^2_W}\right)\left(\frac{g}{\sqrt{2}} J^{\mu\dagger}\right), \tag{1.32}$$

where $1/M^2_W$ is the approximation to the W propagator at low q^2. Making the comparison of the equations 1.28 and 1.32

$$\frac{G}{\sqrt{2}} = \frac{g^2}{8M^2_W}. \tag{1.33}$$

In an analogous way, to express the amplitude for Neutral Current process in terms of Z exchange, it is necesary to use the Equation 1.25 for $|q^2| \ll M^2_Z$, then

$$M^{NC} = \left(\frac{g}{\cos\theta_W} J^{NC}_\mu\right)\left(\frac{1}{M^2_Z}\right)\left(\frac{g}{\cos\theta_W} J^{NC\mu}\right). \tag{1.34}$$

Now, comparing the Equation 1.34 with the current-current form for invariant amplitude

$$M^{NC} = \frac{4G}{\sqrt{2}} 2\rho J_{\mu}^{NC} J^{NC\mu}, \tag{1.35}$$

it is easy to identify

$$\rho \frac{G}{\sqrt{2}} = \frac{g^2}{8 M_Z^2 \cos^2 \theta_W}, \tag{1.36}$$

From equations 1.33 and 1.36, the ρ parameter can be found, wich specifies the relative strength of the neutral and charge current weak interactions,

$$\rho = \frac{M_W^2}{M_Z^2 \cos^2 \theta_W}. \tag{1.37}$$

Experimentally, $\rho = 1$ within a small error. This value is also predicted by the minimal model proposed by Weinberg and Salam.

1.3.4 Feynman Rules for Electroweak Interactions

To obtain the Feynman Rules for electroweak interactions (for $-iM$), previously was found how the electromagnetic interactions look like

$$-ie(j^{em})^{\mu} A_{\mu} = -ie(\bar{\psi} \gamma^{\mu} Q \psi) A_{\mu}, \tag{1.38}$$

led to the vertex factor

$$-ieQ_f \gamma^{\mu} \quad \text{for} \quad \gamma \to f\bar{f}, \tag{1.39}$$

where the Q_f is the charge of fermion f; $Q_f = -1$ for the electron. The outgoing $\bar{f}$ should be drawn as an ingoing f, and spinors attached to the fermion lines.

Following the same procedure for the charged current interaction in the previous section,

$$-i\frac{g}{\sqrt{2}} (\bar{\chi}_L \gamma^{\mu} \tau_+ \chi_L) W_{\mu}^{+} = -i\frac{g}{\sqrt{2}} (\bar{\nu}_L \gamma^{\mu} e_L) W_{\mu}^{+} \quad \text{for} \quad W^+ \to e^+ + \nu \tag{1.40}$$

$$-i\frac{g}{\sqrt{2}} (\bar{\chi}_L \gamma^{\mu} \tau_- \chi_L) W_{\mu}^{-} = -i\frac{g}{\sqrt{2}} (\bar{e}_L \gamma^{\mu} \nu_L) W_{\mu}^{-} \quad \text{for} \quad W^- \to e^- + \bar{\nu} \tag{1.41}$$

For $\chi_L = (\nu_e, e^-)$, these interactions lead to the vertex factor shown; spinors are associate with the external fermion lines just as in QED.

Clearly, the vertex factor will be the same for the $W^{\pm}$ coupling to the other fermion doublets (ν_μ, μ^-), (u, d), and so on.

$$-i\frac{g}{\cos\theta_W}\left(J^3_\mu - \sin^2\theta_W j^{em}_\mu\right) Z^\mu = -i\frac{g}{\cos\theta_W}\bar{\psi}_f\gamma^\mu \left[\frac{1}{2}(1-\gamma^5)T^3 - \sin^2\theta_W Q\right]\psi_f Z_\mu. \tag{1.42}$$

For the coupling $Z \to f\bar{f}$. It is customary to express the vertex factor in the general form

$$-i\frac{g}{2\cos\theta_W}\gamma^\mu(c^f_V - c^f_A\gamma^5). \tag{1.43}$$

By the comparison of the equations 1.42 and 1.43, the vector and axial vector couplings c_V and c_A, are determined in the standard model as

$$c^f_V = T^3_f - 2\sin^2\theta_W Q_f \quad \text{and} \quad c^f_A = T^3_f, \tag{1.44}$$

where T^3_f and Q_f are, respectively, the third component of the weak isospin and the charge of fermion f. The Feynman rules allow us to predict the decay properties of the $W^{\pm}$ and Z^0 bosons in the standard model.

1.3.5 Tree level Cross Sections

The Neutrino Electron Scattering process has an small cross-section and correspondingly it is very difficult to measure. Nevertheless, because the heroic experimental efforts, they have played a crucial role in confirming the $SU(2)_L \times U(1)_Y$ structure of the standard model and in helping to unravel subtle properties of neutrinos.

On the electroweak interaction framework, several process of neutrino and antineutrino scattering cross section can be calculated, in this framework it is possible to divide them into tree categories. One for the pure W exchange and the another for the mixing of W and Z^0 exchange. The Neutrino electron scattering is represented by the Figure 1.6.

A variety of neutrino and antineutrino electron scattering cross sections are possible. This process can be divided into three categories. The fist set, although kinematically suppressed, is conceptually simple. It corresponds to pure W boson exchange, it means Charge Current, on this channel (t),

$$\nu_l + e \to l + \nu_e, \tag{1.45}$$

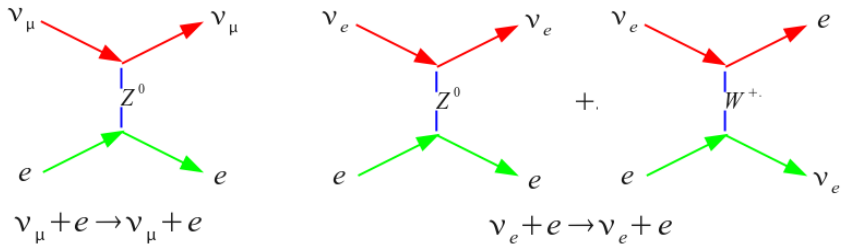

Figure 1.6: Feynman diagrams for Neutrino Electron Scattering. Left Neutral Current. Left Charge Current.

where, $l = \nu$ or τ. And for the other channel (s)

$$\bar{\nu}_e + e \to l + \bar{\nu}_l. \tag{1.46}$$

The reaction described by the Equation 1.46 sometimes are referred to as inverse muon or tau decays. Then the threshold energy for electrons at rest is gived by

$$E_\nu >> \frac{m_l^2 - m_e^2}{2m_e}, \tag{1.47}$$

that is $E_\nu \geq 10.8$ GeV for $l = \mu$ and $E_\nu \geq 3$ TeV for $l = \tau$. Now, for generality we are only using l. Also, from the Equation 1.46 for semileptonic reactions, like

$$\begin{aligned} & d + \bar{u}, \\ \bar{\nu}_e + e \to\ & s + \bar{u}, \\ & d + \bar{c}, \end{aligned} \tag{1.48}$$

are also possible, however these possibilities will not be discussed on this thesis, i.e., only leptonic reactions.

For the Neutral Current Channel, i.e. pure Z exchange, gives rise to a second more easily acccesible set of reactions like these

$$\nu_l + e \to \nu_l + e \quad \text{and} \quad \bar{\nu}_l + e \to \bar{\nu}_l + e, \tag{1.49}$$

where $l = \nu$ or τ. And the last(third) possibility are

$$\nu_e + e \to \nu_e + e \quad \text{and} \quad \bar{\nu}_e + e \to \bar{\nu}_e + e, \tag{1.50}$$

this process is described by the right diagram on the Figure 1.6, it proceeds through a combination W and Z exchange amplitudes.

As a simplification, it is possible to make the following assumptions: neutrino masses and mixing are neglected; $|q^2 << m_W^2|$ or m_Z^2, i.e. the propagator effects and effective four fermions amplitudes employed can be ignored, due that the electron target is at rest.

Using the Fermi constant to normalize all the neutrino scattering amplitudes, that is obtained from the muon decay lifetime

$$G_\mu = \frac{g^2}{4\sqrt{2}m_W^2} = 1.1663 \times 10^{-5}\text{GeV}^{-2}, \tag{1.51}$$

$$M_{CC} = -i\frac{G_\mu}{\sqrt{2}}\bar{u}_l\gamma^\alpha(1-\gamma_5)u_{\nu_l}\bar{u}_{\nu_e}\gamma_\alpha(1-\gamma_5)u_e. \tag{1.52}$$

The Fermi constant are determined with good accurate. Then using these assumptions, for the Charged Current reactions, the effective amplitude is described by the next equation:

$$\frac{d\sigma^{\nu_l e\to l\nu_e}}{dy} = \frac{G_\mu^2}{\pi}[2m_eE_\nu - (m_l^2 - m_e^2)], \tag{1.53}$$

where the u_f are four component spinors corresponding to their subscript fermions. Summing over all polarization and spin states, and integrating over all unobserved momenta, the obtained differential cross section in the electron rest frame, with respect to the fractional energy imparted to the outgoing lepton for $l = \nu$ or τ is

$$\frac{d\sigma^{\bar{\nu}_e e\to l\bar{\nu}_l}}{dy} = \frac{G_\mu^2}{\pi}[2m_eE_\nu(1-y)^2) - (m_l^2 - m_e^2)(1-y)], \tag{1.54}$$

where E_ν is the energy of the incident neutrino and m_e and m_l are the masses of the electron and the outgoing lepton, respectively.

The dimensionless inelastic parameter y reflects the kinematic energy of the outgoing lepton, which in this particular example is

$$y = \frac{E_l - \frac{m_l^2 - m_e^2}{2m_e}}{E_\nu}. \tag{1.55}$$

The limits of y are such that

$$0 \le y \le y_{Max} = 1 - \frac{m_l^2}{2m_eE_\nu + m_e^2}. \tag{1.56}$$

On this derivation, we are not considering the contribution from the neutrino masses, which in this context is too small to be observed kinematically.

The cross section descibed on the equations 1.53 and 1.54 has a threshold energy imposed by the kinematics of the system, $E_\nu \geq (m_l^2 - m_e^2)/2m_e$.

Considering the very high energy limit, i.e. extreme relativistic

$$E_\nu >> \frac{m_l^2 - m_e^2}{2m_e}, \tag{1.57}$$

and integrating the Equation 1.53 over y, yield a simple expression for the total neutrino cross section as a function of neutrino energy

$$\begin{aligned} \sigma^{\nu_l e \to l \nu_e} \simeq 3\sigma^{\bar{\nu}_e e \to l \bar{\nu}_l} &\simeq \frac{2G_\mu^2 m_e E_\nu}{\pi} \\ &\simeq 1.5 \times 10^{-41} (E_\nu / GeV) cm^2, \end{aligned} \tag{1.58}$$

from the Equation 1.58, the neutrino cross section grows linearly with the energy.

From Equation 1.49, their kinematics is simple since $m_l \to m_e$, but it is not possible to ignore the left and right-handed leptonic couplings in the effective amplitude.

As a result, it is obtained a more complex expresions for the relevant matrix element, taking into account that $l = \nu$ or τ.

$$M_{NC} = i\frac{G_\mu}{\sqrt{2}} \bar{u}_l \gamma^\alpha [\epsilon_- \bar{u}_e \gamma_\alpha (1 - \gamma_5) u_{\nu_e} \epsilon_+ \bar{u}_e \gamma_\alpha (1 + \gamma_5) u_{\nu_e} u_e \gamma_\alpha (1 - \gamma_5) u_e]. \tag{1.59}$$

Considering

$$\epsilon_- = g_V + g_A = g_L \quad \text{and} \quad \epsilon_+ = g_V - g_A = g_R, \tag{1.60}$$

where g_v and g_A are the vector and axial-coupling constants, respectively. Then

$$M_{NC} = -\sqrt{2} G_\mu \left[[\bar{\nu}_l \gamma^\alpha (g_V^\nu - g_A^\nu \gamma_5) \nu_l] \times [\bar{e} \gamma_\alpha (g_V^f - g_A^f \gamma_5) e] \right]. \tag{1.61}$$

The same formulation (equations 1.59 and 1.61) can be expressed using the left and right-handed couplings, g_L and g_R

$$\begin{aligned} M_{NC} = -\sqrt{2} G_\mu [[g_L^\nu \bar{\nu}_l \gamma^\alpha (1 - \gamma_5) \nu_l + g_R^\nu \bar{\nu}_l \gamma^\alpha (1 + \gamma_5) \nu_l] \\ \times [g_L^f \bar{e} \gamma^\alpha (1 - \gamma_5) e + g_R^f \bar{e} \gamma^\alpha (1 + \gamma_5) e]]. \end{aligned} \tag{1.62}$$

From the Standard Model

$$g_L^\nu = \sqrt{\rho}(+\frac{1}{2}), \qquad g_R^\nu = 0$$
$$Sg_L^f = \sqrt{\rho}(I_3^f - Q^f \sin^2\theta_W), \qquad g_R^f = \sqrt{\rho}(-Q^f \sin^2\theta_W)$$

or, in terms of Vector or Axial Couplings

$$g_V^\nu = g_L^\nu + g_R^\nu = \sqrt{\rho}(+\frac{1}{2}),$$
$$g_A^\nu = g_L^\nu - g_R^\nu = \sqrt{\rho}(+\frac{1}{2}),$$
$$g_V^f = g_L^f + g_R^f = \sqrt{\rho}(I_3^f - 2Q^f \sin^2\theta_W),$$
$$g_A^f = g_L^f - g_R^f = \sqrt{\rho}(I_3^f).$$

Here, I_3^f and Q^f are the weak isospin and electromagnetic charge of the target lepton, ρ is the relative coupling strength between Charged and Neutral Current. Here at the tree level, $\rho \equiv 1$ and θ_W is the Weinberg mixing angle.

Also, from the Standard Model the definition of the relation between the electroweak couplings and the gauge boson masses M_W and M_Z are

$$sin^2\theta_W \equiv 1 - \frac{M_W^2}{M_Z^2}. \tag{1.63}$$

The cross section for the Neutral Current reactions are directly sensitive to the left and right handed couplings.

Writing the differential cross section in terms of their vector and axial-vector currents, using some definitions

$$g_V \equiv 2g_L^\nu g_V^f \quad \text{and} \quad g_A \equiv 2g_L^\nu g_A^f. \tag{1.64}$$

For neutrinos

$$\frac{d\sigma^{\nu_l e\to\nu_l e}}{dy} = \frac{G_\mu^2 m_e E_\nu}{2\pi}[(g_V + g_A)^2 + (g_V - g_A)^2 \times (1-y)^2 - (g_V^2 - g_A^2)\frac{m_e y}{E_\nu}]. \tag{1.65}$$

And for antineutrinos

$$\frac{d\sigma^{\bar{\nu}_l e\to\bar{\nu}_l e}}{dy} = \frac{G_\mu^2 m_e E_\nu}{2\pi}[(g_V - g_A)^2 + (g_V + g_A)^2 \times (1-y)^2 - (g_V^2 - g_A^2)\frac{m_e y}{E_\nu}], \tag{1.66}$$

where, the inelasticity parameter is

$$y = \frac{E'_e - m_e}{E_\nu} \quad \text{and} \quad 0 \leq y \leq y_{max} = \frac{1}{1 + m_e/2E_\nu}, \tag{1.67}$$

with E'_e being the final state electro energy, and the small interference $g_L g_R = (g_V^2 - g_A^2)$, term has been retained for low energies applications. We can see that the cross sections $\sigma^{\nu_l e \to \nu_l e}$ and $\sigma^{\bar{\nu}_l e \to \bar{\nu}_l e}$ are related by $g_L \leftrightarrow g_R$ interchange.

Now considering that

$$g_L = \frac{1}{2} - \sin^2\theta_W \quad \text{and} \quad g_R = -\sin^2\theta_W, \tag{1.68}$$

and neglecting terms of relative order m_e/E_ν, then the integrated cross section is gived by the Equation 1.69 for neutrinos

$$\sigma^{\nu_l e \to \nu_l e} = \frac{G_\mu^2 m_e E_\nu}{2\pi}\left[1 - 4\sin^2\theta_W + \frac{16}{3}\sin^4\theta_W\right], \tag{1.69}$$

and the equivalent for antineutrinos

$$\sigma^{\bar{\nu}_l e \to \bar{\nu}_l e} = \frac{G_\mu^2 m_e E_\nu}{2\pi}\left[\frac{1}{3} - \frac{4}{3}\sin^2\theta_W + \frac{16}{3}\sin^4\theta_W\right]. \tag{1.70}$$

With $\sin^3\theta_W \simeq 0.23$, these cross sections are very small, i.e.,

$$\sim 10^{-42}(E_\nu/\text{GeV})\text{cm}^2.$$

However, they have been rather well measured for muon-neutrinos, yielding $\sin^2\theta_W$ to about $\pm 3.5\%$. At that level, the electroweak radiative corrections become important and must be applied in any serious study.

Now, the last neutrino electron elastic scattering to be considered is for electron-neutrinos(Equation 1.50), it comes from a combined W and Z boson exchange. Replazing for $\nu_l \to \nu_e$ and $\bar{\nu}_l \to \bar{\nu}_e$ on the equations 1.65 and 1.66, respectively. Considering

$$g_L \to g'_L = g_L - 1 = -\frac{1}{2} - \sin^2\theta_W, \tag{1.71}$$

$$g_R \to g'_R = g_R = -\sin^2\theta_W, \tag{1.72}$$

and again, ignoring the m_e/E_ν effects, the cross section for electron-neutrino electron elastic scattering

$$\sigma^{\nu_e e \to \nu_e e} = \frac{G_\mu^2 m_e E_\nu}{2\pi}\left[1 + 4\sin^2\theta_W + \frac{16}{3}\sin^4\theta_W\right]. \tag{1.73}$$

Reaction	$\sigma/(G_\mu^2 m_e E_\nu/2\pi)$	Relative size
$\nu_\mu e \to \mu^- \nu_e$	4	4
$\bar{\nu}_e e \to \mu^- \bar{\nu}_\mu$	$\frac{4}{3}$	$\frac{4}{3}$
$\nu_\mu e \to \nu_\mu e$	$1 - 4\sin^2\theta_W + \frac{16}{3}\sin^4\theta_W$	0.362
$\bar{\nu}_\mu e \to \bar{\nu}_\mu e$	$\frac{1}{3} - \frac{4}{3}\sin^2\theta_W + \frac{16}{3}\sin^4\theta_W$	0.309
$\nu_e e \to \nu_e e$	$1 + 4\sin^2\theta_W + \frac{16}{3}\sin^4\theta_W$	2.2
$\bar{e}_\mu e \to \bar{\nu}_e e$	$\frac{1}{3} + \frac{4}{3}\sin^2\theta_W + \frac{16}{3}\sin^4\theta_W$	0.922

Tabla 1.2: Tree level neutrino electron scattering cross sections in units of $G_\mu^2 m_e E_\nu/2\pi$ [16].

For electro-antineutrino electron elastic scattering,

$$\sigma^{\bar{\nu}_e e \to \bar{\nu}_e e} = \frac{G_\mu^2 m_e E_\nu}{2\pi}\left[\frac{1}{3} + \frac{4}{3}\sin^2\theta_W + \frac{16}{3}\sin^4\theta_W\right]. \tag{1.74}$$

These cross sections are roughly a factor 7 and 3 respectively larger than those in equations 1.69 and 1.70.

The Table 1.2 shows a summarize of the tree level predictions and relative sizes for the neutrino electron scattering cross sections.

The main limitation on the precise measurements of the cross section are the systematic uncertainties in the neutrino flux and spectrum. One way to help overcome that limitation is often the discussion of some cross sections ratios.

For low energies

$$R_1 \equiv \frac{\sigma^{\nu_\mu e \to \nu_\mu e}}{\sigma^{\bar{\nu}_\mu e \to \bar{\nu}_\mu e}}, \tag{1.75}$$

and using the low energy neutrinos stopped from π^+ and μ^+ decays in the chain to normalize the flux

$$\pi^+ \to \mu^+ \nu_\mu \quad \text{and} \quad \mu^+ \to e^+ \nu_e \bar{\nu}_\mu, \tag{1.76}$$

is possible to get other ratio

$$R_2 = \frac{\sigma^{\nu_\mu e \to \nu_\mu e}}{\sigma^{\bar{\nu}_\mu e \to \bar{\nu}_\mu e} + \sigma^{\nu_e e \to \nu_e e}}. \tag{1.77}$$

The R_2 ratio was proposed for LAMPF Experiment, but would be useful for neutrino physics at an intense neutron source facility where many π^+ are produced.

If the flux normalization could be controlled, using the equations 1.69, 1.70, 1.73 and 1.74, then the expectation at third level for R_1 and R_2 is

$$R_1 = \frac{3 - 12\sin^2\theta_W + 16\sin^4\theta_W}{1 - 4\sin^2\theta_W + 16\sin^4\theta_W}, \tag{1.78}$$

$$R_2 = \frac{3 - 12\sin^2\theta_W + 16\sin^4\theta_W}{4 + 8\sin^2\theta_W + 32\sin^4\theta_W}. \tag{1.79}$$

The best solution for the flux normalization are the Neutrino Factories. It can be done using the decay possibilities $\mu^- \to e^-\bar{\nu}_e\nu_\mu$ and $\mu^+ \to e^+\nu_e\bar{\nu}_\mu$, from a long straight section, at a muon storage ring, would have very well-specified neutrino energy spectra.

Then, one possibility would be to run in both modes, and after weighting for the different spectra, measure

$$R_3 = \frac{\sigma^{\nu_\mu e\to\nu_\mu e} + \sigma^{\bar{\nu}_e e\to\bar{\nu}_e e}}{\sigma^{\bar{\nu}_\mu e\to\bar{\nu}_\mu e} + \sigma^{\nu_e e\to\nu_e e}}, \tag{1.80}$$

where using the previous results, the prediction of the Equation 1.80 at the third level is

$$R_3 = \frac{1 - 2\sin^2\theta_W + 8\sin^4\theta_W}{1 + 2\sin^2\theta_W + 8\sin^4\theta_W}. \tag{1.81}$$

1.3.6 Experimental Test of Electroweak Theory

In the understanding of the electroweak force and the Standard Model, the Neutrino Lepton interaction has played a very important role. For example, the first Neutral Current ($\bar{\nu}_\mu + e^- \to \bar{\nu}_\mu + e^-$) observation was made on Gargamelle Experiment [14], The Figure 1.7 shows a muon-neutrino electron elastic scattering.

This observation, in conjunction with the observation of the Neutral Current Deep Inelastic Scattering (NC-DIS), confirmed the existence of Weak Neutral Currents and helped to solidify the $SU_L(2) \times U(1)_Y$ structure of the standard model [13].

Subsequent experiments further utilized the information from the observed rates of neutral current reactions as a gauge for measuring $\sin^2\theta_W$ directly.

Neutrino Lepton scattering is a particular sensitive probe because to first order the cross section depends just on one parameter, $\sin^2\theta_W$ [15].

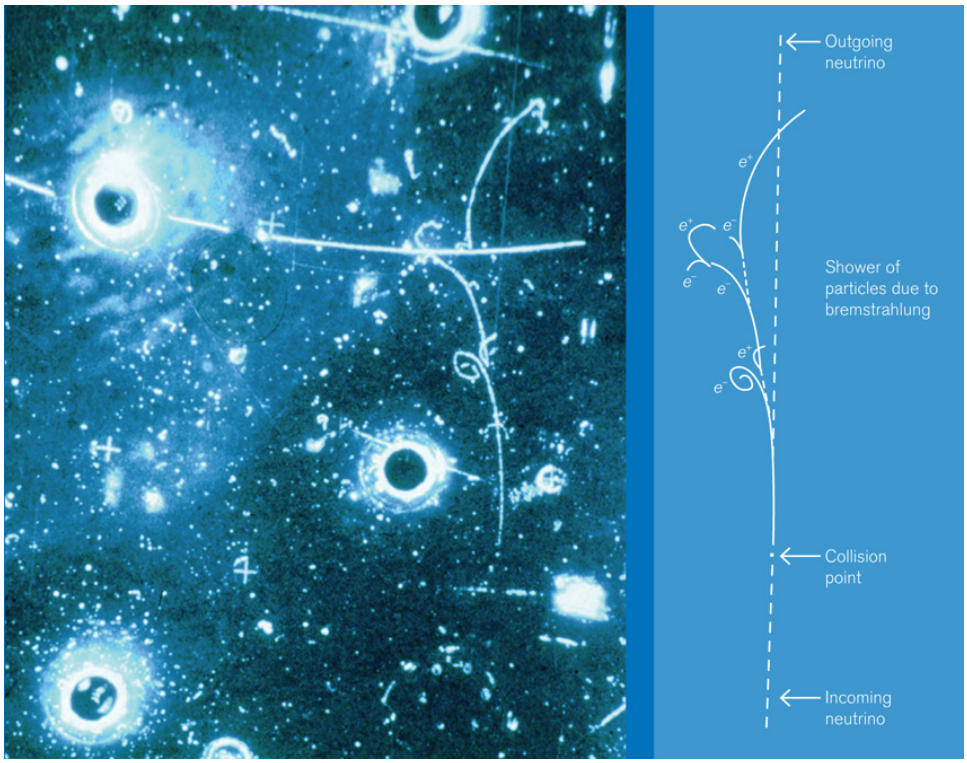

Figure 1.7: Firts observation of the leptonic Neutral Current candidate event at Gargamelle CERN Experiment [4].

Several experimental methods have been employed to measure neutrino lepton scattering. Among the first, included the observation of $\bar{\nu}_e + e^- \rightarrow e^- + \bar{\nu}_e$ scattering by Reines, Gurr and Sobel at the Savannah River Plant reactor complex. Making use of the intense $\bar{\nu}_e$ flux produced in the reactors, an $\pm 20\%$ measurement of the weak mixing angle was extracted.

A more recent results from the Taiwan EXperiment On Neu-trinO (TEXANO Experiment), also utilizes reactor antineutrinos as its source. There exists an inherent difficulty to extract these events, as they are often masked by large low-energy backgrounds, particularly those derived from Uranium and Thorium decays.

The majority of the recent precision test have been carried out using high-energy neutrino beams. Experiments such as Gargamelle, Brokhaven's Alternating Gradient Synchroton (AGS) source, Chicago-Columbia-Fermilab-Rochester (CCFR) and NuTeV fall within this category. Often these experiments exploit the rise in cross section with energy to increase the sample size collected for analysis.

The stopped beam pions have also been used for these electroweak tests at the Los Alamos National Laboratory and Liquid Scintillator Neutrino Detector (LSND) experiments [28].

1.4 Neutrino Oscillation

The first suggestion that free neutrinos traveling through space might oscilate, that is, periodically change from one neutrino type to another, was made by Pontecorvo on 1957.

Gell-Mann and Pais had just shown how quantum mechanical interference would allow the neutral kaon K^0 ($s\bar{d}$) and its antiparticle $\bar{K}^0$ ($\bar{s}d$) to oscillate back and forth, because the quark mass states are mixtures of weak states.

Pontecorvo noted very briefly that, if the neutrino had mass and if the total lepton number were not conserved, the neutrino could imitate the neutral kaon, oscillating between particle and antiparticle as it travels through empty space. This possibility would have implied that the neutrino is a massive Majorana particle with no definite distinction between particle and antiparticle forms.

Although very interesting and still relevant today, Pontecorvos suggestion was not explored in 1957 because Lee and Yangs theory of the massless two component neutrino was just gaining acceptance. This theory helped to explain why parity was maximally violated in nuclear beta decay.

The existence of a left-handed neutrino different from the right-handed antineutrino by having the opposite lepton number, was a crucial postulate and in that theory, particle-antiparticle oscillations could not be possible.

If neutrinos are massless, then the neutrinos, which enter the weak interaction Lagrangian are also the mass eigenstates. If anyone of them has a mass, then it may be that the mass eigenstates wich is denoted by ν_i with $i = 1, 2, 3$ are different from flavor eigenstates ν_ω ($\omega = e, \mu, \tau$). In this case, we can get neutrino oscillations.

The phenomena of neutrino oscillation can provide a mechanism to measure extremely small neutrino masses. Remembering, that two sets of states $|\nu_\omega\rangle$

and $|\nu_i\rangle$ are connected with each other by a unitary transformation:

$$|\nu_\omega\rangle = \sum_i U_{\omega i} |\nu_i\rangle . \tag{1.82}$$

Now,

$$H(k) |\nu_i\rangle = E_i |\nu_i\rangle , \tag{1.83}$$

where

$$E_i = (k^2 + m_i^2)^{1/2} \approx k + \frac{m_i^2}{2k}, \tag{1.84}$$

since, $k \gg m_i$ and on the extreme relativistic limit, now at time t $|\nu(t)\rangle$, satisfies the Schrödinger Equation

$$i\frac{d}{dt} |\nu(t)\rangle = H |\nu(t)\rangle . \tag{1.85}$$

In ν_i basis, H is a diagonal matrix with eigenvalues E_1, E_2 and E_3. Thus

$$|\nu_i(t)\rangle = e^{-iE_i t} |\nu_i(0)\rangle = e^{-iE_i t} |\nu_i\rangle . \tag{1.86}$$

Hence from Equation 1.82,

$$|\nu_\omega(t)\rangle = \sum_i U_{\omega i} e^{-iE_i t} |\nu_i\rangle , \tag{1.87}$$

and

$$\begin{aligned} \langle \nu_{\omega'} | \nu_\omega \rangle_t &= \sum_i U_{\omega i} e^{-iE_i t} \langle \nu_{\omega'} | \nu_i \rangle \\ &= \sum_i U_{\omega i} e^{-iE_i t} U^*_{\omega' i}. \end{aligned} \tag{1.88}$$

Thus the probability that at time t, the neutrino of type ω is converted to the neutrino of type ω' is given by

$$\begin{aligned} P_{\omega'\omega} &= |\langle \nu_{\omega'} | \nu_\omega \rangle|^2 \\ &= \sum_i \sum_j (U_{\omega i} U^*_{\omega' i})(U_{\omega j} U^*_{\omega' j}) \cos(E_i - E_j)t \end{aligned} \tag{1.89}$$

using the relation $L = ct$ and

$$\lambda_{ij} = \frac{2\pi c}{E_i - E_j}, \tag{1.90}$$

$$(E_i - E_j)t = \frac{L(m_i^2 - m_j^2)}{2E_\nu} = \frac{L\Delta_{ij}}{2E_\nu}. \tag{1.91}$$

Neglecting CP-violating phases so that U is real, it is convenient to rewrite it as

$$P_{\omega'\omega} = \delta_{\omega'\omega} - 4\sum_{j>i} U_{\omega i}U_{\omega' i}U_{\omega j}U_{\omega' j}\sin^2\left(\frac{\pi L}{\lambda_{ij}}\right), \tag{1.92}$$

where L is the distance travelled after ν_ω is converted into $\nu_{\omega'}$ and:

$$\lambda_{ij} = \frac{4\pi E_\nu}{\Delta_{ij}} = 2.47\text{m}\left(\frac{E_\nu}{\text{MeV}}\right)\frac{\text{eV}^2}{\Delta_{ij}}. \tag{1.93}$$

As a consequence of CPT and CP invariance

$$P_{\nu_{\omega'}\nu_\omega} = P_{\bar{\nu}_{\omega'}\bar{\nu}_\omega} = P_{\nu_\omega\nu_{\omega'}} = P_{\bar{\nu}_\omega\bar{\nu}_{\omega'}}. \tag{1.94}$$

The form of transition probability (Equation 1.92) depends on the spectrum of Δm^2 or Δ_{ij} chosen and the explicit form of U. If Δm^2 is chosen such that $\lambda \gg L$, then the oscillation term

$$\sin^2\left(\frac{\pi L}{\lambda}\right) \to 0 \quad \text{for} \quad \lambda \gg L, \tag{1.95}$$

On the other hand, for $\lambda \ll L$

$$\sin^2\left(\frac{\pi L}{\lambda}\right) \to 1/2 \quad \text{for} \quad \lambda \ll L. \tag{1.96}$$

Then, for conversion of ν_e to ν_x, where ($x = \mu$ or τ),

$$U = \begin{pmatrix} \cos\theta & \sin\theta \\ -\sin\theta & \cos\theta \end{pmatrix}, \tag{1.97}$$

and

$$P_{\nu_e\to\nu_x} = \sin^2 2\theta \sin^2\left[1.27\frac{\Delta m^2}{E_\nu}L\right], \tag{1.98}$$

while the survival probability is $P_{\nu_e\to\nu_e} = 1 - P_{\nu_e\to\nu_x}$. Here θ is the vacuum mixing angle. $P_{\nu_e\to\nu_e}$ and $P_{\nu_e\to\nu_x}$ oscillate with L as shown in the Figure 1.8.

The amplitude of the oscillation is determined by the mixing angle; the wavelength of the oscillation is λ.

To look for oscillation, is needed the following conditions:

- Low energy neutrinos.
- Long path length.
- Large flux.

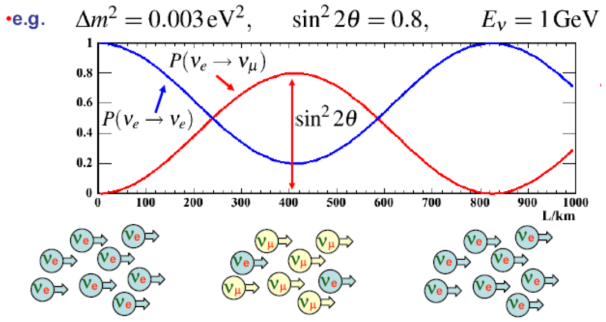

Figure 1.8: Pictorial explanation of neutrino oscillations. [33].

1.5 Motivation

1.5.1 Neutrino Electron Scattering

Neutrino Electron Elastic Scattering is a purely leptonic process, where a neutrino scatters off an electron by the exchange of a virtual vector boson. The Q^2 range covered at the present by the neutrino electron scattering experimentally reaches from 10^{-6} at nuclear reactors to 10^{-2} at accelerators but it is always small compared to the mass of Z^0.

From a theoretical point of view, the process of neutrino electron scattering is comparatively simple. In the previous sections we defined the relevant quantities to describe this process in the theoretical frame of the the Standard Model at tree level. But going to higher orders we will need make some remarks on radiative corrections as well as on physics beyond the Standard Model.

The kinematics of the neutrino electron elastic scattering is fully described by a single variable; for instance by θ_e the angle of the outgoing electron with respect to the neutrino beam.

Defining E_ν and E_e as the energies of the incoming neutrino and outgoing electron respectively, m_e as the electron mass, and $y = E_e/E\nu$ as the fractional energy loss of the neutrino in the laboratory system.

With the assumption of $m_e << E_e$, and the small angle approximation for $\cos\theta_e$,

$$E_e\theta_e^2 = 2m_e(1-y), \tag{1.99}$$

and, as $0 \leq y \leq 1$. The experimental important constraint is $E_e\theta_e^2 < 2m_e$. The full derivation of the Equation 1.99 and the kinematic constraint is in the Appendix C.

This means the outgoing electron is scattered in extremely forward direction, which is used experimentally to subtract, on a statistical basis, background events, which has a much broader distribution in $E_e\theta_e^2$.

On the other hand this signature makes impossible to measure directly the $y-$distribution of neutrino electron scattering, as reachable resolution are just in the same order of magnitude as the kinematical bound.

This remarkable feature has been exploited extensively in various neutrino experiments, particularly for solar neutrino detection. The Kamiokande Neutrino Experiment was the first to use this reaction to recontruct ^8B neutrino events from the Sun and point back to the source [19].

1.5.2 Neutrino Flux Constraint

The neutrinos can come from natural or man-made sources. From the natural sources, the energy and the intensity can not be controled. However the accelerator neutrino beams are controllable in both energy and intensity.

Note that, given our inability to identify the neutrino flavor after it has scattered off the target electron, there is no way of recognizing whether the scattered neutrino has the same lepton-flavor number or lepton number as the incoming one.

The basis of this thesis is the differential event spectrum $dN(T)/dT$. This is the number of neutrino electron elastic scattering events within the interval T to $T + dT$ of electron recoil kinetic energy. It involves the convolution of the differential cross section $d\sigma(T, E_\nu)/dT$ and the incoming neutrino energy spectrum, $d\Phi(E_\nu)/dE_\nu)$.

Since the final state electrons scattered from the various neutrino types are experimentally indistinguishable, their contributions must be incoherently added, leading to

$$\frac{dN(T)}{dT} = (time) \times (\#targets) \times \sum_i^{flavors} \int dE_\nu \frac{d\Phi_i(E_\nu)}{dE_\nu} \frac{d\sigma_i(T, E_\nu)}{dT}, \quad (1.100)$$

where $(\#targets)$ is the total number of target electrons in the detector and, (time) is the time duration of the experiment.

To use the Equation 1.100, we must know the flux and the cross section, along with their associated uncertainties.

Then, the number of events depends from the neutrino flux, the tiny cross section and the targer used

$$N_\nu(E_\nu) \approx \Phi_\nu(E_\nu) \times \sigma_\nu(E_\nu) \times targets. \tag{1.101}$$

The energy spectrum of the produced neutrino beam is quite broad in general. Since neutrinos are electrically neutral, once generated, they are difficult to control or monitor directly.

Experimental parameters that adjust the characteristics of the beam are things like the primary proton energy and the current and position of the magnetic horns.

The neutrino spectrum has to be predicted by simulation. Generally, the flux prediction has large uncertainties (15-20%) due to poor knowledge of the hadron production.

Long baseline oscillation experiments often also use near detectors to measure the flux near the neutrino source. This unoscillated flux measured is used to normalize the flux in the far detector. If the detector technologies are different in the near and far detectors, the nuclear dependence of the cross section introduces systematic error in the flux normalization.

Even if the detector technology is identical in the near and far detectors, the flux in the near detector is not identical with the far detector. The near detector sees the neutrino beam angle spread from the sizable decay pipe, while the far detector only sees a point-like source.

Also, the oscillated spectrum at the far detector is quite different than at the near detector.

The neutrino spectrum is different depending on beam angle due to the kinematics of pion decay. Since muons and kaons present in the secondary hadrons also can decay into electron neutrinos, ν_μ beams typically have about 1% of ν_e contamination. This creates an irreducible background for ν_e appearance experiments.

Chapter 2

The MINERνA Experiment

The MINERνA Experiment is a dedicate neutrino-nucleus cross section experiment, located at Fermilab, Batavia, IL, in USA (http://www.fnal.gov). The MINERνA Collaboration is composed by approximately 70 particle and nuclear physicists from 7 countries(http://minerva.fnal.gov/).

MINERνA Experiment employs two detectors: the main (MINERνA Detector) is used to measure the neutrino interaction cross section, and the second one (Test Beam Detector) is used to calibrate the response of the main detector to the electromagnetic and hadronic interactions.

The MINERνA Detector uses the NuMI beamline, and is located approximately 100 m underground at the same room with the MINOS Near Detector.

The MINERνA Detector employs fine-grained polystyrene scintillator for tracking and calorimetry. In addition to the active scintillator target, the detector contains passive nuclear targets of carbon, iron, lead, water, and liquid Helium. The MINOS Near Detector sits downstream of MINERνA Detector and it is used like a muon spectrometer.

The MINERVνA Experiment play an important and potentially decisive role in helping the current and future precision oscillation experiments to reach their ultimate sensitivity.

2.1 The NuMI Beamline

The Figure 2.1 shows a schematic view of the Neutrino Main Injector (NuMI) beamline. The production of the neutrino beam begins with the extraction of 120 GeV protons from the Fermilab Main Injector accelerator, in pulses of ~ 10

μs, and consisting of anywhere between 1×10^{11} and 4.5×10^{13} protons.

The pulses, commonly referred as spills, are typically extracted every 2.2 seconds. The protons are transferred to the NuMI target hall where they collide with a fixed Graphite target.

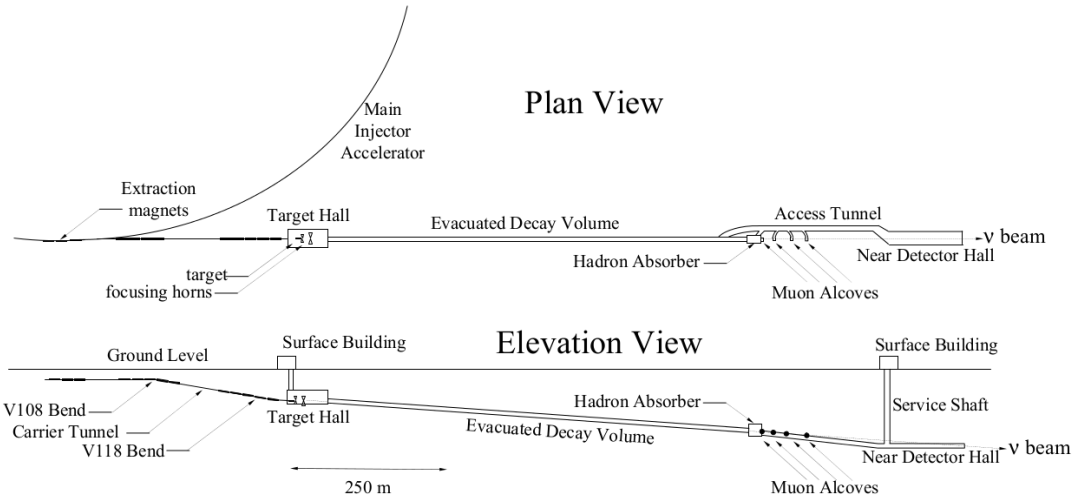

Figure 2.1: A scale diagram of the NuMI beamline. Plan and elevation views of the NuMI beam facility [34].

Pions and kaons are produced in the interaction of the proton beam with a fixed target. The decay of these mesons produces the neutrino beam used in MINOS, NoνA and MINERνA experiments. The branching ratios for those mesons which contribute significantly to the neutrino beam are

$$\pi^{\pm} \rightarrow \mu + \nu_{\mu}. \tag{2.1}$$

$$K^{\pm} \rightarrow \mu + \nu_{\mu}. \tag{2.2}$$

$$K^{0}_{L} \rightarrow \pi + \mu + \nu_{\mu}. \tag{2.3}$$

The beam is predominantly composed of muon neutrinos (92.9%), with a small component of anti-muon (5.8%), and electron and anti-electron (1.3%), neutrinos [31].

When the pions and kaons decay, muons are produced along with the muon neutrinos, these muons can be used to measure the number and energy spectrum of neutrinos delivered to the MINOS, NoνA and MINERνA experiments. An directly measurement of the neutrino flux will be a significant experimental challenge for the cross section measurements, and is almost a partial goal of

this thesis.

Inmediately following the target are two focusing magnets called horns [32]. Particles escape the target with some angular divergence with respect to the center axis of the beamline. The horns act as lenses, reducing beam divergence, focusing particles parallel to the beamline towards the MINOS detectors.

The horns have a focal length. This is proportional to the momentum of the charged particle. Those particles with a momentum matched to the focal length are most perfectly focused parallel to the beamline. The horns selects the peak energy of the neutrino beam.

Furthermore, depending on the polarity, the horns focus positively charged particles and defocus negatively charged particles, produce a predominantly muon neutrino beam, or focus negatively charged particles and defocus positively charged particles, produce a predominantly anti-muon neutrino beam [31].

During the first 2 years of operation, the horns in Medium Energy beam configuration were operated to produce a muon neutrino beam. All data used in the analysis discussed here were collected within the first 12 months (September 2013 - September 2014) of operation in Medium Energy.

The target and horns are contained within a 45 m long shielded enclosure. Immediately following this enclosure is a 2 m diameter and 675 m long decay volume. For the first 3 years of NuMI beam operation, the decay volume was evacuated. In November 2007 the decay volume was filled with Helium near atmospheric pressure. The purpose of the decay volume is to allow the focused mesons to decay in free space producing neutrinos. All kaons and most pions(95% at 5 GeV/c) decay before the end of the decay volume [31].

To stop the mesons that do not decay before the end of the decay volume, a hadron absorber is used. It is a block of Concrete, Steel and Aluminum immediately adjacent to the end of the decay volume. The hadron absorber removes all remaining hadrons from the neutrino beam. Those predominantly are protons that did not interact in the target and undecayed pions.

With the hadron absorber is contained an hadron monitor, which is an array of ionization chambers used to monitor the beam at the end of the decay volume. After the beam passes through the hadron absorber it is composed of neutrinos and muons produced alongside the neutrinos in meson decay.

Following to the hadron absorber are $\sim$ 300 m of unexcavated earth, it is

used to remove the mouns. This region is called the "muon filter" and is largely composed of dolomite rock.

The energy of the proton beam from the Main Injector is 120 GeV. Thus, the maximum energy of any muon is also 120 GeV. At this energy, about 200 m of rock is required for a muon to loose all energy by electromagnetic interactions with the rock.

Thus, after the muon filter the beam is solely composed of neutrinos. In the upstream portion of the rock, before all of the muons are removed from the beam, are three muon monitors.

The first muon monitor is located 7 m downstream of the hadron absorber and is separated from the hadron absorber by air. The other two monitors are located within alcoves excavated in the rock downstream of the first monitor.

The second monitor is separated from the first by 12 m of rock and the third is located after 18 m more of rock. At the end of the muon filter is the hall in which sits the MINERνA, MINOS Near Detector and the recent off-axis NoνA Near Detector.

2.1.1 The Graphite Target

The NuMI meson production target consists of 48 carbon graphite segments 6.4 mm wide, 18 mm high and 20 mm-long, the beam direction and spaced 0.3 mm apart. The total length of the target is 95.38 cm. There is a 48th target segment located $\sim$15.7 cm upstream of and rotated at 90° to the main target segments [31]. It is used for aligning the target with respect to the proton beam.

The length of the targer corresponds to 2 interaction lengths. This increases the fraction of the incident proton beam that will interact in the target and produces mesons which decay into neutrinos. However, even at this length approximately 13.5% of the proton beam will remain unreacted, escape the target and travel downstream to the hadron absorber. The length of the target also increases the number of reinteractions of particles produced in the primary interaction of the proton beam within the target. This has significat implications for the neutrino flux.

At $\sim$2.0 m upstream of the target is a 1.5 m long collimating baffle. The baffle is a carbon graphite cylindrical tube with outer diameter 30 mm and inner diameter 11 mm. The baffle protects the target cooling lines and horns

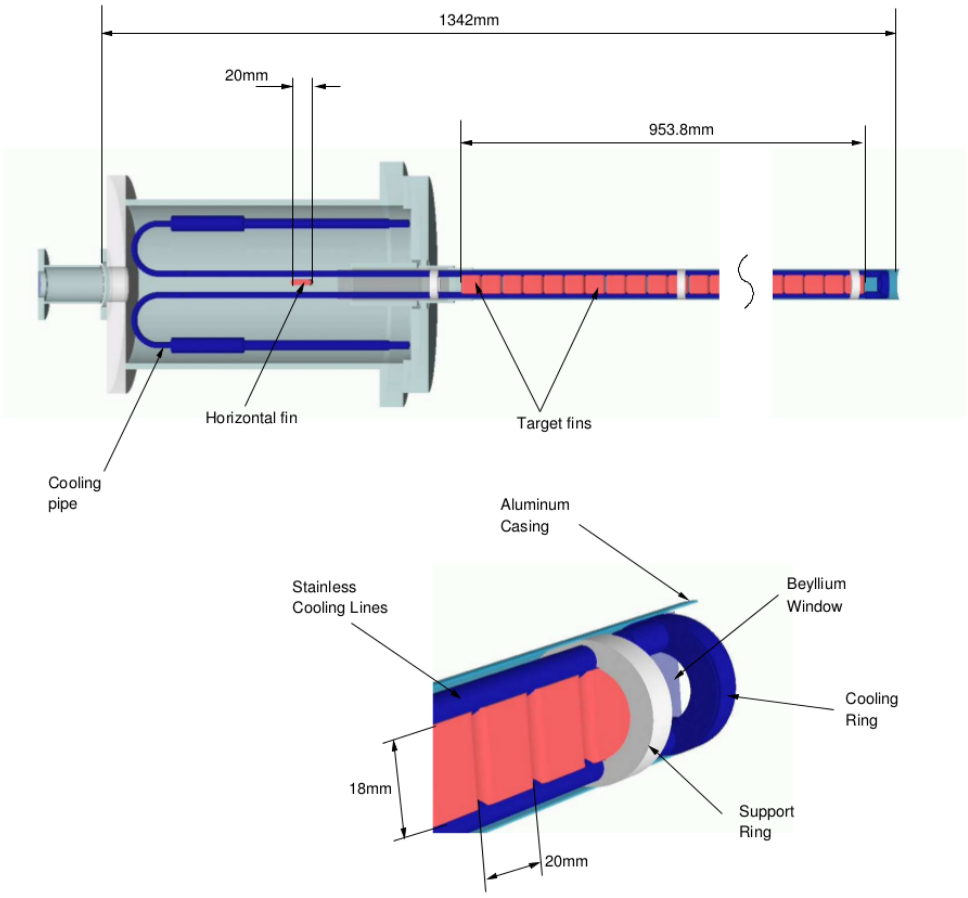

Figure 2.2: The NuMI hadron production target, the 120 GeV proton beam come from the left and interaction with graphite target produce mesons, which will decay producing neutrino.[32].

from misaligned proton beam that could damage these components.

The Figure 2.2 shown the NuMI Hadron Production Target. The target and baffle are mounted in a carrier which can move longitudinally with respect to the beamline center. This special ability of the NuMI beam line is important for the physics analysis discussed in this thesis because it changes the neutrino flux sent to the MINERνA Detector.

2.1.2 Magnetic Horns

Particles diverge from the target with some transverse p_T , and longitudinal p_Z, momentum as shown in the Figure 2.3. To increase the neutrino flux at downstream neutrino detectors it is desirable to remove this divergence and direct parent pion and kaons towards downstream detectors. The NuMI Beamline

uses horn focusing to accomplish this.

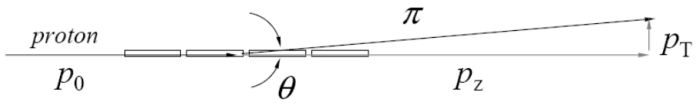

Figure 2.3: Particle diverging out from the target [32].

The NuMI particle focusing system consist of two parabolic horns positioned as shown in Figure 2.4. Those consist of a 2.54 cm thick outer conductor and a 0.2-0.5 cm thick inner conductor. Both conductors are made of Aluminum and the inner conductor has a parabolic shape following $z = ar^2$, where z is the longitudinal coordinate parallel to the axis of symmetry, r is the radial coordinate, and a is a constant parabolic parameter.

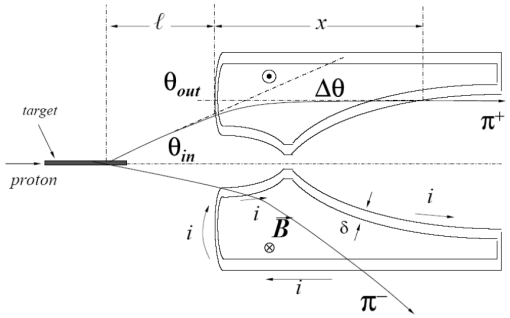

Figure 2.4: Lateral view of particles going through a focusing horn with parabolic shape of inner conductor. Due to the shape of the conductor, the particles entering at bigger radius will see greater Bdl resulting in a greater change in transverse momentum [34]. The squematic view is not at scale.

The first horn has an outer and inner diameter of 35 cm and 1.8 cm respectively, while the second horn is larger with an outer and inner diameter of 79 cm and 7.8 cm, respectively, so that it can intercept those particles not fully focused by the first horn.

The electrical current is applyed and it flows down the inner conductor and returns along the outer conductor. This generates a toroidal magnetic field between the conductors, as shown in the next equation

$$B(r) = \frac{\mu\theta I0}{2\pi r}, \tag{2.4}$$

where r is the radial distance from the symmetry axis. Ideally, there is no magnetic field outside of the region between the conductors. Thus, particles

emitted with very small divergence may pass through the field free region inside of the inner conductors of the horns (the "neck" of the horn) receiving no focusing.

The magnetic field of the NuMI beamline horns is measured using a hall probe before placing the horns in the beamline. The Figure 2.5 shows the measured magnetic field inside(13.5 mm - 150 mm) the first NuMI horn. The magnetic field shows the expected $1/r$ behavior and the expected, $\mu\theta I/2\pi r$, magnitude between the conductors. The field drops to zero outside of the outer conductor at $r > 150$ mm. The field inside of the inner conductor($r < 13.5$ mm) was measured separately and was found to be negligibly small [33].

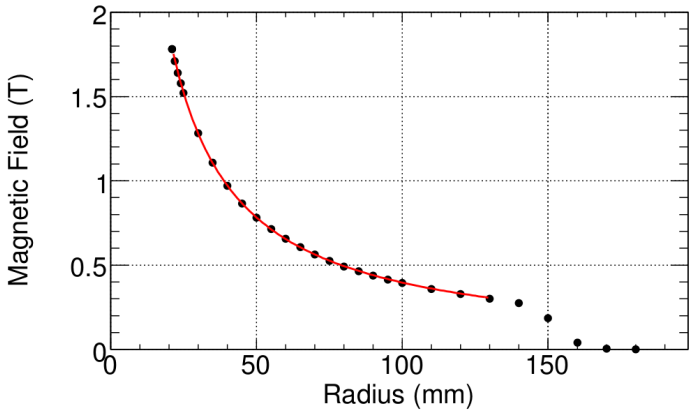

Figure 2.5: Magnetic field measured inside the first NuMI horn, it shows the expected $1/r$ dependence. The magnetic field drops to zero at $r > 150$ mm [31].

Particles traversing the region between the conductors feel a force, $q\mathbf{v} \times \mathbf{B}$, which directs them towards or away from the axis of the beamline depending on the sign of their charge, q. The Figure 2.4 shows a schematic of a particle entering a focusing horn through the parabolic inner conductor. Since the force on the particle is perpendicular to its motion, the resulting change in the particle's momentum is described by the change in direction as

$$|\Delta\theta| = |\theta_{out} - \theta_{in}| = \frac{|\Delta p_T|}{p}, \tag{2.5}$$

using the fact that $p_T \ll p$ and so, $\sin\theta \approx \theta$. The magnitude of the particles momentum change is

$$|\Delta p_T| = \int B(r)dl \approx \frac{\mu_0 I}{2\pi r} a r^2. \tag{2.6}$$

Perfect focusing occurs when $\theta_{out} = \theta$ so that $|\Delta p_T| = p_T$. In the approximation that the source is far from the horn, the focal length, f, of the horn

is

$$f \sim \frac{r}{\Delta\theta} = r\frac{p}{p_T} = \frac{2\pi}{\mu_0 I a}p. \tag{2.7}$$

This shows that the focusing power of the horn depends on the particle momentum and the current in the horn. The current in the horns selects the particle momentum that is most perfectly focused parallel to the beamline. Particles that pass through the necks of the horns are high energy and thus contribute to the high energy neutrino flux outside of the focusing peak.

It is also possible to change the peak energy of the neutrino beam while keeping the horn current fixed by varying the distance between the target and horns.

The flux of neutrinos with energies less than ~ 20 GeV comes mostly from the decay of pions. The typical angle of divergence of pions off of the target is

$$\theta_\pi = \frac{p_T}{p_\pi} \approx \frac{\langle p_T \rangle}{E_\pi} \approx \frac{280MeV}{\gamma m_\pi} = \frac{2}{\gamma}, \tag{2.8}$$

where γ is the relativistic boost factor and 280 MeV is the Fermi momentum of partons in a nucleon. This angle is larger than the typical divergence of neutrinos produced in pion decay, $\theta_\nu \sim 1/\gamma$. The flux of neutrinos at an angle, θ, with respect to the parent pion direction is given by

$$\phi_\nu \approx \frac{1}{4\pi}(\frac{2\gamma}{1+\gamma^2\theta^2})^2. \tag{2.9}$$

With respect to the center of the beam line, in the case of no focusing or a "bare target beam" $\theta = 3/\gamma$ and for the case of perfect focusing $\theta = \gamma$.

$$\frac{\phi_{focus}}{\phi_{bare}} = (\frac{1+\gamma^2\theta_{bare}^2)^2}{1+\gamma^2\theta_{focus}^2)^2} = \frac{1+\gamma^2(3/\gamma)^2)^2}{1+\gamma^2(1/\gamma)^2)^2} = \frac{100}{4} = 25 \tag{2.10}$$

The flux of neutrinos to downstream neutrino experiments is increased by a factor of 25 by removing the divergence of particles coming from the target.

2.1.3 Decay Pipe

Almost 30 m after the second horn, the evacuated decay pipe begins. The purpose of the decay pipe is to allow pions and kaons to decay in free space unobstructed by interactions with matter. It is true that the majority of pions and kaons that contribute to the neutrino flux at the MINERνA and MINOS Near Detector decay freely in the decay volume.

However, as the horns only provide perfect focusing for single particle momentum, off-momentum particles receive partial focusing and still have some angular divergence. This angular divergence may be large enough that the particle does collide with the walls of the decay pipe.

Particles produced in the interactions with the walls, produce neutrinos which contribute to the neutrino flux at the MINERνA and MINOS Near Detector. This is a source of uncertainty in physics analyses [31].

2.1.4 Hadron Monitor

The hadron absorber is located at the end of the 675 m long decay volume. Its purpose is to remove hadrons remaining in the beam at the end of the decay pipe in a controlled manner. A breakaway view of the hadron absorber produced from the GEANT4 beam Monte Carlo is shown in Figure 2.6.

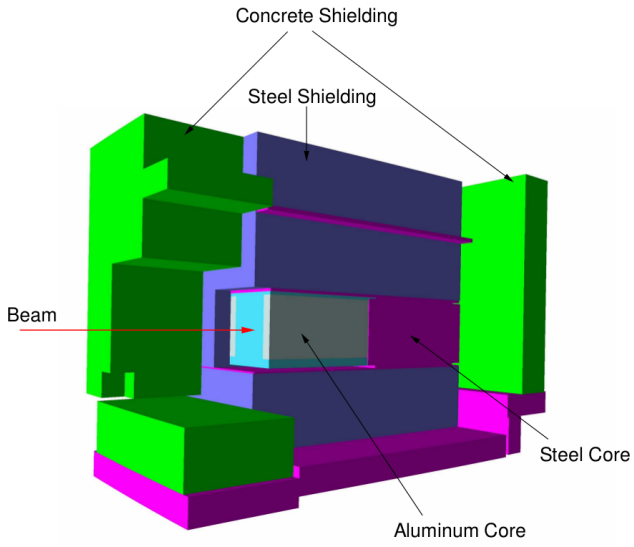

Figure 2.6: Hadron Monitor created on GEANT4 as implemantation on the geometry. The Aluminum core is 2.4 m long and the following steel core is 2.3 m long [31].

It has an inner most core composed of Aluminum and steel surrounded by steel shielding blocks. The aluminum and steel core is further surrounded by concrete blocks. The metal core serves to simultaneously create and contain hadronic showers. Neutrons from these showers are attenuated in the outer concrete shielding. Further discussion and details of the hadron absorber ge-

ometry can be found in the main reference (used to the beamline Section [31]).

2.1.5 Muon Monitors

After passing through the hadron absorber the beam contains only neutrinos and muons produced from the decay of mesons in the decay volume. By the time the beam reaches the downstream neutrino detectors, it must only contain neutrinos. The region downstream of the hadron absorber but before the MINOS Near Detector hall is designed to remove muons from the neutrino beam and is thus referred to as the muon filter.

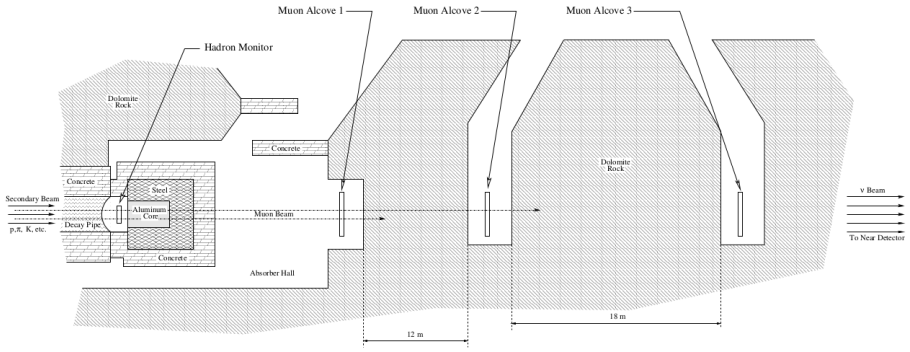

Figure 2.7: Lateral view scheme of the muon monitors.

In the Figure 2.7 is shown a side view of the muon filter. It consists of about 300 m of unexcavated earth with the exception of four excavated muon alcoves. The three most upstream alcoves each contain a muon monitor that is used to monitor the muon beam and measure the muon flux.

The earth is a composition of Dolomite rock and Maquoketa Shale. For the maximum energy muon of 120 GeV, about 200 m of rock is required for a muon to loose all energy by electromagnetic interactions with the rock. Hence, the 300 m of rock between the hadron absorber and the MINOS Near Detector Hall is sufficient to ensure that the MINERνA and MINOS detectors are not overwhelmed by beam muons, but rather can record neutrino interactions.

The muon monitors are located within excavated alcoves downstream of the hadron absorber. Since they are located downstream of the hadron absorber, the flux of particles through the muon monitors is dominated by muons produced along with the neutrinos in the decay of pions and kaons in the decay pipe.

Like the hadron monitor each muon monitor is a 9 by 9 array of ionization chambers. Each muon monitor is separated from the decay pipe by successively more shielding. The shielding imposes a momentum threshold for muons to reach each monitor of about 4, 11, and 21 GeV/c, for alcoves 1, 2 and 3, respectively. This is to say that muons produced in the decay pipe with momenta less than 4(11)21 GeV/c will range out in the hadron absorber and never intercept muon monitor 1(2)3 [31, 32, 33].

Thus the muon monitors measure an integral of the muon flux above each of these thresholds. A key role of the muon and hadron beam instrumentation is the verification of the neutrino beam performance. As described in the references [31, 32, 33] precises manipulation of the proton beam can, when combined with measurements of particle fluxes in these downstream detectors, be utilized to align the target and magnetic horns.

2.1.6 Variable Energy Beam

From the Equation 2.7, the magnetic horns have a variety of focal lengths for particles with different momenta. The average momentum of focused particles is fixed by the longitudinal placement of the target with respect to the horns.

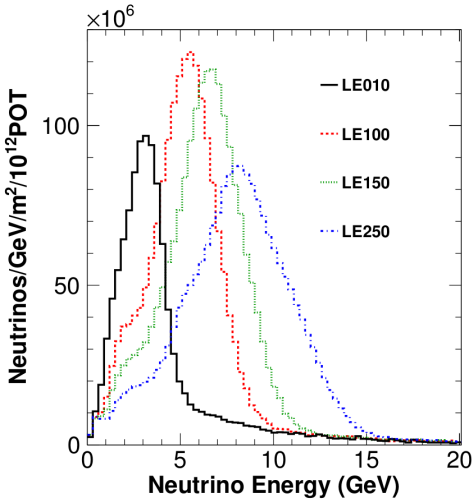

Figure 2.8: Monte Carlo simulation of the neutrino flux at the MINOS Near Detector in the LE010, LE100, LE150 and LE250 beam configurations. The peak energy of the neutrino flux increases as the target is moved away from the horns [31].

In the NuMI beamline, the average momentum of focus particles can be

varied by changing the separation between the target and horns. This locates a different portion of the target at the focal length of the horns, effectively changing the focal length of the horns.

As the typical divergent angle of pions out of the target is $2/\gamma$, higher momentum pions diverge less than to lower momentum pions. Thus, increasing the relative difference between the target and horns results in higher momentum pions receiving full focusing. A higher momentum pion beam directly results in a higher energy neutrino beam.

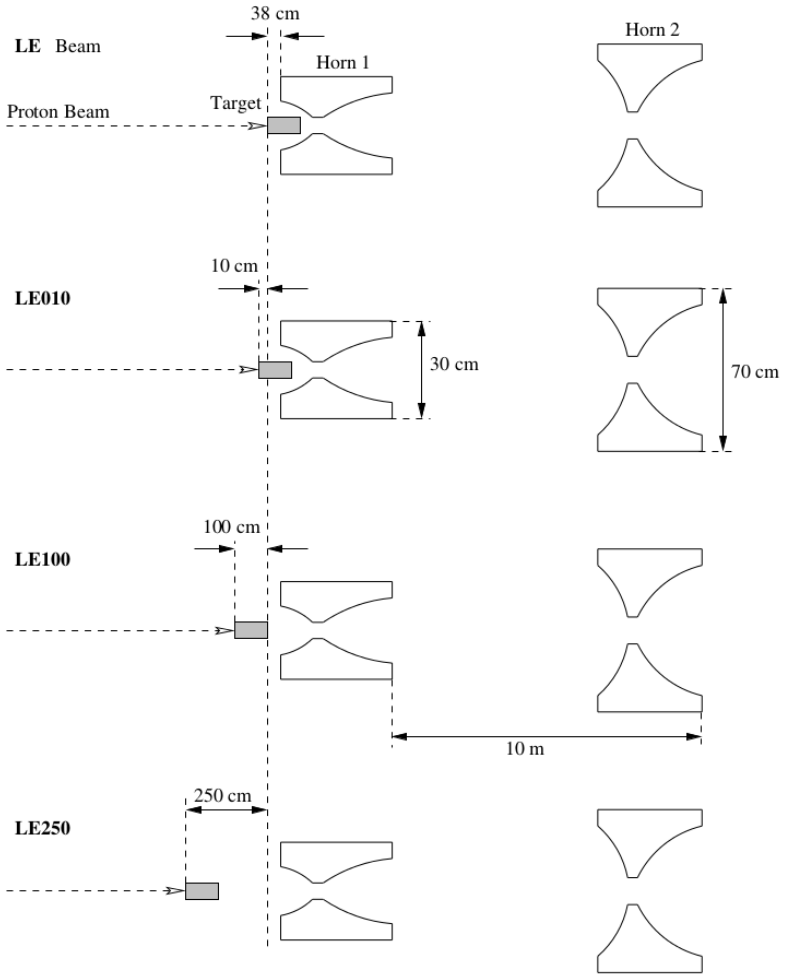

Figure 2.9: Four of the five target-horn configurations in which the NuMI beam has operated to produce different energy neutrino beams [31].

The target and baffle are mounted in a carrier on rails. The system may travel a maximum distance of 2.5 m along the rails. Figure 2.9 shows four of

the five target-horn configurations in which the NuMI beam has operated to produce different energy neutrino beams.

In the nominal configuration, LE or LE000, the target is inserted about 35 cm into the first horn. The LE000 configuration produces the lowest possible neutrino energy beam. Higher energy beams are produced my moving the target away from the horns. In principle the target may be positioned at any distance with respect to the horns up to 2.5 m. The Figure 3.1 shows the Monte Carlo simulated neutrino flux at the MINOS Near Detector in the LE010, LE100, LE150 and LE250 beam configurations. The peak energy of the neutrino flux increases as the target is moved further from the horns.

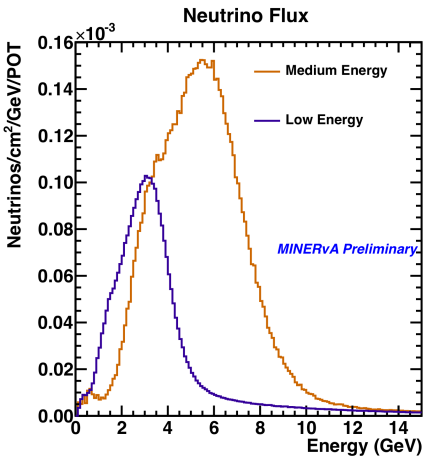

Figure 2.10: Low Energy and Medium Energy neutrino fluxes for Forward Current Horn configuration.

The ability of the NuMI beamline to produce a variety of different energy neutrino beams is essential in understanding the neutrino flux.

The MINERνA Experiment has been taking data just in two configuration: Low Energy (LE) and Medium Energy (ME). The LE period spans from March 2010 to July 2012. Now the Medium Energy period is running, the runs started on September 2013. The Figure 2.10 shows the LE and ME fluxes.

Figure 2.11 shows a draw of the beamline with all the main components on different views.

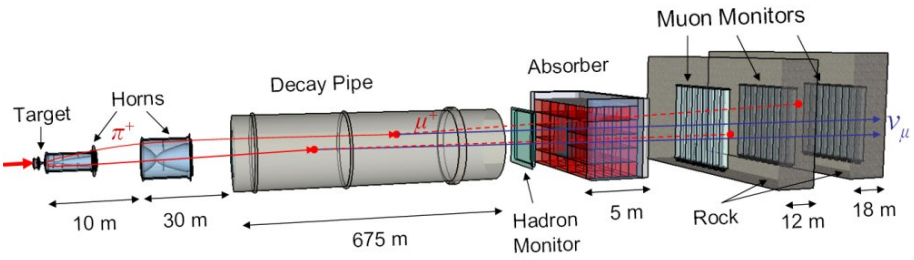

Figure 2.11: NuMI Beamline.

2.2 The MINERνA Detector

The MINERνA Detector was designed to allows the detection of multiple particles in the final state, identify such particles, the track of the charged particles, the energy contained on the electromagnetic and hadronic calorimeters via showers and a time resolution capable to distinguish multiple interactions in a single beam spill.

To study A-dependence of several process, a nuclear target region with different passive targets was designed as weel. On the Figure 2.12 an schematic representation of the MINERνA Detector is shown.

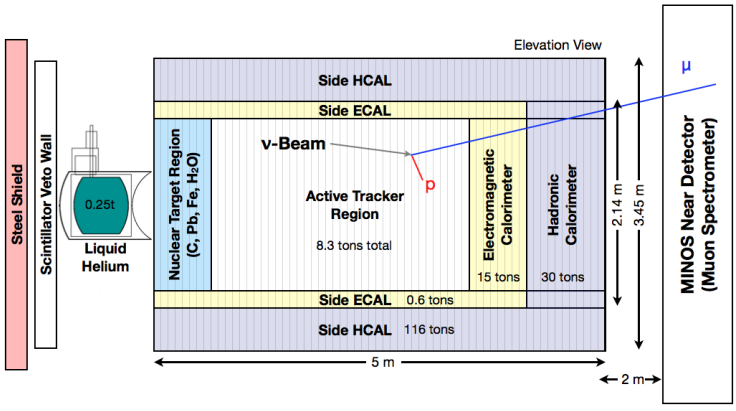

Figure 2.12: Squematic side view of the MINERνA Detector. No to scale. We can see all the major components: Veto Wall, Cryogenic Target, Nuclear Target Region, Traker Region, ECal and Hcal, side Ecal and Hcal and the MINOS Near Detector.

The description of the components of MINERνA Detector following the neutrino beam direction, i.e. from upstream to downstream is in the following Sections.

2.2.1 Veto Wall

The veto wall consists of a 5 cm thick steel plate, a 1.9 cm thick scintillator plane, a 2.5 cm thick steel plate, and another 1.9 cm thick scintillator plane. It can be seen from the Figure 2.12, the veto wall is located at the front of the MINERνA Detector, inmediatly behind the Steel shield.

The veto wall is designed to shield the detector from low energy hadrons and tag muons created by neutrino interactions in the surrounding cavern rock (such particles are referred to as "rock muons" in this thesis).

2.2.2 Nuclear Target Region

The Nuclear Target Region are composed by 22 tracking modules and 5 solid pasive targets modules. To get the reconstruction of the events generated in the targets, four tracking modules are located between the solid targets.

The Figure 2.13 shows an schematic view of the Tracker Region.

The pasive targets are numerated from upstream to downstream, 1 to 5, the composition of these targets is a combination of segments of Carbon, Iron and Lead.

Thicker targets are the most upstream, so that they interfere with fewer final state products from interactions in other targets [36].

Targets 1, 2, and 5 contain Iron and Lead, which are divided diagonally on a 20.5 cm offset from the center of the hexagon. Target 3 is made of Carbon, Iron, and Lead; which occupies is 1/2 , 1/3 and 1/6 of the area of the module-target, respectively. Target 4 contains only Lead. Each target has some unique features.

- Target 1: Being the most upstream target, it makes Target 1 difficult to analyze. The primary difficulty is the small number of upstream tracking planes which can be used to identify particles produced outside of MINERνA. To solve this problem, the veto wall has been improved in this target.

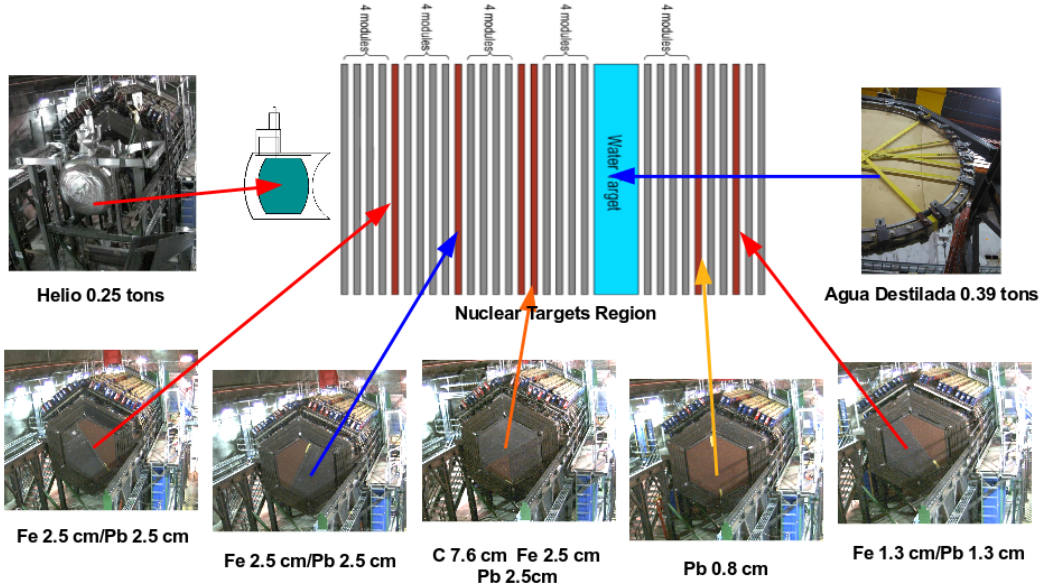

Figure 2.13: Scheme of the Target Region, not to scale. And actual pictures of each target.

- Target 2: The orientation of Iron and Lead is flipped horizontally from that of Target 1.

- Target 3: The carbon slice is three times as thick as the Iron and Lead, which are the same thickness as the Iron and Lead in Targets 1 and 2. All materials are flush at the upstream end, so that there is an air gap downstream of the Iron and Lead.

- Target 4: This is much thinner than the other targets. It is intended to induce electromagnetic interactions of particles from the upstream targets before they enter the low Z tracking region. These, both improve the containment of events in the upstream targets and reduce the noise from n, γ, and π^0, which would confuse event selection in the tracking region [36].

- Target 5: Target 5 has the same shape as Target 1 but is half the thickness. As the large, fully active tracking region is immediately downstream of this target, tracking is a bit more precise than in other targets.

There is an air gap between Targets 3, 4, and 5 and the first scintillator plane downstream of them, which is beneficial for reconstruction because it allows for greater spatial separation of low energy hadronic final state particles.

The Figure 2.14 shows the configuration of the target-modules.

Figure 2.14: Configuration of the target-modules, from left to right: U-$[Pb/Fe]_1$, UV-$[Pb/Fe]_2$, UV-$[Pb/Fe/C]_3$, UV-$[Pb]_4$ and UV-$[Pb/Fe]_5$ [39].

Water Target

A water target is positioned between solid targets 3 and 4, with a mean position of 530.8 cm. It consists of a circular steel frame with a diameter slightly larger than the MINERνA inner detector size, and Kevlar (polymerized C14H10N2O2) sheets stretched across the frame as shown in the Figure 2.15.

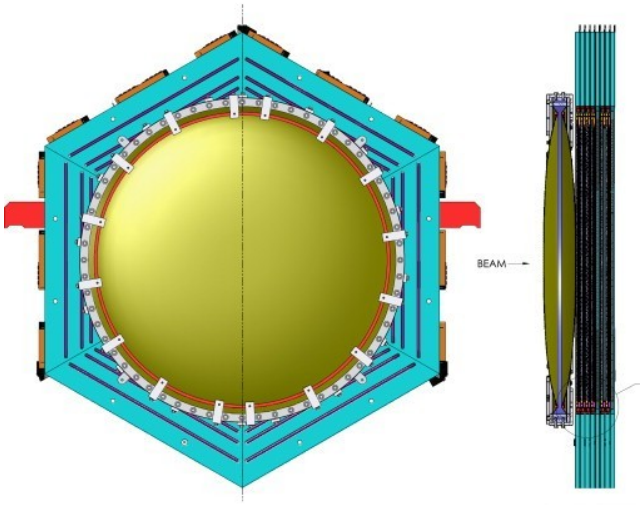

Figure 2.15: Front and side view of the Water Target [49].

The shape of the water target is not as well known as that of the solid targets. When the target is filled the lower part expands more than the upper part, and it is not possible to access the entire target in order to make precise measurements. The water target chemical composition by mass is 88.5% Oxigen and 11.1% Hydrogen with negligible amounts of C and N [38].

Helium Target

The cryogenic helium target is located immediately upstream of the active detector and was filled with liquid Helium during the begin of 2014.

The cryogenic target consists of an Aluminum cryostat capable of holding approximately 2300 l of cryogen. The cryostat consists of an inner vessel containing the cryogen, which is thermally isolated from an outer vacuum vessel, and which hangs from a set of four Kevlar ropes.

The vacuum region contains layers of thin Aluminum baffles for minimizing the radiative heat transfer from the inside of the outer vessel to the inner vessel.

The inner vessel itself consists of a cylinder with an inner diameter of 152 cm, length of 100 cm, and a wall thickness of 0.635 cm. The ends of the inner vessel are capped with 0.635 cm thick. The outer vessel cylinder has an inner diameter of 183 cm and a wall thickness of 0.952 cm.

In order to minimize energy loss and rescattering of final state particles entering MINERνA, the amount of Aluminum on the downstream end of the cryostat was minimized in the design.

Consequently, the flanged and dished head on the upstream end has a thickness of 0.635 cm, while the hemispherical head on the downstream end has a nominal thickness of 0.160 cm and a radius of curvature of 107 cm with the center of curvature downstream.

Since the equation of state for helium is known, the temperature and pressure sensors allow an accurate determination of cryogen density. The temperature is regulated to within 25 mK via a feedback loop which controls a heater.

On the Figure 2.13 a picture of the Helium target is shown.

2.2.3 Tracker Region

Behind the nuclear target region there is the heart of the MINERνA Experiment: The Tracking Region.

The Nuclear Region contains 22 tracking modules, and the central Tracking Region contains 62 tracking modules.

The tracking modules consist of two scintillator planes, each plane is composed by triangular scintillator strips. And each plane consists of 127 strips glued together with translucent epoxy. Sheets of Lexan cover the planes and are attached with gray epoxy to make them light tight and to add rigidity.

Black PVC electrical tape is used to seal joints in the Lexan and patch any light leaks. On the Figure 2.16 is shown a transversal section scheme of the tracking planes.

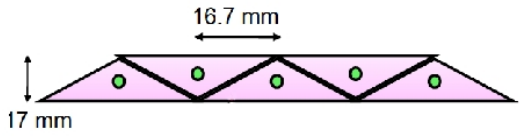

Figure 2.16: Transversal view of one tracking plane.

Optical epoxy provides the coupling between the scintillator and WLS fibers.

The scintillator plane can have one of three different orientations, referred to as X-planes, U-planes or V-planes, according to the coordinate in the MINERνA system in which each plane measures particle hit positions.

As shown in the Figure 2.17, the X-planes have scintillator strips aligned vertically, hence hits in this view give position information in the horizontal or x-direction. The U- and V-planes are rotated 60 degrees clockwise and counterclockwise from the X-planes in the x-y plane, respectively.

Three different views are used in order to avoid ambiguities with reconstructed hit associations that can occur when multiple tracks traverse two orthogonal planes.

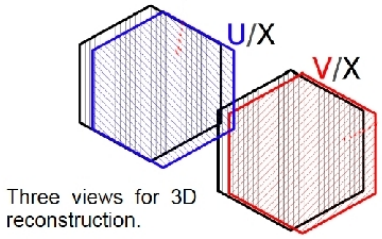

Figure 2.17: Three orientations of the scintillator strips on tracking planes.

The chemical composition and areal mass (mass per unit area) of the planes is determined by combining measured densities (pure scintillator and coated

strips), as sayed compositions (coated strips and epoxies), and data sheet values (tape and Lexan).

The estimated areal mass densities of the epoxy and tape are based on their usage in plane construction. The chemical composition of the components is well known. There is some uncertainty in the composition of the coated strips due to the uncertainty in the coating thickness, which is estimated to have a relative uncertainty of about 10%. This affects most strongly the fraction of the strips which is scintillator [40].

The estimated areal density for the scintillator plane is 1.65 ± 0.03 g/cm^2. The estimated areal density of an assembled plane is 2.02 ± 0.03 g/cm^2.

More information about the density and composition in the scintillator planes, is in the paper "Calibration, and Performance of the MINERνA Detector" [40].

2.2.4 Electromagnetic Calorimeter

Each module on the tracking and electromagnetic calorimeter (ECal), has one X-plane, and either, a U- or V-plane, with modules alternating between a UX or VX structure with the X-planes always located downstream of the U- or V-planes.

The Ecal modules are very similar to a central tracking module. It differs in that it has a 0.2 cm thick sheet of lead covering the entire scintillator plane instead of a 0.2 cm thick lead collar covering only the outer edge of the scintillator region.

Between the Tracking and ECal Region are located transition modules, this region contains a 0.2 cm thick lead sheet on the downstream end of the last plane in the module, so that each plane of the ECal has a lead absorber upstream of it.

The fine granularity of the ECal ensures excellent photon and electron energy resolution and provides directional measurement for these particles. There are 10 modules in the Ecal region of the detector [40].

2.2.5 Hadron Calorimeter

The lead sheets used for the side electromagnetic calorimetry were measured using an ultrasonic device to determine the variation in thickness along the length of the sheet. The thickness along each piece vary at the 5% level, and the average thickness of the different pieces vary at the 3.5% level.

The thicknesses of the lead sheets used in the downstream electromagnetic calorimetry also vary at this level. The Hcal consists of 20 modules that are similar to the tracking modules; however, instead of two planes of scintillator in each module, there is only one plane of scintillator and one 2.54 cm thick hexagonal steel plane in the inner detector region.

The scintillator planes located in the HCal have a repeating pattern of XVXU.

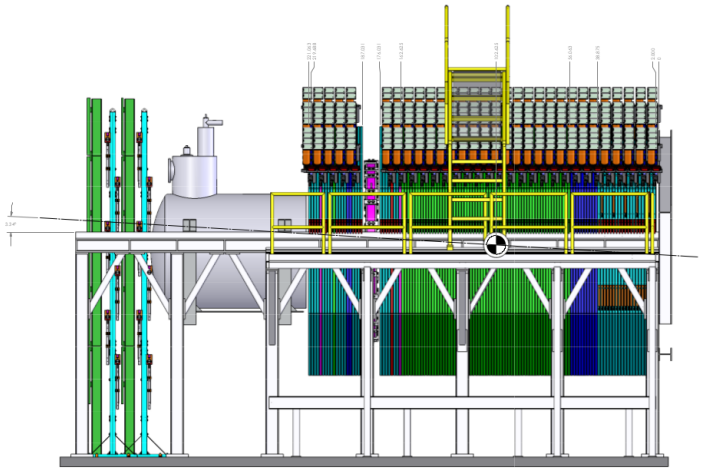

Figure 2.18: Side view of the actual state of the Minerva Detector. From left to right; veto modules, Helium target, Target Region, water Target, Tracker Region in light-green, ECal Region in blue and HCal Region in dark-green.

2.2.6 Side Electromagnetic and Hadronic Calorimeters

The tracking modules are designed to perform electromagnetic calorimetry using a 0.2 cm thick lead collar that starts at roughly 90 cm from the module center and extends to the outer frame. The collar forms a hexagonal ring whose purpose is to reduce the leakage of electromagnetic showers that originate in the central detector.

The Side HCal has 5 trapezoidal Iron blocks, it increases gradually untill reaches a thick of 43.4 cm, and it is separated by 4 scintillator strips of 2.5 cm of thick, like the ECal.

The Side Calorimeters design allows a complete particle contain and a high resolution for angles below 25°. On the Side Calorimeter is possible to stop protons with energy under 750 MeV when it enters at orthogonal angle with respect to detector longitudinal direction.

The Figures 2.18 and 2.19 show the profesional draws of the MINERνA Detector from different views. The draws are in the minerva-docdb webpage.

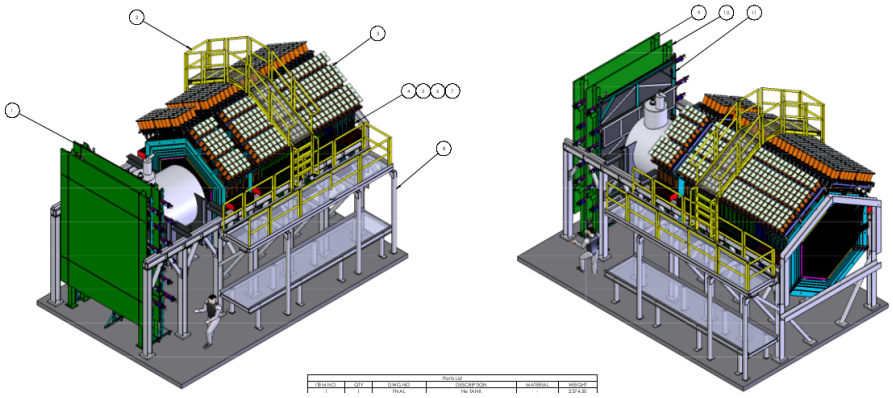

Figure 2.19: Left: Front-right corner view. Right: Back-right corner view.

2.2.7 Optical System

The MINERνA Detector is composed from around 32 000 scintillator strips, this means, the same number of channel must be converted to electrical pulses, each pulse carries the accurate information related to the energy deposited and timing information.

When charged particles pass through the individual scintillator strips generate light, this light is collected in wavelength shifting fibers at the center of each bar and transmitted through clear optical cables to 64-anode photo- multiplier tubes (PMTs) mounted above the detector.

Each PMT is enclosed in a metallic cylindrical box, inside it an additional set of fibers called "ODU" is contained, it guides the light to the front face of the PMT. Each box also houses the associated PMT base. The front-end electronics board that services the PMT is mounted to the exterior of the box

on one endplate.

MINERνA Detector uses extruded plastic scintillator technology for the tracking detectors in the Inner Detector (ID), and embedded scintillators in the Outer Detector (OD). The blue-emitting extruded plastic scintillator strips are read out with a green wavelength shifting (WLS) fiber, it is placed in the center of the strips.

The extruded scintillator strips are made from polystyrene pellets doped with 2,5-diphenyloxazole (PPO) and 1,4 bis benzene. This scintillator composition was previously utilized in the MINOS scintillator strips. PPO and POPOP are used for their spectroscopic properties. The strips are co-extruded with a white reflective coating based on TiO_2 in polystyrene [40].

The ID scintillator strips has a triangular cross section, with a height of 17 ± 0.5 mm and width of 33 ± 0.5 mm, see the Figure 2.20. Each ID strip has a 2.6 ± 0.2 mm diameter hole centered at 8.5 ± 0.25 mm above the widest part of the triangle.

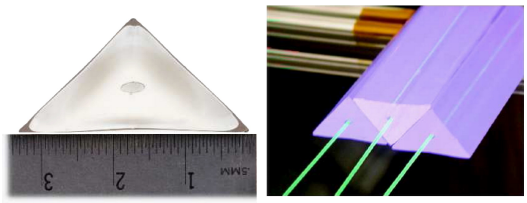

Figure 2.20: Left: Scintillator strips used on MINERνA Detector, these have a triangular cross section. Right: Configuration of the planes by stacking extruded triangular strips, the WLS fiber collect and send the to the PMTs the light generated by a charge particle interaction [48].

Both ends of the scintillator strips are painted with white TiO_2 Eljen paint. The OD scintillator strips have two different rectangular cross sections. For 90% of the detector the OD scintillator strips have a base of 19 ± 0.5 mm and a height of 16.6 ± 0.5 mm. For the hadron calorimeter region the OD steel is thicker, hence the OD scintillator strips are also thicker to improve hermeticity. The OD scintillator strips have a 3.5 ± 0.2 mm diameter hole [40].

2.3 MINOS Near Detector

The MINOS Detector is located on the Fermilab site 100 m underground and 1 km from the NuMI target. It is a sampling calorimeter composed of alternating planes of 1 cm thick scintillator arranged in planes of strips and 2.45 cm thick steel planes. It is designed to measure the momenta of muons produced in charged current muon neutrino interactions, $\nu_\mu + Fe \rightarrow \mu^- + X$.

The detector is magnetized allowing for the separate identification of μ^+ and μ^- from ν_μ and anti-ν_μ charged current interactions, respectively. This also allows for a measurement of muon momentum by the curvature of the muon track.

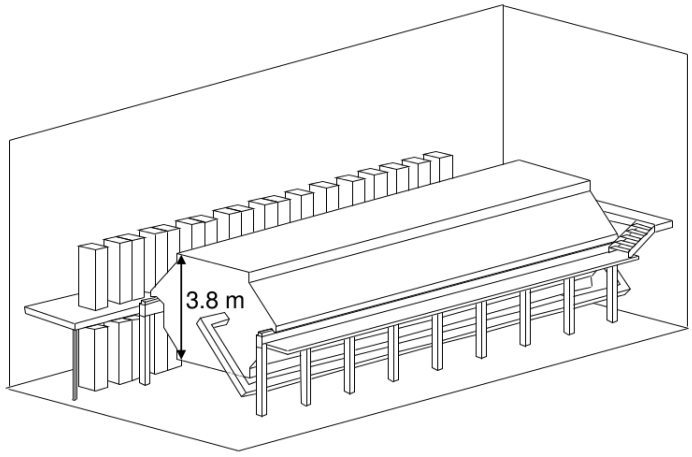

Figure 2.21: Scheme of the MINOS ND, it is used as muon spectrometer.

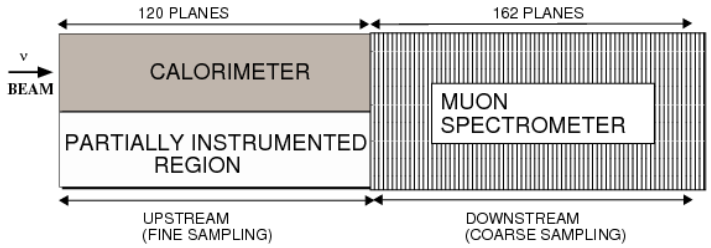

Figure 2.22: Top schematic view, showing the calorimeter and muon spectrometer. The drawing is not at scale [49]

The energy of the hadronic state, X, is measured calorimetrically. The Figure 2.21 shows a diagram of the 980 ton MINOS Detector. It is a "squashed" octagon ∼3.8 m in diameter and 16.8 m long. The steel-scintillator planes are spaced 5.95 cm center-to-center for a total of 282 planes.

The planes alternate in +45°, called U, and -45°, called V, orientation with respect to the horizontal direction. The upstream 120 planes comprises the calorimeter portion of the detector. All planes are instrumented to measure hadronic showers produced in neutrino interactions. The downstream 162 planes form the spectrometer section. Every 5th plane is instrumented to track muons produced in muon neutrino interactions.

The magnetic coil is offset from the center of the detector by approximately 0.56 m. The neutrino beam is centered on the left side of the detector between the left edge and the coil.

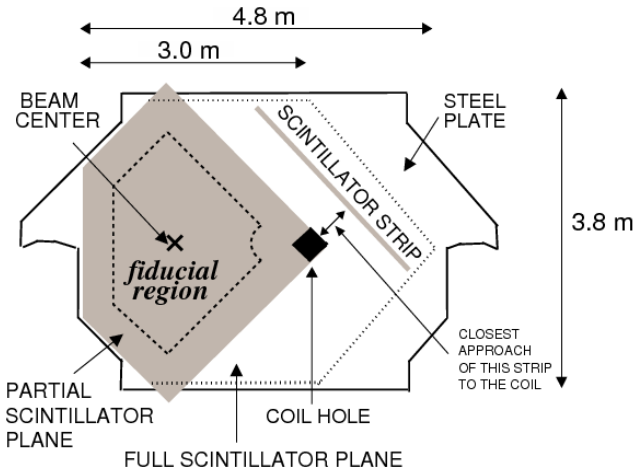

Figure 2.23: Transverse view fo the MINOS Near Detector. The shaded area shows a partially instrumented active scintillator plane and the dashed line within shows the boundary of the fiducial region. And the dotted line shows the outline of a fully instrumented scintillator plane.

Figure 2.24 shows a diagram of a MINOS scintillator strip and demonstrates the scintillation process. Each polystyrene scintillation strip is 4.1 cm, 1.0 cm thick and up to 6 m long (in the Near Detector) and coated with a titanium-dioxide (TiO_2) doped polystyrene reflective layer to maximize reflection and protect the strip.

A wavelength shifting (WLS) fiber is inserted into a 2.3 mm deep grove cut into the wide face of the strip. Charged particles ionize the scintillator producing scintillation light at a characteristic 420 nm. The WLS fibers absorb radiation peaked at 420 nm and re-emit light at 470 nm. The light travels along the length of the fiber to the end where it impinges upon a photo-multiplier tube (PMT). Each strip is connected to one PMT pixel. Only one end of each strip is readout, the other end is coated with a highly reflective material.

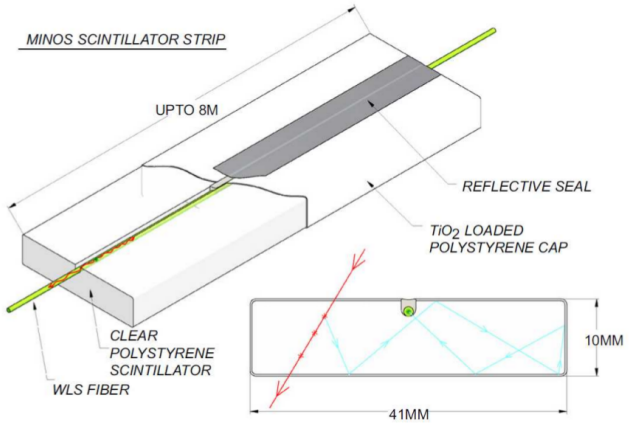

Figure 2.24: Diagram of a MINOS scintillator strip showing the outer TiO_2 coating and WLS fiber. Scintillation light reflects within the scintillator until it is absorbed by the WLS fiber. Light is re-emitted by the fiber and travels down its length to the collector system [31].

2.4 Test Beam Program I and II

The goal of the test beam experiment is to measure how well the Monte Carlo (MC) simulation of the detector responses to these particles and how well describes the data. The accuracy of the simulated single-particle response is an essential ingredient to the MINERvA neutrino cross-section measurements.

The Test beam Detector was proposed to study the hadronic and electromagnetic response on a miniature replica of the MINERVνA Detector, and it is used for calibration. It is 1 m in the transverse dimension, about half the size as MINERνA Detector, and one-third the depth.

On the Test Beam I, the energy range covered was 0.35 - 2.0 GeV, it is well matched to the energy range of protons, pions, and electromagnetic showers in the data taked from 2010 to 2012, i.e. at MINERνA Low Energy neutrino and antineutrino data.

Now, Test Beam II is in operation and it covers an energy range from 1.77 Gev to 8 GeV, these are the predictions for the range of protons, pions and electromagnetic showers in the MINERνA Medium Energy run.

The Test Beam Experiment was developed at the Meson Test Beam facility

(MTest). This facility works with a beam coming from the collision of protons extracted from the Main Injector at 120 GeV on a target of Aluminum, the products of the interaction are directed towards MTest in the two operation modes: protons and pions.

The not interacting proton beam is mostly absorbed by a pinhole collimator, and the beam remainder is transported directly to MTest, while on the pions beam mode, the momentum selection is made with dipole magnets located along the beam line. It can provide pions at different energies, below of 1 GeV the beam content are electron and positrons coming from the decays or showers.

When the secondary beam (pions at 16 GeV) hits the copper target, is generated a tertiary beam from the products of the interaction, the remain of the secondary beam is also spread in the room.

Even although secondary and tertiary beam are not on time, this enables to separate the two signals to a zero level, the secondary beam is absorbed in order to maintain low levels of radiation. By this means, a sensor chain is installed on the detector, that is not exposed to a unnecessary contamination.

On the Figure 2.25 is shown the eye-bird view scheme of the test beam array.

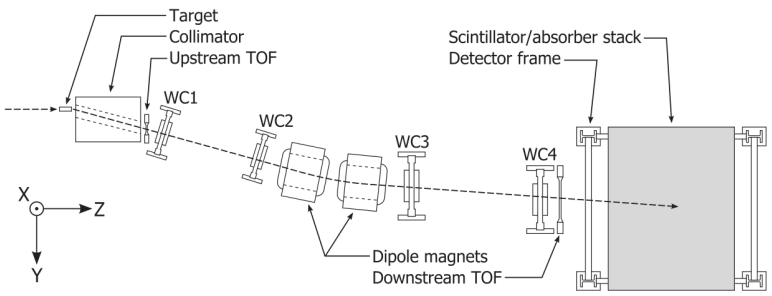

Figure 2.25: Diagram of the Test Beam Experiment array for Run I, viewed from above, with the beam comming from left to right [40].

2.4.1 Tertiary Beam

The Test Beam Experiment uses a tertiary beam, this means, that the beam is extracted from the interaction of the secundary one produced on a copper target.

The motivation to have a tertiary beam is because the secundary beam (pions at 16 GeV) not covers the requierements of the Test Beam Experiment, it

necesary a beam with an specific energy range.

These were the beam requierements for the Test Beam I:

- Electrons, positrons, pions and protons with an energy range between 0.35-2.0 GeV.
- Good balance in the events rate, to have a good response of the DAQ (Data Adquisition Quality System).
- To have an specific particle type per run, with the low contamination possible.

2.4.2 Test Beam Line

The Test Beamline is composed by one production target, Iron collimator, time of flight (tof), magnetic spectrometer, four wire chambers and the Test Beam Detector.

The Figure 2.26 shows the test beamline from two different views.

Figure 2.26: Test beamline. Left: Lateral view. Righ: Front-Uper view [39].

2.4.3 Copper Target

The target type depends of the secondary features, on the Test Beam Experiment, the Copper was chosen, because it has low activity.

The Copper target has trapezoidal shape, with 30.48 cm of length, and 3.17 of thick. It was at 166.4 cm above the floor. The Copper target is shown on the Figure 2.27.

Figure 2.27: Copper target.

2.4.4 Collimator

When the beam hits the Copper target, many particles are produced (tertiary beam), to choose the appropriate beam, an Iron Collimator are been installed, it choose particles at 16° respect to the secundary beam direction.

The coper target is located just front the collimator, the dimensions of pinhole in the collimator are Front, (7.63×5.08) cm and Rear, (14.50×5.08) cm. A lateral view of the collimator, target and TOF are shown in the Figure 2.28.

Figure 2.28: Collimator with Copper target in the front.

2.4.5 Drift-Wire Chambers

The reconstruction of the trajectories and angle measurements were done with four wire chambers, that were the same used previously in the Hiper CP Experiment.

The wire chambers have the same features. One of the four wire chambers are shown in the Figure 2.29.

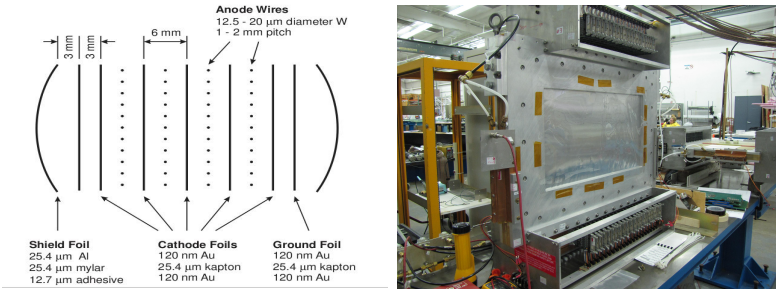

Figure 2.29: Left: wire chamber scheme. Right, picture of the wire chamber [39].

2.4.6 Magnets

The magnets type "NDB" made at Fermilab, are ramped to a current of 100 A producing a magnetic field of 0.339 Tesla in the central region of the magnet, the polarity can be reversed. The typical field integral is 38.3 Tesla cm with 1.5 Tesla cm variations around this value that encompass 90% of selected events [40].

The magnets were built by two coils of 200 turns each, the layer core of the magnet is made with Iron, each layer has a thick of 3 mm and each magnet weight is 772 kg.

The dimensions of the cavern in the magnet, where cross the charged particles, are 20.95 cm, 14.73 cm and 46.4 cm for width, high and length, respectively [39].

At normal operating conditions the magnets have an inductance of 297 mH, and the temperature of the core oscillates around 133.8 ° C.

The Figure 2.30 shows the pictures of the two magnets used at Test Beam Experiment.

2.4.7 Time of Flight

The TOF units, 1 and 2, are used to measure the time the particle travels from just in front of the first wire chamber to just behind the last wire chamber. The path length is 6.075 m with RMS variations of 0.014 m from center to inside and outside tracks through the bend magnets.

The front TOF unit is a single piece of inch-thick scintillator. The back unit

Figure 2.30: NDB0022 and NDB0021 magnets before used in the Test Beam Line.

is three longer pieces of inch-thick scintillator, covering an area larger than the wire chamber aperture.

A resolution of 200 ps is obtained using fast photo-multiplier tubes (PMTs) reading out two sides of each scintillator and a 25 ps least-count time to digital converter. The photo-electron yield, scintillator size, and length of signal cables contribute to this resolution [40].

2.4.8 Test Beam Detector

The test beam detector is a miniature version of the MINERνA Detector. The Test Beam Detector is made of 40 square planes of 63 nested triangle-shaped scintillator strips, each one with length of 107 cm and 1.7 cm of thickness.

As a remainder, the MINERνA Detector has a hexagonal cross section and it is made of 124 planes of 127 strips in the Tracker Region, 20 planes in the Ecal and Hcal, which have Lead and Iron interleaved respectively.

Both detectors have the same three views, with the same UXVX sequence of planes with U and V rotated $\pm 60°$, relative to the X plane, aligned with vertical coordinate.

Unlike the MINERνA detector, the test beam detector has removable absorber planes, that allows to take exposures in two configurations. One has 20 planes with 1.99 mm thick lead absorber in Ecal, followed by 20 planes with 26.0 mm thick Iron absorber at Hcal. The other has 20 planes with no absorber (Tracker) followed by 20 planes of Ecal [40].

The absorber is interleaved by placing one absorber upstream of each scin-

tillator plane. More information about the Test Beam Experiment, array, calibration and analysis, in Reference [40].

2.5 Data Acquisition System

As in other experiments, MINERνA has its own specific readout electronics. The MINERνA Detector uses plastic scintillator as fundamental detector technology. The light generated by the charged particles crossing through the scintillator material is colected and delivered by a wavelength shift fiber to PMT′s.

Each PMT has 64-anode photomultiplier channels, this transforms the collected scintillator light into photo-electrons on their photo-cathodes, which are then amplified into a measurable signal by series of dynodes inside the PMT. The MINERνA Detector has approximately 500 PMT′s, which give service to $\sim$32 000 chnannels.

Each PMT is read out by a Front End Board (FEB) that has mounting six Application-Specific Integrated Circuit (ASIC) chips (TriP-t chips) that digitize and store charge using pipeline ADCs. Input charges from the PMT anodes are divided into high, medium, and low gain channels using a capacitive divider to increase the dynamic range. The high gain is 1.25 fC/ADC, the medium is 4 fC/ADC, and the low is 15.6 fC/ADC. The FEBs generate the high voltage for most of the PMTs using an onboard Cockroft Walton (CW) generator [48].

Each TriP-t chip services 32 channels and has an user-selectable gain. Two chips are set to low gain for all 32 channels; the other four chips are set to medium- and high-gain for 16 channels each. The control circuitry resides on the FEB, while the CW chain itself resides on the base, with appropriate taps for each dynode.

All FEB operations are controlled by a Spartan 3E Field-Programmable Gate Array (FPGA) chip. The FPGAs decode timing signals received over the unshielded twisted pair (UTP) cables, sequence the TriP-t chips and decode and respond appropriately to communication frames received over the data link. The FPGA also controls the CW and other aspects of FEB operation.

For data collection, the boards are daisy-chained together (into chains) using standard UTP ethernet networking cables with a custom protocol and Low Voltage Differential Signaling (LVDS). Of the four pairs in the cable, one is dedicated to timing, including clock and encoded signals, one is dedicated for data,

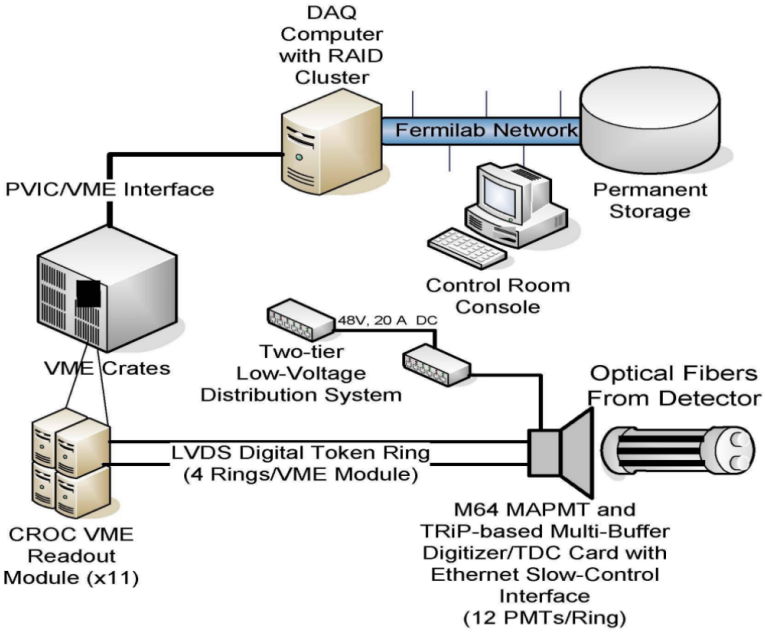

Figure 2.31: An Scheme of the MINERνA DAQ [41].

one is used to indicate the sync-lock status of the data Serializer/Deserializer (SERDES) and one for a test pulse.

An integration gate on the FEBs is opened synchronously with the delivery of neutrino beam spills. Beam spills delivered by the Main Injector (MI) are approximately 10 μs long, and are delivered every 2.2 or 2.06 s, depending on the MI operating mode. The MINERνA read-out gate opens 500 ns before the arrival of the spill and remains open 5.5 μs after the end.

During normal data-taking, one additional calibration gate is recorded between neutrino spills, either a random sampling of the detector noise (a pedestal gate) or in coincidence with LEDs flashing the PMTs (a light-injection gate). Pedestals are used to establish baseline readout levels and light-injection to monitor gain drifts in the PMTs by sudying the photo-statistics of the LED signals.

At the end of the gate, the readout system runs a software loop over all of the FEBs and collects data in the form of device frames (well-defined and formatted byte data with attached headers) one at a time for the state of the high voltage, hit timing, and finally the hit blocks themselves.

Each frame is passed through a chain to a CROC FE channel where it is

stored briefly before being passed to a readout computer for archival and monitoring processes.

Readout of the electronics is done in pairs of nested loops. Requests for data are sent to the first FEB on each FE channel before looping back to retrieve the data from the CROC memory. Then the next set of FEBs are handled in another dual loop over FE channels, etc. This allows the DAQ computers to communicate with the next CROC while the previous one is fetching data from the FEBs on one of its readout chains.

In normal data-taking MINERνA reads out in a "zero suppression" mode. In this mode, the DAQ first reads the discriminator frame data for each board and stores frames that contain hits above the discriminator threshold (about 70 fC). It then loops over those boards and reads the FPGA registers and all time-stamped ADC hit block frames. The FEBs are configured to enable readout of up to eight ADC blocks: seven time-stamped hits and one un-timed hit at the end of the integration gate.

The untimed hit carries no discriminator timing information and contains all the integrated charge between the last timed hit and the end of the gate. The FPGA registers contain configuration data, high voltage read-back, and the local gate time stamp, the time the gate was opened for integration in the local FEB counter time coordinates. Boards without hits above threshold are not read out in this loop and neither are un-time-stamped ADC frames (charge collected below threshold and stored until the end of the integration gate). All seven available time stamped hits are read out.

During construction and early low energy configuration running, a configuration with five time stamped hits and one un-timed end-of-gate hit was used. With a 2.2 s MI cycle and 35×10^{13} protons on target (POT) per spill, roughly 1 MB per spill for the entire detector in zero-suppression mode running in the NuMI Low Energy configuration is collected, about half of those data are beam spill data and half are calibration data.

Readout time for a single frame is approximately 500 μs. Most of that time is in message preparation and in setting up a block transfer; for our data the readout speeds per frame are largely insensitive to the size of the frame. Physics gate readouts typically require 1200 frames on average, while calibration gate readouts require 1600 (channel occupancy is lower in physics gates). Therefore, reading a typical cycle (single physics gate plus single calibration gate) requires 1.4 s.

Calibration readout times are very stable, but physics gate readout times vary with the level of activity in the detector. The DAQ is programmed to protect the integrity of physics gates above all else. It will only attempt a calibration readout in the case where the physics readout is accomplished in under 0.9 s. If the subsequent calibration readout extends beyond 0.9 s, the DAQ will dump that readout and simply arm for the next physics spill. However, the DAQ will not interrupt readout of a physics gate. Propagation of the start gate signal is blocked in hardware and only unlatched after readout is complete [41].

Chapter 3

Simulation

3.1 Beamline and Flux

The NuMI beamline prediction is possible with G4NuMI, that is a GEANT4 adapted version. The G4NuMI allows modification, as complete interaction record for all produced hadrons and adapted physical models.

On beamline prediction are included a complete description of all the components mentioned on the previous chapters, as the geometry and materials in the baffle, target, horns, target hall, decay pipe, hadron absorber, muon monitors, and unexcavated rock in areas relevant for the beamline. In G4NuMI, the target position and horn current are configurable.

The products of primary $p + C$ collisions are allowed to propagate through the material of the NuMI beamline, where they may reinteract. The products of these interactions are focused according to a description of the magnetic horns and decayed by G4NuMI. This procedure is used to predict the flux spectrum from NuMI for all neutrino and antineutrino flavors [36].

The Monte Carlo flux prediction is frequently changed as new constraints from measurements of hadron production in conditions similar to the NuMI beamline are added.

To improve the knowledge of hadron production in neutrino beams, measurements of hadron production on external targets are used to tune the simulation.

MIPP and NA49/SHINE are two of such external hadron production experiments that were performed for this purpose. T2K and MINOS use external data from these experiments to tune hadron production in their beamline simulation. MINERνA also utilizes NA49 data to tune NuMI beamline simulation.

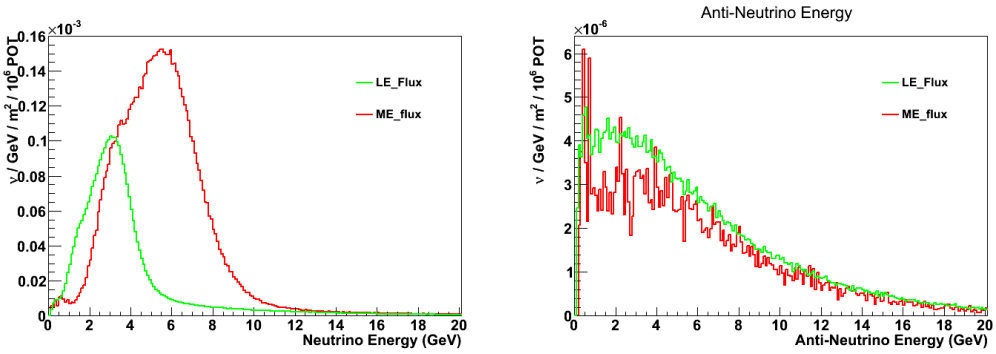

Figure 3.1: Neutrino flux prediction at MINERνA. $\sim$93% of the of the flux are composed by muon-neutrinos, $\sim$ 6% by antimuon-neutrinos and $\sim$ 1% for electron-neutrinos. Left: muon-neutrino flux. Right: antimuon- neutrino flux. On both cases, the green line describes the Low Energy prediction and red one is the prediction for Medium Energy.

In principle, each time that the flux is changed, the neutrino interaction simulation, detector simulation and reconstruction of this simulated data must be completely redone, beacuse different flux give different interactions. On the Figure 3.1 are shown the 4 types of neutrino fluxes usend on different MINERνA periods.

To avoid this repeated nearly duplicate MC productions, a reweighting technique is used for variations in the flux. Each event in the Monte Carlo simulation gets a reweighting factor from the ratio of new flux to old flux as a function of neutrino energy [44].

3.2 Event Generator

After having the simulation of the NuMI beamline, and the flux prediction, the next step to do is the event generation. It predicted using GENIE, that is an object-oriented neutrino generator, it is used on several experiments: T2K, NOνA, ArgoNeuT, MicroBooNE and MINERνA.

GENIE use the flux information from the external G4NuMI beamline simulation output files.

The GENIE flux driver uses an spatial window to predict neutrino flux at a

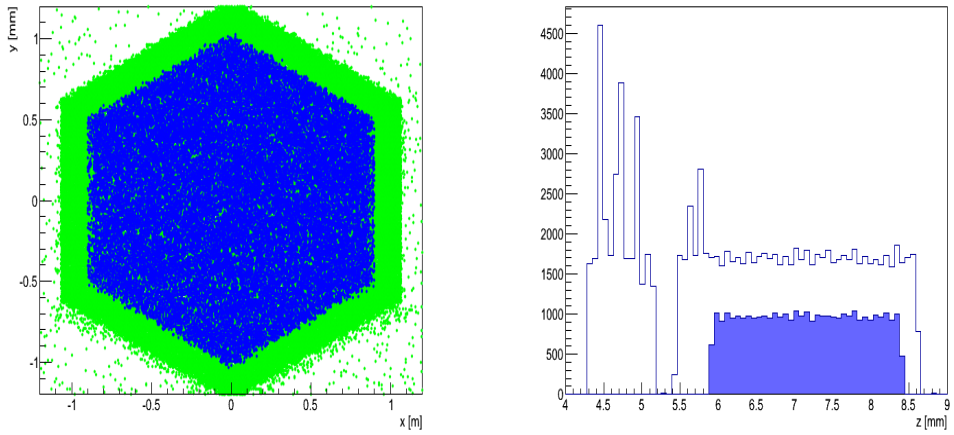

Figure 3.2: Genie sample. Left: Transversal view of the detector, interactions on plane 25, the blue color represents interactions on tracker region, green the interactions on SideEcal. Righ: Longitudinal-transversal view of the detector, the blue color represents the interactions just in the tracker region.

specific location. The flux window is located upstream of the MINERνA Detector, and its position is given in terms of beamline coordinates [44]. The window size are optimized to prevent unnecessary inefficient generation.

GENIE uses a simplified geometry description of the detector (see Figure 3.2), due to that the neutrino interaction is approximately proportional to the volumen and density of the components in the MINERνA Detector.

A cross section spline file is used for efficient generation. The cross section spline file is pre-generated for each interaction type, each neutrino flavor and each different isotope in the target. As the neutrino flux flows through geometry material, geometry analyzer calculates path lengths through volumes separated by each isotope [44].

Then, the neutrino interaction is predicted using density and individual cross section. After it has been determined that the neutrino interacts, GENIE selects the interaction process randomly by considering the relative likelihood for each process $P_p(E_\nu) = \sigma p(E_\nu)/\sigma(E_\nu)$. Finally, event kinematics are determined according to the model of the particular interaction process [36].

The generation of the different neutrino interaction process on GENIE, is handed by several Physics Models. Here, we are only enumerating the process and used physics models [36].

These are some of those models:

- Quasi-Elastic Scattering: Llewellyn-Smith.
- Resonance Production: Rein-Seghal.
- Deep Inelastic Scattering: Quark Parton and Bodek-Yang.
- Transition, Resonance to DIS: Applying cuts on W. Res: W $<$ 1.7 GeV, DIS: W $>$ M_{Δ}^{++} 1.232 GeV $<$ 1.7 GeV.
- Hadronization: AGKY and KNO.

As was described on the first chapter, neutrino electron scattering is based on a tree-level calculation, where the low energy term, m_e/E_ν is ignored, which is small correction for the GeV neutrino energies.

A portion of the predicted background comes from a similar reaction: the inverse muon decay ($\nu_\mu e \to \mu^- \nu_e$), includes 1-loop radiative correction.

Due to that it is considered events with only one forward electron, the major background to the neutrino electron scattering is any process which gives a single electromagnetic particle in the final state. For example electron- neutrino charged-current quasielastic (NuE-CCQE) reactions, $\nu_e n \to ep$.

If a recoil proton or neutron is not observed in the detector, which is common at low Q^2 , NuE-CCQE events looks like a single electromagnetic shower.

Most parameters of the Llewellyn-Smith model, are precisely determined in electron scattering, and we used the BBBA2005 form factor parametrization of these form factors. However, the nucleon Axial Form Factor, F_A, while precisely known near $Q^2 = 0$, does not have its variation with Q^2 well measured in electron scatering [44].

On GENIE the Q^2 dependence of axial vector form factor has dipole form,

$$F_A = \frac{1}{(1 + Q^2/m_A^2)^2} \tag{3.1}$$

here m_A is axial mass. Under this dipole assumption, other measurements of neutrino CCQE favor a value of $m_A = 0.99$ GeV [44].

Other background contribution to neutrino electron scatering are the process that involves π^0 production, because it interacts via electromagnetic, and decays into 2 gammas. For example, $\nu A \rightarrow \nu\pi^0 + RecoilNucleus$.

The dominant reactions that produce this final state are the excitation of baryon resonances which decay to nucleons plus pions, and the production of pions from coherent interactions with the nucleus.

The coherent pion production mechanism has a smaller cross section, but it produces energetic forward π^0. These reaction are built from an approximation where the target is a single neutron or proton inside the nuclei. The kinematic modification of this target nucleon is simulated by a relativistic Fermi gas (RFG) model for exclusive processes [44].

Many different types of interactions are considered, whose rates in the simulation are based on measurements of hadron-nucleon scattering as follows: elastic scattering, pion or nucleon charge exchange, inelastic production of pions and absorption of pions.

Other feature of GENIE is that it includes the event reweighting, such feature is useful for studying uncertainties due to variations in cross section models.

3.3 Detector Simulation

The simulation of the MINERνA Detector is based on GEANT4, it is an internal part of the GAUDI Framework, where the analysis and simulation are implemented.

Each event generated on GENIE, has no time stamp, this means that each event is distributed randomly according to the Main Injector bunch time structure, and later handed by GEANT4.

The physics models used on GEANT4 for Detector simulation are configurable. For electromagnetic interactions the default GEANT model is used, and for Hadronic interactions is used the QGSP BERT model.

To do the detector simulation, it is necesary to define the detector geometry, it consists of shape and material definitions, placing daughter volumes inside mother volumes, and placement of replicas when the geometry is repetitive.

Only a few definitions of shapes are necessary, because most of the MINERνA detector is made from the same module shape and composition.

All the aspects related to real detector have been included on the simulation, for example the fiber hole and the rounded corner of triangular scintillator strip have been implemented, see Figure 3.3. And the three kinds of module for Tracker, Ecal, and Hcal have slightly different absorber configurations.

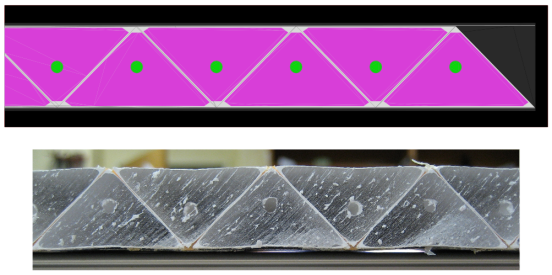

Figure 3.3: Top: Simulated plane, composed by simulated scintillator strips. Bottom: Cross section of an actual scintillator plane [44].

Due to the flexibility of the XML structure, that allows a slightly different detector configuration to be studied without signifiant duplication of geometry coding, the MINERνA geometry is defined based on XML. A component in an XML file can access to another component from a different XML file via a reference link.

3.4 Readout Simulation

The simulation works by propagating particles in time steps, determining if and how they interact with the material. So the next step on the simulation, after got the GENIE sample, is to simulate the energy deposition.

The GEANT4 simulation result is a collection of true energy deposition with coordinates where the energy loss happened in the detector. The particle detector consists of active components and inactive components, like Ecal and Hcal absorbers. GEANT4 only simulates the particle interactions with material, i.e. when particles travel through the detector volume.

MC hits from all scintillator strips are serialized into a list without association to originating volume. Geometric calculation is performed to find the

originating strip from (x, y, z) coordindates of the MC hits.

Energy deposition in the strip is converted into light in the scintillator, proportional to the deposited energy. An optical model translates the energy deposited in scintillator into light using Birks law. The calibrations are applied so that the photostatistics and light yield in the simulation match those found in data.

Light propagation through a WLS fiber is simulated using a measured attenuation curve that was measured from Module Mapper. In order to find the correct electronics channel that is connected to the strip, a detector strip to electronics channel map is used. This map combines the complicating mapping of clear fiber cables to PMTs and the PMT pixel weave [44].

Time-dependent calibrations applicable to the overlaid data event are used to calibrate the energy and include the identification of dead channels. A PMT model that includes optical cross-talk converts the light into charge. The time it takes for light to propagate through optical fibers is smeared with a data-driven model. Digitization of charge into hits is simulated by a model of the front end electronics.

The PMT simulation includes the measured optical crosstalk probability that the photon lands on a part of the photocathode which feeds a neighboring PMT dynode. Signal smearing during the dynodes amplification is also simulated, and the response of the electronics is also simulated to produce the equivalent "raw" detector data for the simulation.

This "raw" simulated detector data can then be run through all the same calibration and data processing steps as the real data. A complete description of the calibration process can be found on the Reference [44].

The Figure 3.4 summarizes the simulation process on the MINERνA Experiment.

3.5 Overlay with Data

Many aspects of the Monte Carlo data are not simulated. Some of them include the event overlap in the detector, events in the calorimetry, rock muon events, dead time, dead channels, and miscalibrations.

Instead of developing complicated extensions to the simulation, the effects

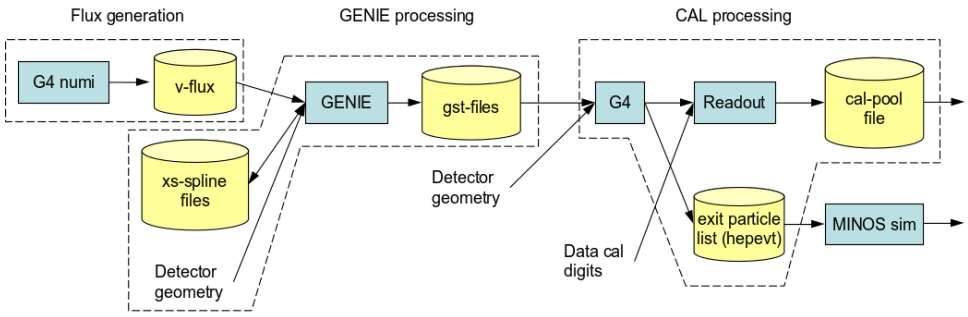

Figure 3.4: Summary of the stages to generate the Monte Carlo data.

are directly imported from real data. The MC data overlay procedure is preferable as it is clearly more representative of the real data than any simulation of these effects could be.

Some times, a neutrino interaction in the detector or some rock muons may produce deadtime or cause hit overflow, this may generate that the following neutrino interaction of interest may not have all hits recorded in the detector.

For example if the region of dead time is near to the interaction vertex, the event reconstruction cannot be reconstructed with correct vertex, then these events will not be used for analysis, this means that some candidate signal events are wasted, i.e. the detector has not an optimal efficiency.

If the neutrino interaction in the real data overlaps with the previous neutrino interaction or rock muon without dead time, the event reconstruction may be blind by the overlapping. Such effect can be simulated from single interaction MC.

A realistic hit time model is difficult to do due to lack of an accurate model for detector components and electronics. To get around these difficulties, single interaction MC event is overlaid with actual data from a randomly chosen beam spill. The data-MC overlay allows get a more realistic deadtime and hit overflow from multiple interactions and event overlapping in the MC sample.

Since we are only interested in data hits that are near the MC interaction time, only data hits within 50 ns of the hits from the MC simulated event are considered. The reason to use the latest MC hit time in this calculation is that the interaction may have delayed activity like a Michel electron [44].

MC-Overaly sample is prepared/generated for an specific run period, using

data from that corresponding run period for the overlay, the idea is to take into account time variation and hardware updates for the corresponding running conditions.

Chapter 4

Reconstruction

Due to that this study is the first one in MINERνA Medium Energy region, and it is an extension of the previous one in Low Energy, we are using "basicaly" the same reconstruction package developed from Low Energy, so this chapter is a complement of the main Reference [42].

4.1 Data and Monte Carlo POT Samples

This thesis was done using the data from the first year of the Neutrino Forward Horn Current Medium Energy (ME) Beam configuration run, just the first of the 2 years data were used, these have been taken from September 2013 to September 2014 using the Forward Horn Current (FHC) or commonly know as neutrino mode.

At the moment we only have the Monte Carlo (MC) sample just for the first playlists, it has been done simulating the corresponding status of the MINERνA Detector, on this case, the MC General Sample corresponds to the status of the MINERνA Detector between September - December 2013.

Due to the lack of simulated events and to get a better modeling, some Neutrino Electron Elastic high statistics samples were generated and processed for each one of the Medium Energy playlists used on this thesis. Table 4.1 shows the POT size for Data, General MC and NuEElastics high statistics samples.

To qualify as useful data for analysis, the data must meet certain quality requirements. The primary proton beam position and various other primary beam and secondary beam conditions, such as the focusing current in the horns, have been monitored during neutrino beam operation. The analysis requires that the neutrino beam is an expected state, the POT counting and the beam flux

Playlist	Data	MC	NuEElastic
me1A	9.118	80.482	3000
me1B	1.864	N/A	630
me1C	4.720	N/A	1560
me1D	14.367	N/A	4730

Tabla 4.1: Protons on Target (POT) for Medium Energy Data, MC and NuEElastic hight statistics samples used on this thesis. All the samples are scaled to $\times 10^{19} POT$. The data sample is comparable to the Low Energy sample data used on the Reference 42.

prediction based on that counting are reliable.

The status of the MINERνA DAQ is also required to be good; otherwise data from the detector may not be reliable. Good status of the MINOS Near Detector is generally necessary for analysis of the ν_μ Charged Current reactions, those dominate the observed reactions in the MINERνA Experiment, these muons leave the MINERνA Detector at the back part and are necesary to be reconstructed.

The Neutrino Electron Scattering does not require muon reconstruction, so the MINOS near detector has not been taken into account.

The analysis is done with a Data-overlay in MC samples, it is used to mimic the overlap of multiple interactions and deadtime of electronics.

Some MC events will become unanalyzable due to the event overlap or deadtime as a result of event overlap, and the simulation successfully reproduces such occurrences. However it is possible to reconstruct Neutrino Electron Scattering events from overlaid data as a MC event, if the true MC interaction is some other reaction that happens outside the fiducial volume.

Due to that the MC analysis relies on the simulation itself generating the candidate event, this is not a genuine MC event for the purposes of this analysis.

For a given reconstructed event in MC sample, it can be either a genuine MC event or an overlaid data event or even possibly a mixture of both. Because it is a MC simulation and there is full knowledge of the event, it is possible to determine what fraction of energy in a reconstructed event is from MC hits, to handle this feature, is used a plausibility cut, that will be described later.

4.2 Reconstruction

An energetic electron traverses about a radiation length as a MIP (Minimal Ionizing Particle) until it begins to shower. The radiation length X_0, in the Tracker Region is about 42 cm, when the direction of the electron is normal to the planes, the radiaton length corresponds to 25 scintillator planes.

The first part of the electron interaction with the detector, before it showers, could be a track-like, this part of an electron shower can often be reconstructed as a track. In this analysis the track serves as the heart to applay a cone that encloses the shower seeding as shown in the Figure 4.1.

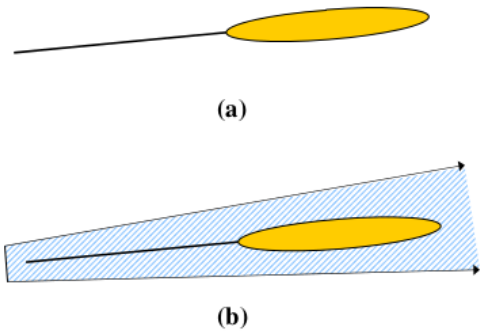

Figure 4.1: (a) Electromagnetic shower with the beginning of shower reconstructed as a track. (b) Shower cone enclosing the track-like shower [44].

In order to apply the shower cone algorithm, the start position and direction of the electromagnetic shower should be known. The shower cone angle is chosen to collect most of the hits that are associated with the shower. Even though the seeding track is 3-dimensional, the shower cone is applied in 2D, i.e. in XU, and XV views. If more than one track is available at the same time gate, then the more upstream track will be used first as a shower cone seed.

Occasionally an electron starts to shower early and the MIP track is too short to be reconstructed as a track. In such case, an isolated blob will be used for the shower cone seeding. The most upstream isolated blob is used as shower cone seeding as shown in Figure 4.2.

On such case the direction is determined from a fit to the shower cone seeding isolated blob. If the most upstream isolated blob is too short, and the direction of the isolated blob seed does not give a reasonable direction for the shower cone, the next upstream isolated blob will be used as a shower cone. This procedure continues until the shower cone algorithm succeeds in creating

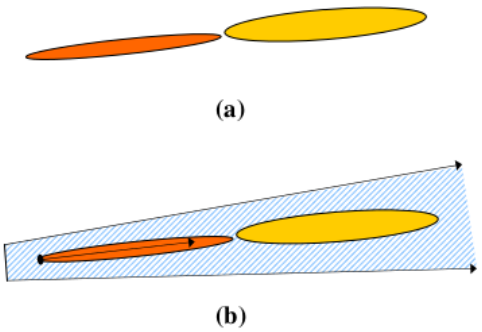

Figure 4.2: (a) Electromagnetic shower with beginning of shower reconstructed as an isolated blob. (b) Isolated blob seeded shower cone [42].

a shower or there are no more available isolated blobs.

In the case where the most upstream small isolated blob is skipped for the seeding, the shower axis of the reconstructed shower cone is traced back in the upstream direction to check if the small isolated blob is on the shower axis. If the small blob is on the axis, the shower start position is moved back to the small blob, and shower direction is determined from the small blob and the reconstructed shower cone.

The cone shape parameters that are used are the cone offset (50 mm), the cone opening width (80 mm) and the cone opening angle (10 degrees), they are showed in the Figure 4.3.

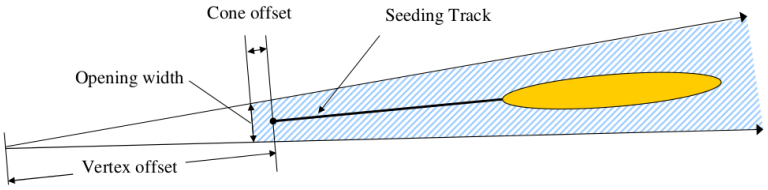

Figure 4.3: Shower cone and shape parameters [42].

4.2.1 Calorimetric Energy

Using the shower cone shape, the energy contained into it is measured calorimetrically. The calorimetric energy is the sum of calorimetric energies in each sub-detector computed with each apropiate sub-detector's calorimetric constant as is decribed by the Equation 4.1.

$$E = \alpha(E_{Trk} + k_{ECal}E_{ECal} + k_{HCal}E_{HCal}). \quad (4.1)$$

Where E_{Trk}, E_{ECal} and E_{HCal} are the visible energies in the Traker, Electromagnetic Calorimeter and Hadronic Calorimeter, respectively. The parameter α is at the same time an scale factor and the Tracker Calorimetric constant. The k_{ECal} and k_{HCal} are the Electromagnetic and Hadronic Calorimetric Constants respectively.

The physical interpretation for the k_{ECal} and h_{HCal} is the quantity necesary to compensate the energy loss in the pasive absorber material at the ECal and HCal region respectively. The scale factor α compensates the energy loss in the inactive materials in each scintillator plane, such as the WLS fiber, capstocking material, lexan wrapping and epoxies.

The clusters with low activity, that often are the after-pulse noise or cross-talk hits, have not been included in the calorimetric energy calculation.

The calorimetric constants were determined via MC studies. The tracker constant α was determined from events generated using an electron particle gun sample(MC-PC) with a semi-infinite size, and just working inside the Tracker Region. The Figure 4.4 show the Visible Energy vs the True Energy before applying the proportional scale factor α.

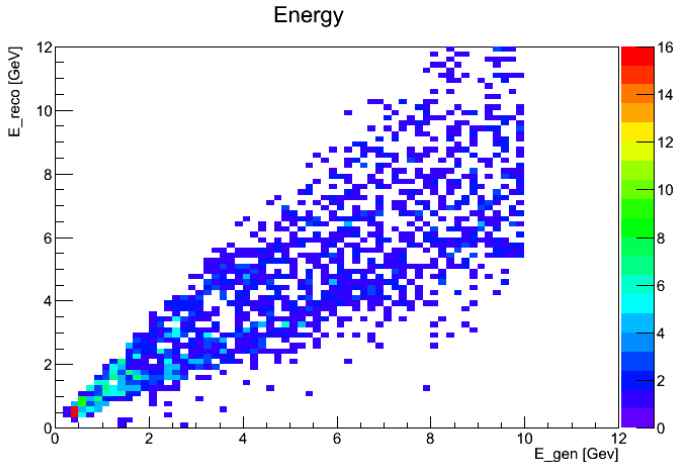

Figure 4.4: True electron energy vs Reconstructed electron energy, before applying the α calibration constant.

As is shown in the Figure 4.5, the scale factor was calculated from the ratio between True(GENIE) Energy and Visible Energy ($\alpha = E_{True}/E_{Vis}$). To do this, it is necesary to apply some cuts like fiducial volume, plausibility and good reconstructed tracker, to restrict the working volume region at the Traker

Region and use only the useful events.

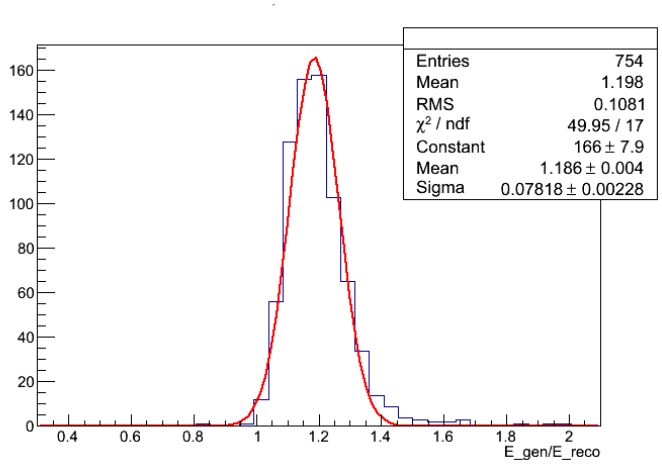

Figure 4.5: The Tracker constant "α" is calculated from a gaussian fit applied over the Reconstructed and True energy ratio distribution.

The α constant is obtained from the mean of the Gaussian fit. After calculating the constants, this is applied over the Visible Energy as an scale factor, now the Visible Energy vs True Energy are showed on the Figure 4.6.

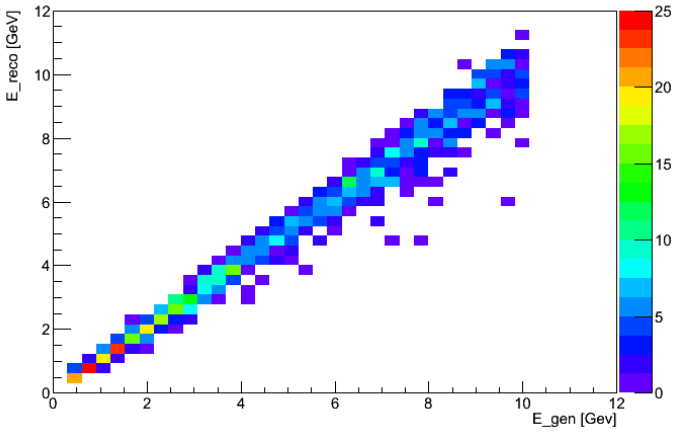

Figure 4.6: Reconstructed vs True energy after applying the calorimetric tracker constant.

Then following the same process, using the electron particle gun (MC-PC) sample, but now with on the semi-infinite ECal Region, the ECal calorimetric constant was calculated from $k_{ECal} = E/(\alpha E_{ECal})$, where α comes from the

Constant	Value
α	1.296
k_{ECal}	2.341
k_{HCal}	9.54

Tabla 4.2: Calorimetric Reconstructed Energy values in Medium Energy.

procedure mentioned above.

The MC-PC with a semi-infinite HCal-only geometry is used in a similar fashion to calculate the HCal calorimetric constant ($k_{HCal} = E/(\alpha E_{HCal})$).

To get the calorimetric constants, the low energy events ($E < 0.5$ GeV) have not been used, due to that those are nonlinear at low energies. The calorimetric constants obtained with electron particle gun samples (MC-PC) are sumarized in the Table 4.2. The calorimetric energy constant for the Tracker Region in Medium Energy is 3.9% more lower than the same parameter ($\alpha_{LE} = 1.348$) used on the Low Energy region.

The Side ECal has not been taked in the Equation 4.1 because it will be treat on different way, depending on the hit position, see Figure 4.7.

If a hit is known to be in the Side ECal region as shown in Figure 4.7 (a), it can be treated in the same way as the downstream ECal.

For the x-y position is little more hard, for example when the electromagnetic shower are close or in the Side ECal. Thus, the Side ECal calorimetric energy calculation only relies on hit strip position. If the hit is from strip 1-10 or 118-127, it is certainly a Side-Ecal hit.

The C hit in the X-plane in the Figure 4.7 (b) will be recognized as a Side Ecal hit, but the same position will not be recognized as a Side ECal hit in the following U or V-planes as in (c) and (d).

Since plane orientation follows XUXV pattern, hit C will be treated as a Side-Ecal hit twice in four planes as shown in Table 4.3.

Hit B in the V-plane in (d) will be recognized as a Side ECal hit but not in the X or U-planes. Hit B will be treated as a Side ECal hit only once in four planes as shown in Table 4.3. Hit D in the U-plane will be treated similarly as hit B in the V-plane [42].

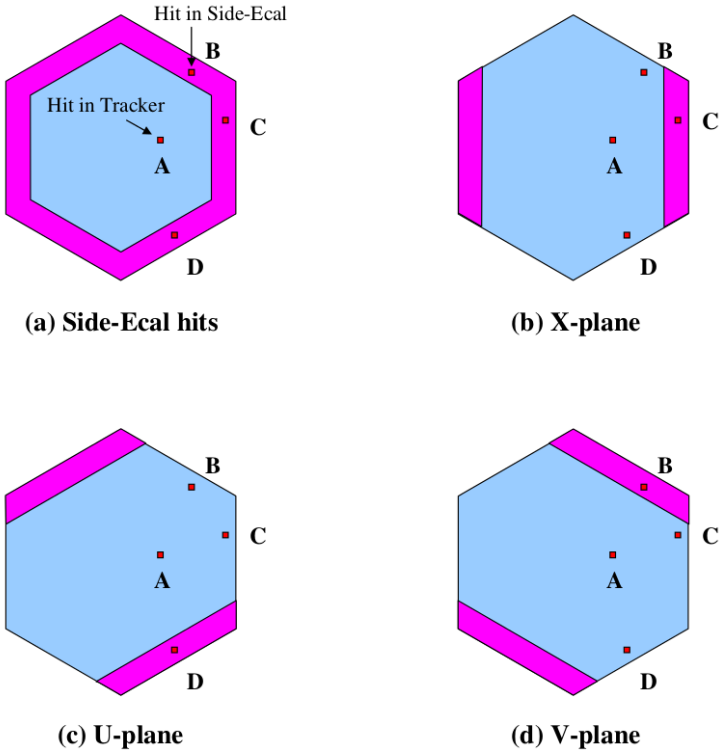

Figure 4.7: Different possible positions of the hits on Side ECal [44].

If a hit is from strip 1-10 or 118-127 in the X-view, it is necessary to compensate the missing Side-Ecal energy in the U and V planes. The energy calculation without a correction is $\pm(k_{ECal}e_1+e_2+k_{ECal}e_3+k_{ECal}e_4)$, where the energy deposited in the 4 planes are e_1, e_2, e_3, and e_4, respectively. The energy deposited in each of the 4 planes are approximately the same, therefore

$$\alpha(k_E e_1 + e_2 + k_E e_3 + k_E e_4) \approx 2(k_E + 1)e. \tag{4.2}$$

Plane	B	C	D
X-view		✓	
U-view			✓
X-view		✓	
V-view	✓		

Tabla 4.3: Checkmark squares represent the hits recoignazed as Side ECal hit based on the strip position in the plane [42]. The hit positions B, C and D are defined in the Figure 4.7.

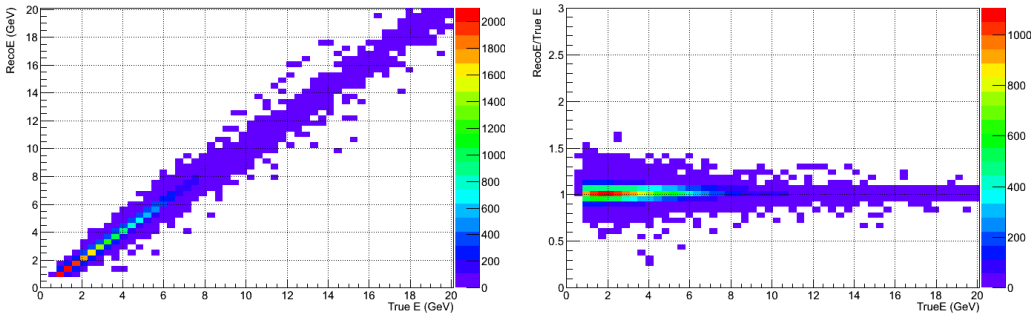

Figure 4.8: Left: Reconstructed vs True energy. Right: Electron energy resolution.

Ideally, the correct form is $4k_E e$. Then, the missing amount is

$$4k_E e - 2(k_E + 1) = 2(k_E - 1)e. \tag{4.3}$$

Similarly, a compensation factor for the U or V-plane is $2(k_E 1)e$. In summary, the calorimetric energy calculation with Side ECal is given by

$$E = \alpha[(E_T + k_E E_E + (2k_E - 1)E_{SE}^{X-view} + (4k_E - 1)E_{SE}^{U,V-view} + k_H E_H], \tag{4.4}$$

where E_{SE}^{X-view} is the Visible Energy in the Side ECal for X-view plane, and $E_{SE}^{U,V-view}$ is the Visible Energy in the Side ECal for U or V-view plane, respectively.

After obtaining the calorimetric constants, using a High Statistics NuEElastics sample, it is posible to check the Reconstructed Energy versus the True Energy as shown in the Figure 4.8.

On this case, only some minimal cuts were applied just to check the good recontruction of the events. The event selection will be described in the next section. From Figure 4.8, the energy scale is flat over the entire energy range.

The energy dependence of the energy resolution will not follow conventional calorimetric behavior exactly, because the vertex Z position varies within the fiducial volume (will be explained in the next section), and the fraction of the energy in the ECal affects the energy resolution.

The low energy point is not on the fit line because the shower does not reach the Ecal. The energy resolution of a shower fully contained in Tracker will be

better than one reconstructed in the mixed calorimetry of Tracker and ECal [44].

4.2.2 Direction and Angular Resolution

The experimental signature of the $\nu e \rightarrow \nu e$ is single electron at very forward angle, so the accurate in the direction recontruction is critical to the background rejection when kinematic constrain (Equation 1.99 or C.31) is applied.

To get the direction, is not necessary to use all the nodes and energy centroids on the scintillator planes, because the part of the shower is wider in transverse size, and the transverse energy distribution could be asymmetric due to shower fluctuations. To determine the optimal direction of the electron only is used the beginning of the electron shower, just were the shower is a narrow track-like, see Figure 4.9.

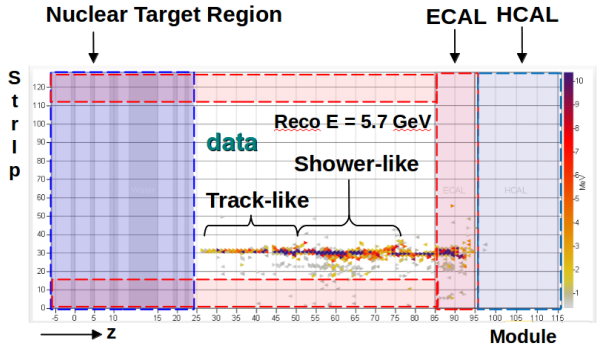

Figure 4.9: Real reconstructed EM Shower as it seems in the event display software tool.

The energy centroid diverts significantly from the shower axis near the end of the shower, where the shower diminishes gradually. Also, occasional heavy bremsstrahlung can give off shower axis energy deposits near shower maximum position.

The electromagnetic shower is not a single particle once the electron starts to shower, and then to use The Kalman fitter tool to get track direction, that is single particle fitting, the direction is is obtained using up to the first 30 fit nodes, i.e. before the electron begins to shower.

However, the charged showering particles travel collinearly because the detector is not magnetized. So, the showering particles are treated as a single

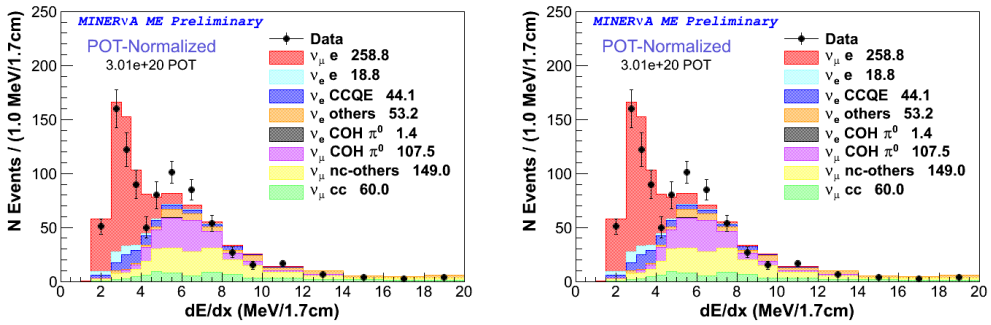

Figure 4.10: Angle resolution for electrons. Left: x axis. Right: y-axis. The angle resolution on x direction is slightly better than the y direction, due to the MINERνA Detector planes configuration.

particle collectively using the energy centroid positions.

The Kalman filter was used with the single electron assumption. In other words, the particle mass parameter in Kalman filter was set to the electron mass. The fit of the Kalman filter will be best at the beginning of shower, and this is used to represent the initial electron direction.

The Figure 4.10 shows the angular resolution just for a high statistic NuEElastics sample. The angle reslution is represented by the angle residual in each x and y directions. The angle x is solely determined by the X-planes, while the y direction is determined by combining the U and V-planes. The y angular resolution is slightly worse than the x angular resolution due to the X, U, and V plane orientation and XUXV plane configuration [44].

The angular residual vs electron energy is shown in the Figure 4.11, we can see more NuEElastics events at low energies, and the angular resolution is better at high energies, due to that the electrons at higher energy can travel more distance before the shower development.

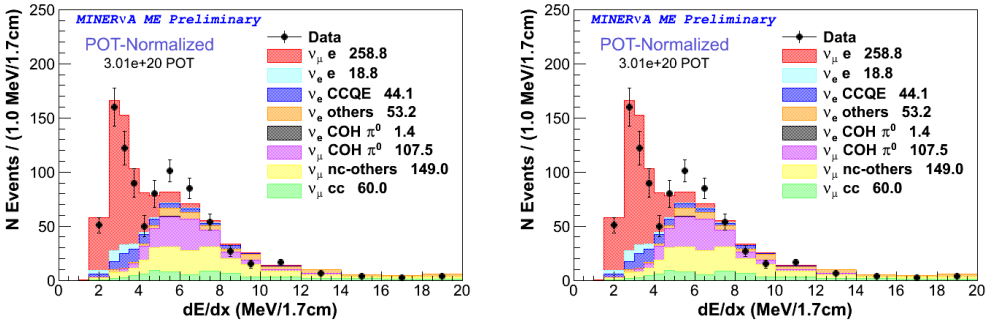

Figure 4.11: Angle vs Reconstructed Energy: Left: angle in x direction. Right: angle in y direction. The angle resolution is better at high energies.

Chapter 5

Event Selection

Each one of the cuts applied on the neutrino electron scatering study in Medium Energy were tested, the goal was optimize the signal selection, but due to this analysis topic represents the first study on Medium Energy beam configuration, a lot of problems was found on the way.

In the Medium Energy some cuts used previously in Low Energy analysis are applied and 2 new cuts have been added; 1 cut from Low Energy was eliminated.

The Neutrino Electron Scattering is a rare event, to find these events represents a lot of effort to build an efficient event selection system in order to maintain high efficiency for single electron signal events, and be very carefull to not reject the few signal events.

The shower cone that is the base of the event reconstruction, is applied wherever a viable seed is found as described in the previous chapter. Due to this feature, the raw output of the reconstructed showers does not necessarily represent a good reconstruction, particularly for background events and events originating outside the tracker region of the detector.

Requirements on the location vertex of the shower cone and quality of the reconstruction are necessary to ensure that the reconstructed shower cones are consistent with electrons originating from the Tracker Region.

The cuts used on event selection can be divided on tree types: Fundamental Cuts -Basic event selection- Pre-Selection Cuts -Quality recontruction- and Signal Selection Cuts -Neutrino Electron Scattering signal isolation-.

The first two types of cuts, preserve a very high single efficiency ($\sim 99\%$). For the third cut type, the most strongs cuts are applied, to reject the photons

that looks like a single electron, and to reject electrons at large angle. Both cuts are necesary to be consistent with Neutrino Electron Scattering definition.

5.1 Fundamental Cuts

The fundamental cuts are the minimal requierements imposed over the MC and Data samples analysis. This includes the good quality and geometrical reconstruction and the ionization handle.

5.1.1 NullReco

This cut is used just to ensure if some track were or not reconstructed in the gate, in some cases the gate have information related to tracks reconstructed on the Reco Stage, but the Ana/NuE tool is unable to give a good reconstruction, the issue come from the unknown vertex position or rock muons.

5.1.2 Fiducial Event

The fiducial volume defines a proper region of work inside of the MINERνA Detector. The main idea of this cut is to have the best quantity and quality information using the vertex position information.

The fiducial volume is defined by a hexagon with an apothem 88.125 cm whose outer boundary is therefore 4 cm away from the inner boundary of the Side ECal. A z-view of the Inner Detector is shown in Figure 5.1.

The most upstream two modules in the Tracker Region have been excluded from the fiducial volume, the idea is to remove interactions from the Nuclear Target Region, which includes other pasive materials different of the scintillator and for this composition has different detector response for electromagnetic showers.

The most downstream four modules in the Tracker are excluded from the fiducial volume in order to have at least four module track length in Tracker, the reconstructed shower has good angular resolution before it enters into ECal.

The top-longitudinal view of the Inner Detector with highlighted fiducial volume is shown in the Figure 5.2. The total mass of the detector within the

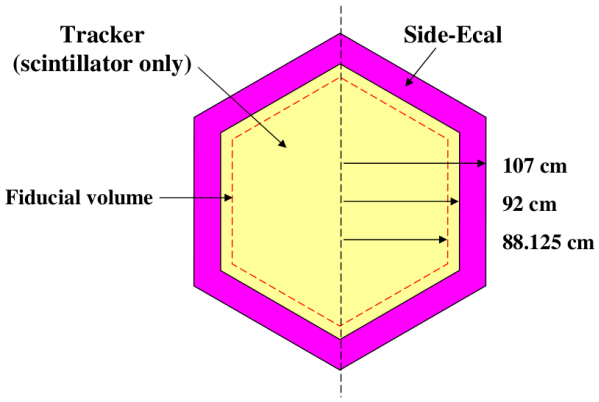

Figure 5.1: Transversal draw of the MINERνA Detector with the fiducial volume viewed from the direction of the beam [42].

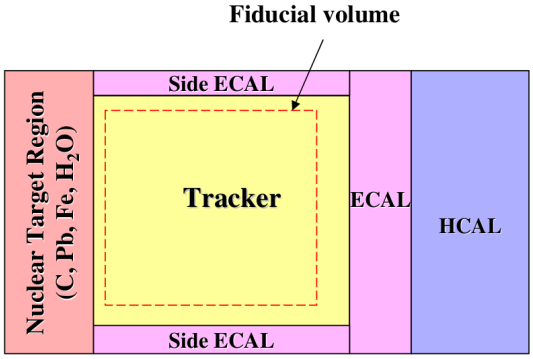

Figure 5.2: Longitudinal squeme of the Inner MINERνA Detector with the different regions. The fiducial volume corresponds to a portion of the Traker Region.

fiducial volume, which is proportional to event rate, is about 3 metric tons.

5.1.3 Plausiblility

The plausibility cut is made with "e is plausible" variable, it is a requirement that only has effect on MC Sample, because this cut uses the information of the clasification of the Prong inside the DAQ System, this means that the prongs can be identified or assigned to a determined particle, for example muons, proton or electrons, and only it is possible the identification on MC samples because the true information is known.

This cut is useful to know if the MC sample is overlaid or not, because it only has 2 options: 0 or 1. 0 for Data inside MC sample; and 1 for MC data.

When a Data sampe is analyzed, automatically the number 1 is asigned at the time when the job is sent to the Fermi-Grid.

5.1.4 Minimum Energy

Neutrino Electron Scattering at low energies has a very high background, mostly resulting are photons from π^0 decays. The event reconstruction is also more challenging for lower energy electrons.

In particular, the particle identification for low energy electrons becomes more difficult because the electron does not have enough energy for bremsstrahlung, and the subsequent photon e^-e^+ pair production processes to cause the particle multiplicity to rise as the electron traverses the detector, see Figure 5.3.

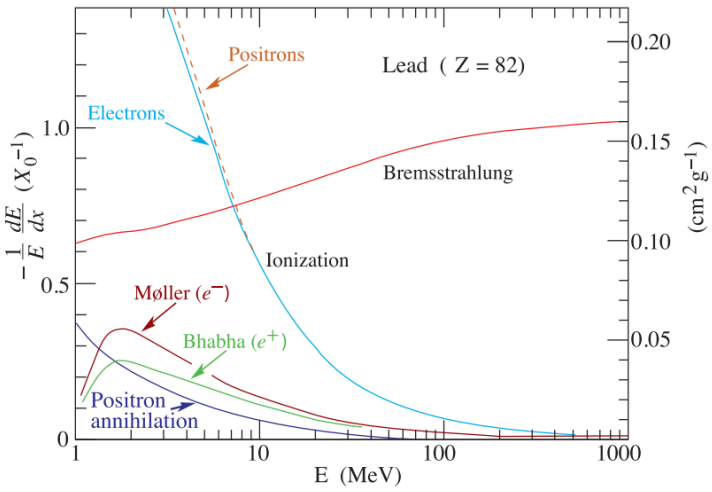

Figure 5.3: Fractional energy loss in Lead as a funtion of positron energy [7], in the Appendix B there is a better desciption.

In that case, electrons are too similar to particles which merely lose energy by ionization and leave straight tracks in the detector.

Another pathology of the low energy electrons is that they often create showers with gaps along their longitudinal development track due to hard bremsstrahlung. When a hard bremsstrahlung photon carries most of the energy from an electron, the shower becomes invisible in the detector until the bremsstrahlung photon undergoes pair production [42].

Since the gappiness in the electromagnetic shower is unique, it could serve as particle identification for low energy electron. These shower gaps are not used in this study, but they could be used to allow extension of the energy threshold to lower energies.

Due to this phenomenon, the energy of electron candidates is required to be greater than 0.8 GeV.

5.2 Pre-selection

On the Pre-selection cuts, some geometrical, energy balance and electromagnetic shower size are imposed, to ensure at the end to have the best signal isolated candidates.

5.2.1 Bending Angle

High energetic electromagnetic particles produces a shower that follows a straight line in the same direction of the initial particle, since typical transverse momentum exchanged by bremsstrahlung or pair-production reactions is of the order of electron mass.

In particular, a large fluctuation of the transverse direction in the early stages of a true electromagnetic shower is very rare, and when this does happen, it is often correlated with the gap behavior described above.

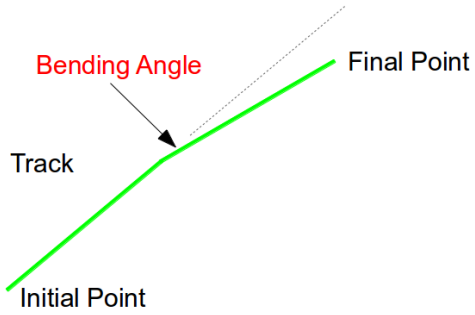

Figure 5.4: Bending angle cut representation.

By contrast, in the hadronic interactions the impact transverse momenta is of order m_π, and so often appear bent along their path. The bending angle of a shower is measured by drawing segments between the shower track-like start

point and the midpoint as shown in Figure 5.4. The angle between initial the midle point and between the midle point and the end of the shower.

The bending angle is measured in the midle piont of the electron signature.

The goal of the bending angle cut is to handle the cases with a large kinked path, on this situaction the shower cone will not contain the entire kinked track. However, this metric is almost always sufficient to identify such events.

Other goal is to reject the overlaping events in one-view. This cut need to be optimized, because it uses only the information coming from one-view (X, U or V-view), for the ideal situation the bending angle should use the information coming from at least two-views.

5.2.2 Chi2perDoF

The determination of the electromagnetic shower direction is made with the Kalman fitter assuming the beginning of the electromagnetic shower behaves like a single particle, which was described previously in the Reconstrution Section.

The Kalman fitter produces a χ^2 statistic, describing the quality of the fit to this underlying model of a single particle.

The reduced chi squared, χ^2/degree of freedom does not follow the expected χ^2 distribution because the single particle hypothesis is not correct. However, high values of this parameter are highly correlated with events where the fitted direction of the electromagnetic shower is misreconstructed due to a poor fit [42].

In particular, some classes of background events will contain multiple particles in the cone and will not be well represented by a single straight shower. For such events, the χ^2/NDF of such background event will be larger than the electron shower, and they can be removed by the very loose requirement that $\chi^2/NDF < 100$.

5.2.3 ECal - HCal Visible Energy

Several electromagnetic shower reaches the HCal Region, no matter it is an event originating in the Tracker, it has to go through ECal Region. Almost all of the electromagnetic shower energy deposited in the Tracker should be deposited in the ECal and a tiny amoung in the HCal. The definition for the

Visible Energy Asymmetry on this thesis is

$$\text{Asimmetry}_{E-H} = \frac{\text{VisE}_{ECal} - \text{VisE}_{HCal}}{\text{VisE}_{ECal} + \text{VisE}_{HCal}}. \tag{5.1}$$

On this analysis, we set the asymmetry energy at $A_{E-H} > 0.6$.

5.2.4 Maximum Tranverse Spread

After the track is computed from a shower cone, the energy weighted mean residual distance of clusters from the shower axis was calculated to determine the transverse spread of energy from the shower axis.

The electromagnetic showers from a single electron will have a greater spread in this variable than is expected from single minimum ionizing particles. However for the background events where this larger transverse size is comming from the nearly overlapping tracks, will tend to have a larger transverse spread than electron showers.

In some cases, when two particles overlap in the shower cone with a small opening angle, it is possible that in one view the two tracks may accidentally overlap giving a small transverse spread in that view. However, if the transverse energy spread is calculated in each view, the maximum value of the three views will be affected by the opening angle between the two overlapping tracks.

By contrast, a single electromagnetic shower will have approximately the same transverse spread in all three views. Thus, the maximum root mean squared (RMS) of transverse residual among three views has sensitivity to distinguish two track background events [42].

To get the maximum transverse spread, the follow equation is used:

$$\text{RMS of transverse residula}_{X-view} = \left[\frac{1}{E_{X-view}} \sum_{i,X-view} (\Delta t_i)^2 e_i \right]^2. \tag{5.2}$$

After some studies, it was found that this quantity is required to be < 65 mm to reject events with two or more overlapping tracks in the shower cone.

5.2.5 Energy Balance

As it was explained on the previos chapter, the scintillator plane configuration follows the XU-XV pattern, then the electromagnetic shower will deposit 50%

of the energy in the X-view and 25% of the energy in the U and V-views.

The Energy balance between three views can be expressed as two conditions $E_x - E_u - E_v \approx 0$, and $E_u - E_v \approx 0$.

For background events with multiple particles, the energy balance is not guaranteed within the shower cone. The energy balance cut is useful to reject misreconstructed events [42]. The energy balance metric is given by these equations:

$$E_{XUV} = \frac{E_X - E_U - E_V}{E_X + E_U + E_V}. \tag{5.3}$$

$$E_{UV} = \frac{E_U - E_V}{E_U + E_V}. \tag{5.4}$$

The cuts applied on these equations to select the signal event are

$$E_{XUV} < 0.28 \quad \text{and} \quad E_{UV} < 0.28. \tag{5.5}$$

5.2.6 The End of the Shower in the Second Module

Using the most downstream position of an electromagnetic shower in the detector can give us a handle to reject some types of background events. Even the most energetic electromagnetic showers will not penetrate far into the HCal because its has 1 inch steel absorbers, not matter how close to the downstream of the detector the shower begins. See the Figure 5.5.

The electromagnetic shower loses most of its energy in the ECal ($\sim 8X_0$), and the remaining showering particles cannot reach too deep into the HCal.

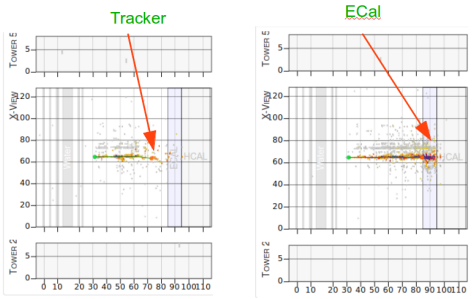

Figure 5.5: This figure shows true electron on different region of the detector.

When a true electromagnetic shower, at the end of the shower, has a high energy photon, that can cross few modules in the HCal before, pair production

is done typically will result in just few hits in the next one or two downstream HCal modules. Therefore, it is desirable that the definition of the shower end point should not be sensitive to such straggling low energy photons [42].

Then, the shower end position is defined as the most downstream hit in a triplet of planes in one each view, all of them with hits, which is not longer extent than five consecutive modules.

If a triplet candidate is more than five modules in extent, then the most downstream hit of that triplet is ignored, and the next most upstream triplet is considered until the five module criteria is meet [44].

The shower end position is required to be between modules 70 and 112, i.e. near to the upstream end of the HCal or close to the downstream end of the ECal Region.

5.2.7 Dead Time

How it was explained in the Simulation Chapter, the data acquisition has some insensitive "dead time" after hits, i.e. the time that the electronic needs to process the hit information.

In order to avoid incorrect reconstruction due to the effect of dead time, the channels upstream of the start of the reconstructed shower cone are checked to see if these channels are dead at the time of the interaction. If there are such dead channels, then the reconstructed vertex position may be shifted downstream from its true value, and this will have a cascade of negative effects in the entire reconstruction [42].

Considering the reconstruction process of the candidate electron track: it is extrapolated through two upstream modules, or four planes to find a central strip in each plane. The total number of dead channels on these strips and the adjacent strips in each of the four planes is required to be no more than one.

5.2.8 Neighborhood Energy

Since the experimental signature of Neutrino Electron Scattering is a single very forward electron, then the reconstructed candidate event should be a well isolated shower with little portion of other nearby activity.

In principle, a sum of all the energy outside the shower cone could be used to ensure a single electromagnetic shower, but this quantity is maximally sensitive to overlapping energy from pileup in the detector.

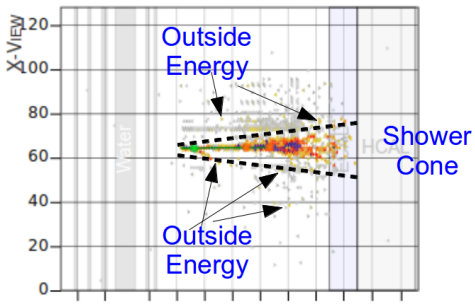

Figure 5.6: The Neighborhood Energy is the energy into the 5 cm region outside of the shower cone.

Some times is possible to have other interaction or activity at the same gate, and we want to conserve this event, therefore only the nearby "neighborhood" energy to the shower cone is used to check if an electromagnetic shower is isolated. The Neighborhood Energy is defined as energy contained in a region within 5 cm of the outer boundary of the shower cone, see Figure 5.6.

Some times the energetic electrons can produce a shower which is slightly wider than the cone. To maintain good efficiency at high energies, the neighborhood energy cut is loosened linearly above the electron shower cone energy of 7 GeV. The neighborhood energy cut, shown as the red line in Figure 5.7.

Originally in the first studies, these cuts were set to be constant, now the conditions applied for this cut are

$$\text{Neighborhood Energy} = \begin{cases} < 120 & \text{if } E < 7 \text{ GeV} \\ < 7.82E + 65.22 & \text{if } E > 7 \text{ GeV} \end{cases} \tag{5.6}$$

5.2.9 vtxToShower

Using the information from the Figure B.6 and applying it to the Equation B.7, it is possible to detemine the slope from the vertex to the maximum of the shower, therefore

$$= \frac{Eb}{\Gamma a} \left(\frac{0.7 t_{Max}}{e} \right)^{0.7 t_{max}} \frac{1}{t_{Max} X_0} \tag{5.7}$$

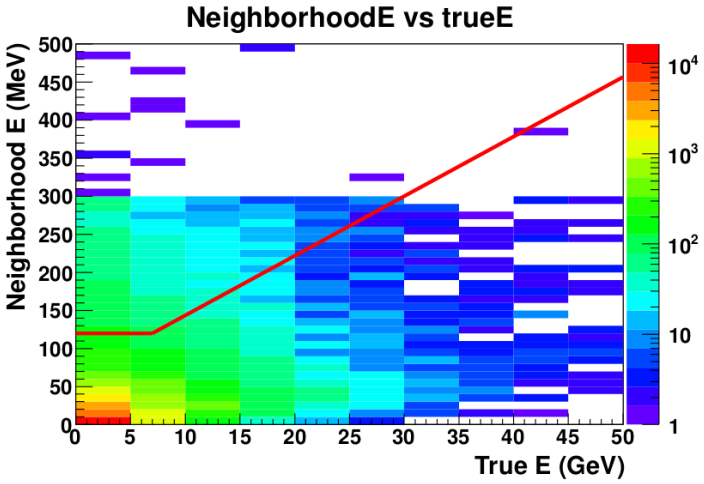

Figure 5.7: Neighborhood Energy vs True Energy, the selected event are below the red line [42].

Therefore, the following quantity is, on average, approximately constant for an energetic electron shower:

$$\frac{1}{E}\frac{(dE/dx)_{Max}}{x_{Max}} \sim \text{constant}, \tag{5.8}$$

although on an event by event basis, this quantity does vary due to the stochastic behavior of shower development. A low value of this cut means the particle appears minimal ionizing, like a muon. But a high value it is characteristic of background events with overlapping short tracks stopping not too far from the vertex [44], for example when a non- relativistic recoil proton stops inside the shower cone. It is requiered

$$\frac{1}{E}\frac{(dE/dx)_{Max}}{x_{Max}} < 5. \tag{5.9}$$

5.2.10 Peaks In ECal Region

Due to that a single electromagnetic shower is considered, one of the main backgrounds is a single photon background from the π^0 decay ($\pi^0 \to \gamma\gamma$), where one of the two photons is not observed. This happens for one of two reasons as follows:

First, the energy of one of the photons is very small, or π^0 is very energetic and then the two photons are too close or nearly collinear in the original π^0 direction.

In the other case, the two photons may not be reconstructed separately if their opening angle is too small. The photons travel a significant distance in the Tracker before they interact, but never more than a very short distance in the ECal because of the high pair production cross-section in the lead absorbers.

If the π^0 decays into two photons with a small opening angle then both may be within the same shower cone, but this does not mean that they are not separated transversely in space. The Figure 5.8 illustrates such a case where two peaks in the transverse projection can be identified within a single shower cone.

The event selection looks for such peaks in the ECal region, where the photons lose most of their energy, and it requires only one peak(shower).

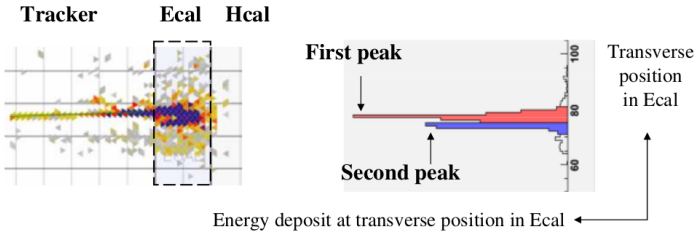

Figure 5.8: $\pi^0 \rightarrow 2\gamma$. Left: Event display, the square enclose the ECal Region, where 2 peaks appear. Right: Energy deposited for each photon [42].

5.2.11 Upstream Interactions

To select the electron candidate events inside of the fiducial volume, a neutrino interaction that happens upstream of the fiducial volume may contribute to the background if its event vertex is misreconstructed.

The upstream region includes the Nuclear Target Region and material in front of the detector; such as Helium Target and Veto wall, so the upstream region contains significant mass and therefore a large rate of neutrino interactions.

As an example, a neutral current interaction with π^0 in the Nuclear Target region could simulated the signal, since a photon from the π^0 decay will typically travel through detector about one radiation length without making a track, and may produce an electromagnetic shower starting in the fiducial volume. Fortunately, such electromagnetic showers point back to the location of an upstream neutrino interaction [42].

The total energy is calculated inside a cylinder of radius of 30 cm and whose center axis is the upstream extrapolation of the reconstructed electron candidate track. This energy is calculated in three views. If there is localized activity near the true neutrino interaction vertex, then the extended z distance of the energy in all three views should overlap.

Each pair of views is checked for such overlap and the deposited energy is only considered in one view if there is such an overlap. Events with all three possible overlaps are rejected if the energy in the overlap region is > 300 MeV.

5.2.12 Non-trackable Cluster in Tracker

One of the basic cuts is the minimum energy cut, where the electron candidates was required to have an energy great than 0.8 GeV, it due to the very high background at lower energies comming from the ionization process.

Even with this requirement, most backgrounds are still concentrated between 0.8 and 2 GeV, and therefore extra selection cuts are useful to reject the background in this region.

The effectiveness of the particle identification methods depends on the energy of candidate events, because both of the longitudinal and transverse size of the electromagnetic shower, and in particular the amount of energy deposited in the ECal Region have a significant dependence on energy.

While most of the electrons below 2 GeV do still reach to the ECal, they often do not deposit sufficient energy in the ECal to rely on that energy for background rejection. In fact, electrons and charged pions at low energy can be much more easily confused in the ECal by at lower energies than they can be at higher energy. Because of the small and fluctuating energy in the ECal, these extra selection cuts rely on the shower development in the tracker [42].

The pattern of energy deposited by a charged pion that doesn‘t undergo inelastic interactions is consistent with a track of a Minimum Ionizing Particle (MIP) in the Tracker. In elastic interactions, which typically make a track, the abruptly changes directions, or kinks, are already removed by the reconstruction quality cuts.

When an electron traverses the tracker, it starts to shower by bremsstrahlung and subsequent pair production of those photons, but due to the particle multiplicity is still low, the resulting electromagnetic shower is slender. However,

the overall transverse size of the electromagnetic shower is still slightly wider than that one of the MIP particle.

The transverse size of the electromagnetic shower can be quantified by the different topologies of clusters, for example, these slender electromagnetic showers may make a number of three strip clusters before reaching the ECal, but MIP particles will almost always only create one or two strip clusters, which we categorize as "trackable" clusters along the track [42].

The fraction of non-trackable cluster in tracker is used to reject the MIP-like track in the Tracker. Useful discrimination is only possible when the interaction vertex is in the upstream part of the fiducial volume, so the particle can travel a sufficient distance and begin to shower before it enters into Ecal.

For electromagnetic candidates with energy below 2 GeV, whose vertex position is not too close to ECal, and with vertex module < 65, the fraction of non-trackable clusters in the Tracker is required to be < 0.05 to reject MIP-like tacks [42].

5.2.13 Rock Muons Rejector

The Ana/NuE package includes the option to remove the Rock Muons, those are the muons generated by the neutrino interaction with the rocks between the decay pipe and the MINERνA Detector. But some times when the rock muon track has a gap or not deposited enough energy in the upstream and downstream of the detector, it is not considered like a rock muons, and it falls on the samples.

To remove these events, it is used the information coming from the Nuclear Target Region and HCal region, if at the same slice it appears on both regions, it is considered as rock muon, and the track information will be removed.

The Figure 5.9 shows the Electron Energy and the kinematic constrain plot after applying all the precuts (geometrical and good quality reconstruction), the last one, just for the range of $E\theta^2 < 0.04$ GeVrad^2.

5.3 Signal Selection

After applying the geometrical and good reconstruction cuts, the electron energy spectrum is shown in the Figure 5.9. Due to that the kinematic constraint for Neutrino Electron Scattering is known, it is expected to have those events

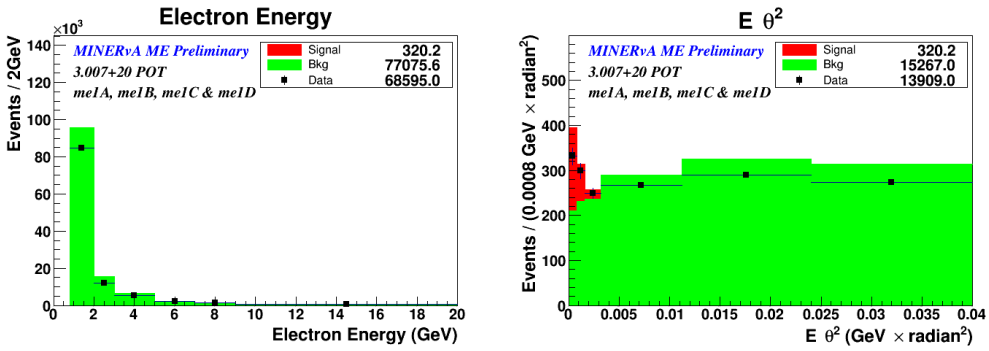

Figure 5.9: After applying the Pre-selection cuts. Left: Electron Energy. Right: Kinematic Constraint. It can be seen how after applying the pre-selection cuts the signal events in the left plot does not appear even the pre-selection cuts reject almost the 70% of the background.

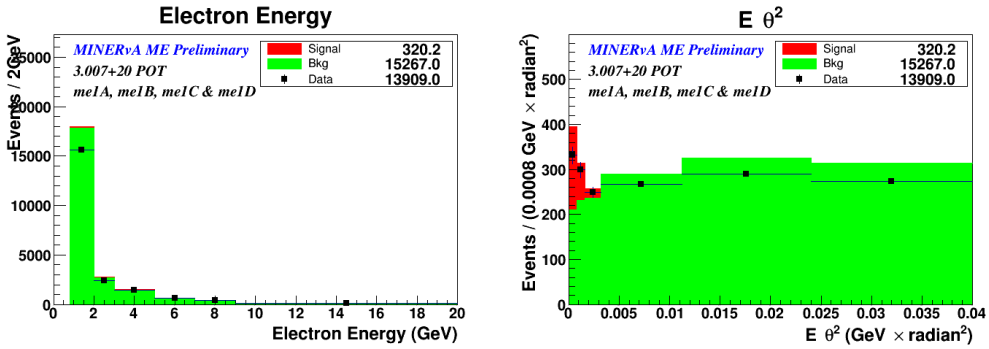

Figure 5.10: After applying all the Pre-selection cuts and the soft cuts on the kinematic contraint, $E\theta^2 < 0.04$ GeVrad^2. Left: Electron energy. Right: Kinematic Constraint, both plots after the shoft cut on $E\theta^2 < 0.04$ GeVrad^2

at very low values in $E\theta^2$, so it is possible to apply a soft cut on the kinematic constrain just to study and see the effect of each cut that will be studied in this chapter.

This means, from now the following plots will include the $E\theta^2 < 0.04$ GeVrad^2 as default cut. The Figure 5.10 shows the Electron Energy.

At this point, the sample has an efficiency of $\sim 82\%$, but the samples still conserve the main background: gammas and electrons coming from ν+$n \rightarrow p$+e and neutral current π_0, those will be removed in the final cuts.

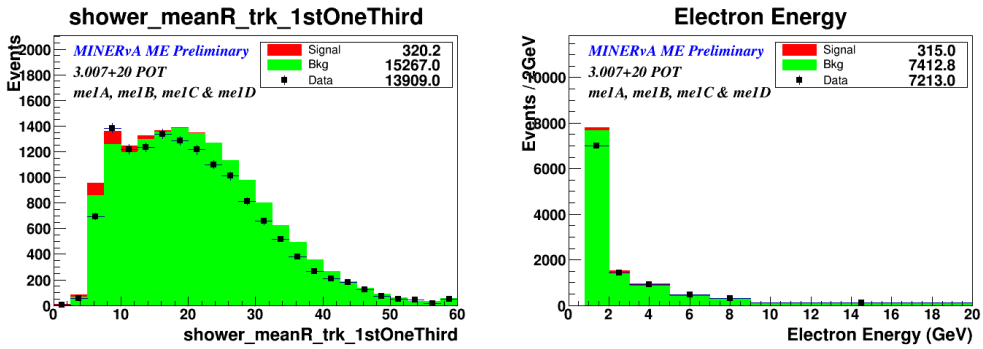

Figure 5.11: Left: Transverse Residual RMS in the first third of the shower at the Tracker Region. Right: Electron Energy for the events contained under the first 20 cm on the left plot.

5.3.1 Shower Mean R at the 1rstThird of the Shower

At the beginning of the electromagnetic shower from electrons, it does not show significant transverse energy spread because the particle content at the start of the shower is still a single electron until the first hard bremsstrahlung interaction, and the radiation length is more than ten modules in tracker for electrons in the beam direction.

However, background events with multiple particles may have some transverse spread in energy even if they are within the shower cone.

As the shower develops, the electromagnetic shower will eventually show significantly wider transverse distribution near its shower maximum, so the discrimination will not be useful in this region. Therefore, the transverse energy distribution is calculated at the first one third of the shower in the Tracker Region using the method described previously on Maximum Tranverse Spread cut, but summing over all three views [42].

The energy weighted transverse residual RMS in the first third of the shower in the Tracker region is required to be less than 20 cm.

On the Figure 5.11, there is the electron energy after applying the cut in the first third of the shower in the Tracker Region.

5.3.2 Higher Angle Rejector

Sometimes the electron candidate events in the fiducial volume, has a large angle with respect to the z-axis, and it may escape out the side of the inner

detector. For such events if the particle is minimally ionizing like a muon, it leaves little energy in the SideEcal before exiting, and the hits in the SideEcal extend to the edge of the detector.

However, if the exiting particle is making an electromagnetic shower, then it leaves significant energy with a typically large transverse energy spread.

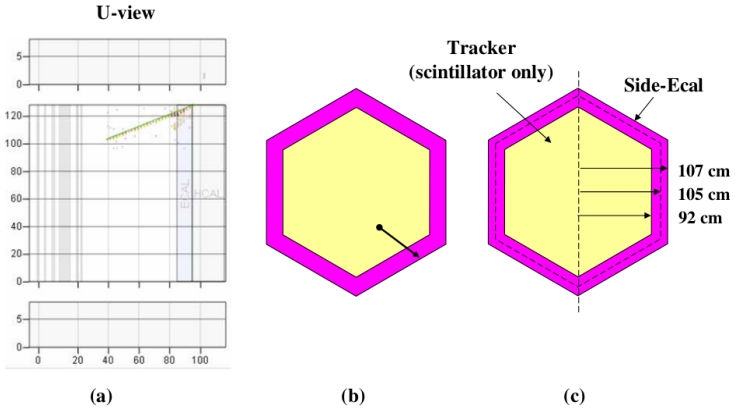

Figure 5.12: (a) Track going out from the Inner Detector on U-view, (b) Same track but on transversal view, and (c) Transversal view of the Inner and Outer Detector. [42].

The transverse position at the end of such shower is measured by the energy centroid, and because of the transverse spread of energy deposited in such events, the apparent position of the exit shower can be far from the edge of the detector.

Due to the Inner Detector is hexagonal, an exiting track should escape through one of six sides, and this means that the track will often only reach the edge of the detector in one view [42].

For example, in the event shown in Figure 5.12 (a), it reaches the side of the event display in the U-view, but in the X and V-views the track appears ending in the middle of the detector.

To measure the proximity to the edge of the detector, the maximum of the absolute value of the transverse position from each of the three views is calculated. This is equivalent to the apothem of the minimum side hexagon centered along the detector z-axis that encloses the shower end transverse position. This is required to be less than 1050 mm, which is at 2 cm from the boundary of the Inner Detector as shown in Figure 5.12 (b) and (c).

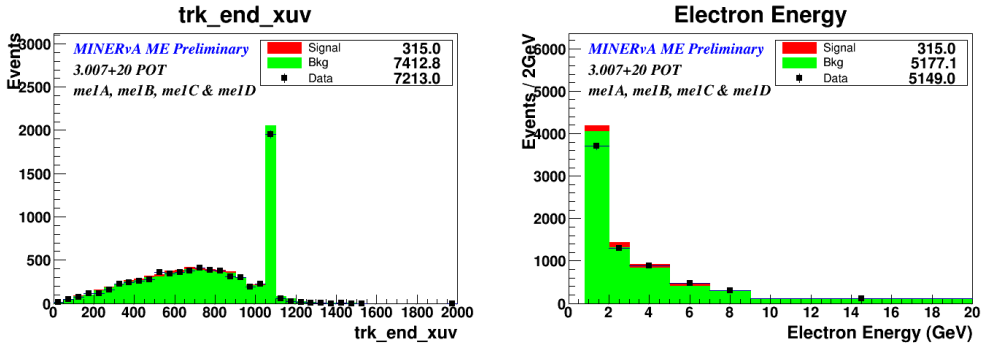

Figure 5.13: Left: The maximum absolute value of the EM Shower transverse position. Right: Electron energy for the signal candidate events under the first 1050 mm on the left side plot.

The Figure 5.13 shows the strong effect of this cut over the background, this cut can be used to reject some events coming from the outer detector.

Some events coming from Neutrino Electron Charge Current Quasi-Elastic(NuE-CCQE) are removed with this cut, because the electrons have an angle more bigger than the electrons coming from Neutrino Electron Scattering. If the NuE-CCQE electron is at the edge of the side fiducal volume, it will scape to the Side ECal. The Figure 5.14 shows an example of the NuE-CCQE event.

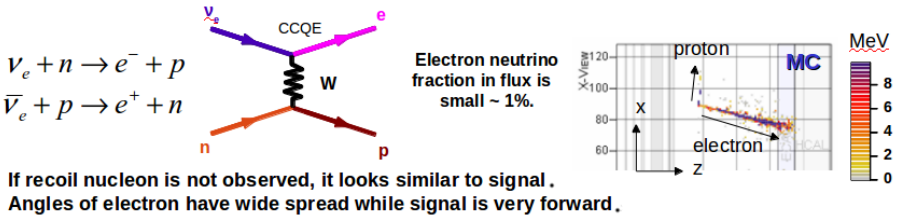

Figure 5.14: Example of one Electron-Neutrino Charge Current Quasi-Qlastic event, it looks like signal event due to that some times the energy of the proton is too low to be reconstructed and the interaction looks like a single electron in the final state.

5.3.3 Photon Rejector

In the case of the Neutral Current Single π^0 production, the only visible particles in the interaction may be the photons from the π^0 decay. In some cases, one of the two photons may not be observed in the detector because it has low

energy, and it can look like a single electromagnetic shower. See Figure 5.15.

Also, when the produced π^0 is highly relativistic (at high energy), the decay of π^0 may produce two photons with a very small opening angle. With the small opening angle, these two photon showers can nearly overlap and appear like a single electromagnetic shower.

Since the photon shower development processes are very similar to an electron shower, it can mimic the signal. See the right side of the Figure 5.15.

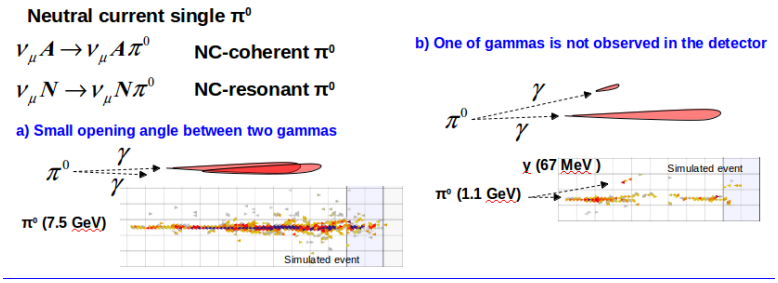

Figure 5.15: a) High energetic π^0 decay into two gammas with small opening angle. b) In some cases just one of the two photon is visible from π^0 decay.

At high energies the pair production dominates and the mean free path of the photon is $9X_0$, where the radiation length, X_0, in the Tracker Region is about 50 cm.

However, photon and electron have an important difference at the beginning of the shower. As it is explanied on Apendix Section B. When an electron travels in the detector, it initially loses energy due to ionization until the multiplicative processes in electromagnetic shower development increases the shower multiplicity.

The most common first steps in a photon shower for energies above 10 MeV is pair production of e^-e^+, and thus at the start of a photon shower typically has twice dE/dx than seen in electron showers. As the electromagnetic shower cascade develops, the number of particles increases and dE/dx continues to increase and become more influenced by the stochastic fluctuations in shower development.

Therefore, it is very useful to calculate dE/dx near the beginning of shower to separate electrons and photons. But if only few planes are included in the calculation, the dE/dx has broad distribution due to variation of the vertex

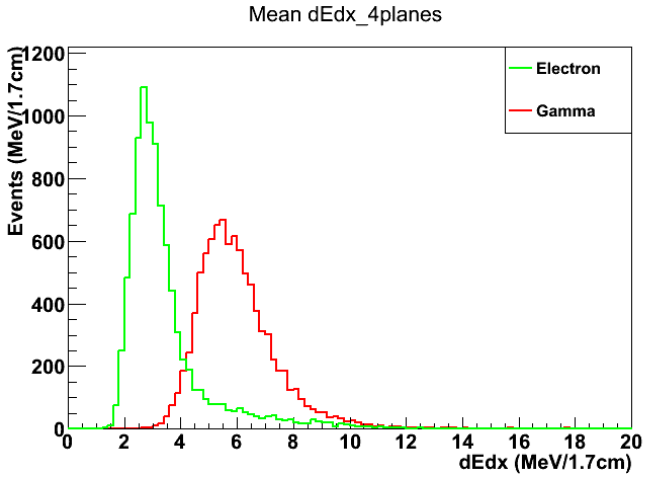

Figure 5.16: Energy loss per length for electron and photon at the first 4 planes. The distributions are made using a Monte Carlo Particle Cannon (MC-PC) samples.

position within the first scintillator strip and due to the energy resolution in the detector.

Increasing the number of planes included in the sum decreases these smearing effects. Measuring the dE/dx over first 4 scintillator planes it found to be a good choice for optimal discrimination.

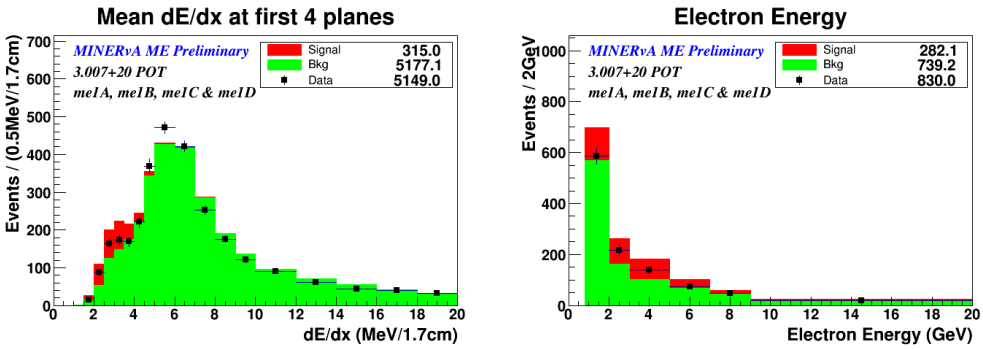

Figure 5.17: Left: Energy loss in the firs four planes at the beginning of the electromagnetic shower. Right: Electron energy for the signal candidate events under 4.5 MeV/1.7 cm on the left plot.

We define the mean measured energy loss per length as

$$\langle dE/dx \rangle_{1-4} = \frac{1}{4} \sum_{\text{plane}i=1}^{4} dE_i \times \cos\theta, \tag{5.10}$$

where dE_i is energy deposited in the $i-th$ plane and θ is the angle of shower in detector coordinates. Monte Carlo simulation for electron and photon dE/dx samples are compared in Figure 5.16.

Electron and photon $\langle dE/dx \rangle_{1-4}$ have a peak near 3 MeV/1.7 cm and 6 MeV/1.7 cm respectively, and indicates a good discrimination between electron and photon showers.

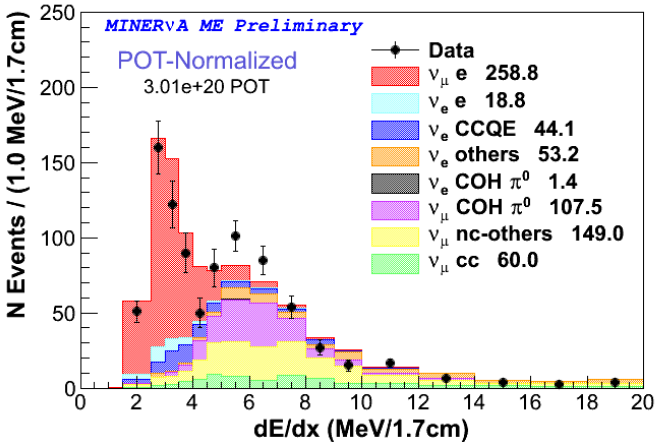

Figure 5.18: Energy loss in the first four planes for Data and MC.

After the efficiency analysis with the electron and photon MC-PC samples and the purity studies using the general MC, the $\langle dE/dx \rangle_{1-4} < 4.5$MeV/1.7cm is required for this analysis.

Other experiments plan to use this technique in the future to discriminate electrons from photons in neutrino interactions. The Figure 5.18 shows the dE/dx distribution for Data and MC sample.

The plot on the Figure 5.18 shows the $dEdx$ in the first four planes for data and the simulated events. The main signal cadidate event are under 4.5MeV/1.7cm.

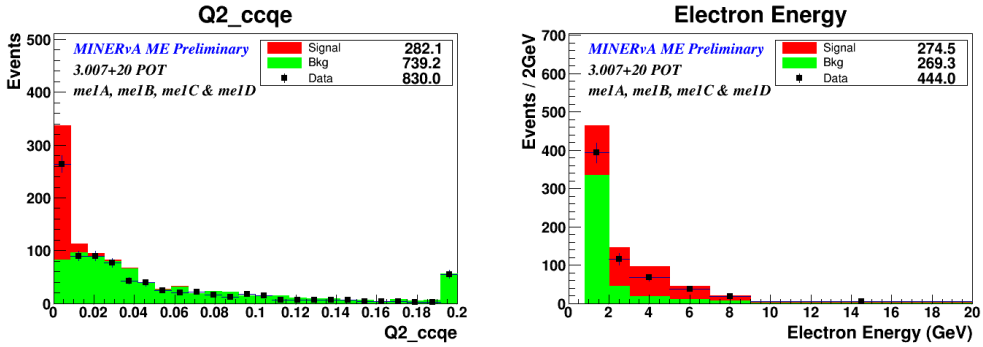

Figure 5.19: Left: Q^2 distribution. Right: Electron Energy for the signal candidate events after the cut on $Q^2 < 0.025$ GeV^2.

5.3.4 The Q^2

Before applying the main isolator cut, that is useful to removed NuE-CCQE background events effectively at low energy, but is less effective for high energy electrons. The electrons from NuE-CCQE also are observed at smaller angles at higher energies, so the angular resolution becomes more important.

As an extra cut, the Transfered Momentum (Q^2) is reconstructed directly under the assumption of NuE-CCQE kinematics

$$E_\nu = \frac{m_n E_e - m_e^2/2}{m_n - E_e + p_e cos\theta}, \tag{5.11}$$

$$E_\nu = 2m_n(E_\nu - E_e), \tag{5.12}$$

where E_ν is the neutrino energy, E_E is electron energy, p_e is electron momentum, m_e is the electron mass, and m_n is neutron mass.

The Q^2 for the Neutrino Electron Scattering is gived by the next equation:

$$Q^2 = \frac{2m_p^2 E_e - m_p m_e^2}{m_p - E_e(1-\cos\theta)} - 2m_p E_e. \tag{5.13}$$

On this analysis, after several efficiency and purity studies, Q^2 (CCQE) $<$ 0.025 GeV^2 is required to reject high energy electron from NuE-CCQE. This is an small addition to the existing $E\theta^2$ cut, and is also only a function of the electron angle and electron energy [42].

5.3.5 Main Signal Isolator

With the dE/dx selection we are removing most of the backgrounds from photons, the remaining major background is from NuE-CCQE, $\nu_e n \rightarrow ep$ and $\nu_e p \rightarrow e^+ n$.

If the recoiling nucleon is not observed in the detector, which is common at low Q^2 , the final state is a single electron or positron. The MINERνA Detector does not distinguish electron from positron due to lack of magnetic field. Even though ν_e content of the neutrino beam is only about 1%, the NuE-CCQE background is potentially very large because the neutrino electron scattering cross-section is a factor of 2000 smaller than neutrino nucleon scattering.

Since the observable particle content is identical, no particle identification requirement can reject NuE-CCQE background directly. However, neutrino electron scattering can be separated using a kinematic constraint which is derived in Appendix Section C.

$$E\theta^2 < 2m_e, \tag{5.14}$$

where E is electron energy, θ is angle of the electron with respect to the neutrino beam direction, and m_e is electron mass.

The CCQE background, in which the target is a nucleon, can have values of $E\theta^2$ up to $2m_N$, where m_N is the mass of the target nucleon. The $E\theta^2$ cut was previously used by the CHARM II experiment to measure the weak mixing angle from Neutrino Electrical Scattering [21].

To use the kinematic constrain, Equation 5.14, is necesary to make the Beam Angular Correction. At the location of the MINERνA Detector, the beam points down by $\sim$3 degree so that the NuMI beam arrives near the surface at the far detector location of MINOS in northern Minnesota, at 735 km from MINERνA.

While the direction of the beam is well known by survey relative to outside references, any measurement of track angles in the MINERνA Detector is based on the MINERνA Detector coordinates. If there is a misalignment of the MINERνA Detector with respect to the beam, the measured angle at MINERνA will be shifted [42].

The beam angle is important for many measurements in MINERνA. For example, the neutrino energy reconstruction of CCQE events depends on the muon angle with respect to the beam direction.

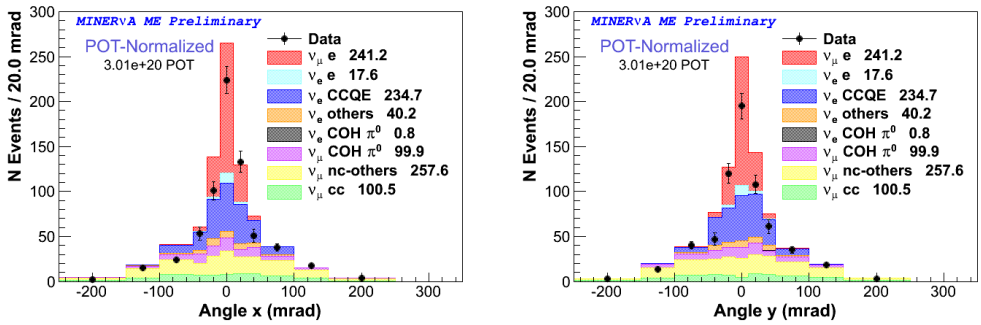

Figure 5.20: Angular distributions on the MINERνA Detector frame before applying the angle beam correction.

But due to that the neutrino electron scattering produces very forward electrons, some at small angles with respect to the beam direction, the angles in the x-z and y-z planes with respect to the beam direction peak sharply at zero, other interactions have a more broad distribution [42].

Due to that the peak electron direction is the same as the beam direction, the Neutrino Electron Scattering signal can help to check the detector alignment if it is close enough so that the event selection has not affected the distribution.

In the Figure 5.20 and 5.21 it is shown angle x and y distributions respectively for studied sample, before $E\theta^2$ cut is applied. Peak positions of angles in the x-z and y-z planes, θ_x and θ_y, peak at the beam direction. Note that in the Neutrino Electron Scattering, the beam angle has a strong effect on the $E\theta^2$ event selection.

The angle in the y-z plane, θ_y is slightly shifted with respect to the expectation. A correction to the beam angle on the data sample was applied to restore/match the peak position to zero angle, and $E\theta^2$ was recalculated using this correction.

Due to that the angles x and y are measured on the MINERνA Detector coordinates, is necesary make a transformation to the Beam Frame, to do it, we are using the Equation 5.15.

$$\begin{aligned}\theta_{w.r.t}beam = acos(&-n_x sin(\phi_{beam}+\phi_x)\\ &- n_y sin(\theta_{beam}+\theta_y)cos(\phi_{beam}+\phi_x)\\ &+ n_z cos(\theta_{beam}+\theta_y)cos(\phi_{beam}+\phi_x)) \quad (5.15)\end{aligned}$$

where, n_x, n_y and n_z are the unitary vectors for x, y and z directions, re-

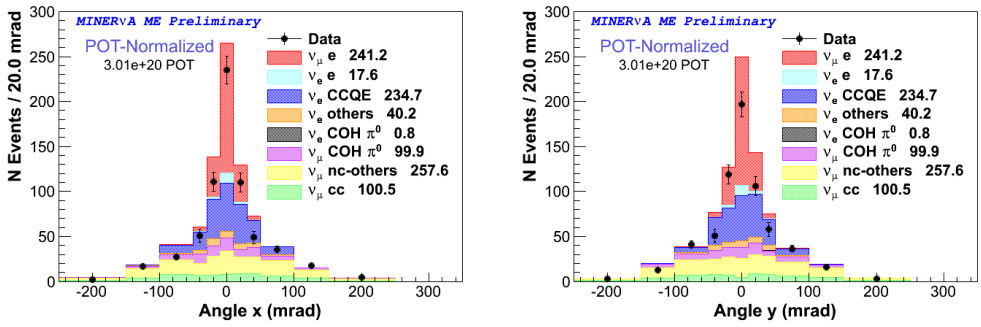

Figure 5.21: The angular distributions. Left, angle on x-axis. Right: angle measured with respect to the y-axis. The distributions are after applying the beam angle correction.

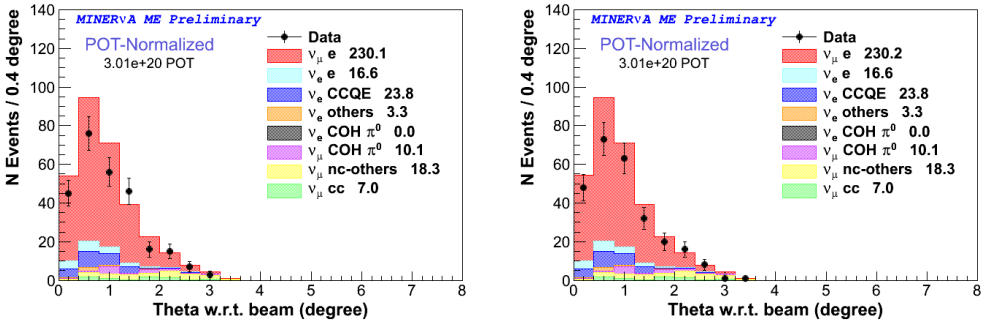

Figure 5.22: Angle of the outgoing electron measured with respect to the beam. Left: Before applying beam angle correction. Right: After applying the beam angle correction.

spectively. θ_{beam} and θ_y are the angle of the beam and y beam angle correction on data, measured on the YZ plane, with respect to the z axis. ϕ_{beam} and ϕ_x are the beam angle and beam angle correction on data, measured XZ plane, with respect to the x-axis.

The Figure 5.22 shows the angle of the electron coming from the neutrino electron elastic scattering, measured with respect to the beam direction, in this figure there is the effect of the beam angle correction.

The Figure 5.23 shows the $E\theta^2$ distribution of the candidate events after the beam angle correction and all event selection cuts have been applied except the $E\theta^2$ and Q^2 cuts. The signal event are peaked at very small $E\theta^2$ value.

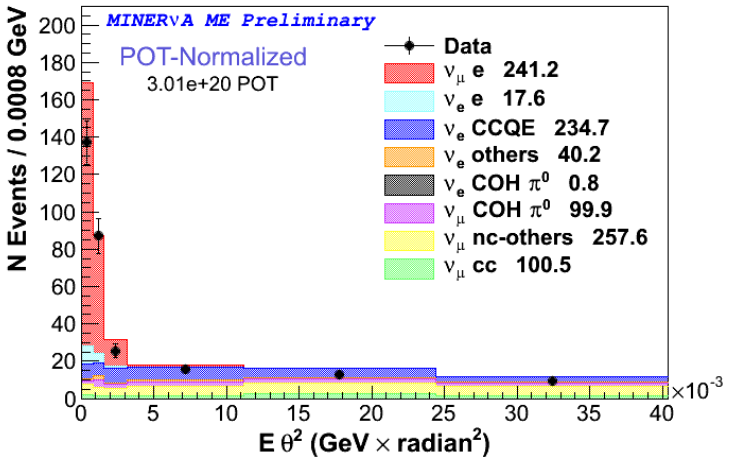

Figure 5.23: $E\theta^2$ distribution, before applying the last 2 cuts. The predicted signal events are too close to the origin. The final cut to isolate the $\nu - e$ Scattering events are made on $E\theta^2 < 0.0032\text{GeV rad}^2$.

Note that the signal peak is much wider than $2m_e \approx 1$ MeV due to the smearings effects from the detector, as angular and energy resolution for the reconstructed events.

$E\theta_2 < 0.0032\text{GeV} \times \text{rad}^2$ is applied for neutrino electron scattering analysis. After the $E\theta^2$ cut, finally the Electron Energy spectrum is obtained and shown in the Figure 5.25

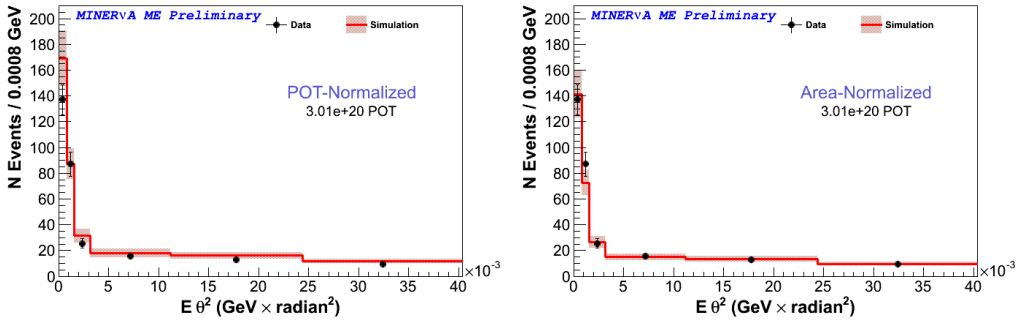

Figure 5.24: $E\theta^2$ distibution with error bands. Left: POT normalization. Right: Absolute normalization.

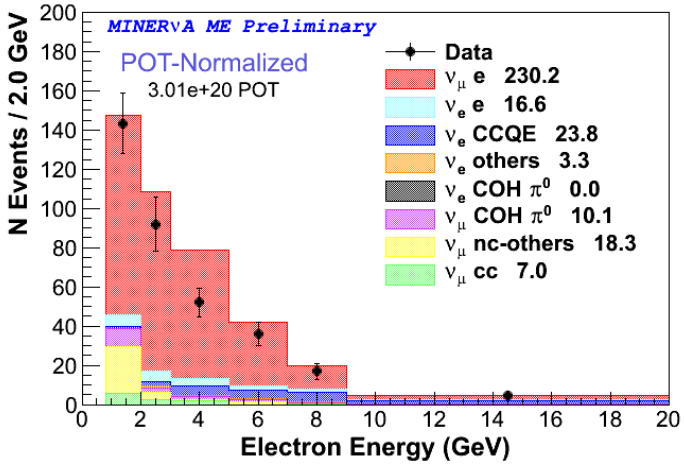

Figure 5.25: Electron Energy spectrum after applying all the selection cuts and the beam angle correction.

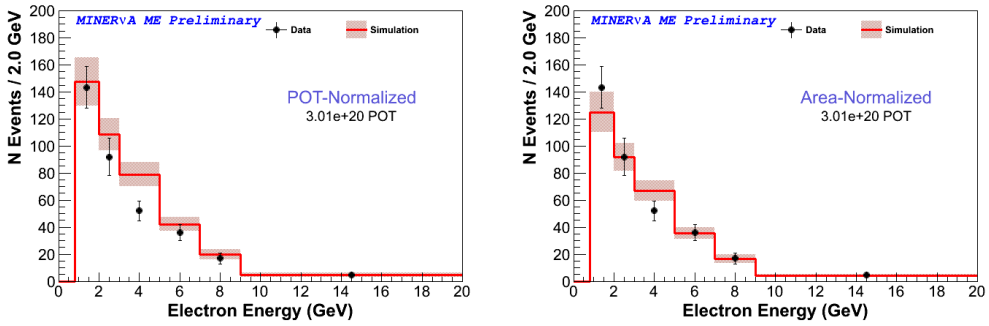

Figure 5.26: Final Electron Energy spectrum, after applying all the selection cuts. Left: POT normalization. Right: Absolute normalization.

Chapter 6

Neutrino - Electron Elastic Scattering Analysis

6.1 Background Studies

The plot on the Figure 5.25, shows the predicted Neutrino Electron Scattering energy spectrum, and the predicted signal and background events, those are a fraction of the signal events.

Considering that the given is the right fraction of background present on the final data signal candidate events, and if this predicted background is subtracted to the data distribution, then a real measurement of the neutrino electron scattering events will be obtained. This procedure is subject to systematic uncertainties in the background Monte Carlo prediction, because a mismodeling of the background will bias the signal measurement.

The main uncertainties on the analysis comes from the neutrino flux and the cross-sections, instead for the background reactions, our poor knowledge for the hadron production is the main contribution to the flux uncertainties [42].

The uncertainties due to the flux are particularly problematic, since this measurement is to be used to constrain the neutrino flux.

The method to break the vicious circular reasoning and reduce the background uncertainties is to use the sidebands studies. A sideband is a portion of the data that fails one or more of the event selection cuts, this method is used to constrain the backgrounds.

The sidebands are used to tune the background predictions, this means that, the agreement between Monte Carlo simulation and data in the sideband region

is demanded.

The Tuning is a procedure that makes the Monte Carlo prediction similar to data by correcting normalizations on different background reactions, and extrapolating those normalizations into the signal region [42].

Whith this procedure, the uncertainties in the model are reduced but not eliminated, since these uncertainties may still giving result with uncertainties in this extrapolation. The sidebands also provide a test of the model and the uncertainties since one can study distributions of observables that are sensitive to the different reaction cross-sections in these sidebands, i.e. it is looked for the good data modeling at different regions.

The tuning will be optimal if the tuned parameter is the real source of the discrepancy between data and MC. If the physics model is wrong, the tuning may not perform very well; if the model is approximately correct or only good in certain regions of the sideband, and the sideband tuning is not fully useful to try to compensate some calibration or geometrical problems, then tuning will not be perfect but it is still useful to match data and Monte Carlo.

6.1.1 Parameters to Tune

In this analysis, the tunning in done using many sideband distributions throughly to test these predictions of the background within their uncertainties. Two different tuning parameters may have similar effects on one distribution but have different effects on the another distribution, this is because the data or MC events are correlated with ather variables.

In principle, will be ideal to tune all the free or uncertain parameters in the flux and cross-section model, however is more practical work and fit on an small number of non-degenerate parameters. The simplest case is just to fit for an overall correction to the rate of a given process. It should be tested if this simplification is acceptable by comparing distributions of observables in the data and simulation at the sidebands.

The Figure 5.25 shows the predicted background components after the final event selection. The total background consists of many different reactions which are governed by distinct physics models.

To apply the tune procedure, it is tunned the background components which are known to be most uncertain and have the biggest representation in the sig-

nal and sideband regions.

For the tuning, the reactions are classified as either Charged Current (CC) or Neutral Current (NC). Both are subject to uncertainties from the neutrino flux, but the cross sections for NC have additional uncertainties because the measurements of these reactions are few, and the uncertainties are therefore larger.

The largest component in background as shown in the Figure 5.25 is NuE-CCQE reaction, and here the major uncertainties in the model of NuE-CCQE events is due to the large uncertainty in the ν_e flux. Due to this all ν_e induced events are grouped together with one tuning parameter [42].

The Coherent-π^0 production is not tuned because it is an insignificant part of total background. Future analysis might attemp to tune either by improved sideband tuning or using CC-Coherent measurement.

In summary, the method for tuning parameters chosen for the sideband studies are four normalizations: one for all ν_e induced processes except Coherent-π^0 production, one for all NC-ν_μ induced processes.

After choosing the parameters to tune from the sideband data, it is used to chose the selections for defining sidebands and the distributions in those sidebands to fit and match Monte Carlo to Data.

6.1.2 Sideband Regions

Following the same procedure for the background studies made in the previous Low Energy analysis, that is described on the Reference 44, it is introduced two new quantities, which have not been used in the signal selection cuts.

Any track originated from the fiducial volume(Figure 5.12), is defined as a fiducial track. The length of such fiducial tracks that penetrates into the HCal region, is a good discriminant between tracks from electromagnetic showers, which do not penetrates far into the HCal, and MIP tracks such as muons from Charged Current interactions, which will typically penetrate deep into the HCal, this particles may be pions and kaons.

The main process in the background contribution for neutrino electron scattering is coming fron NuE-CCQE, to study, it is used the Min$[dE/dx_{26}]$, it is defined as the minimum measured deposited energy, dE/dx, from the second to

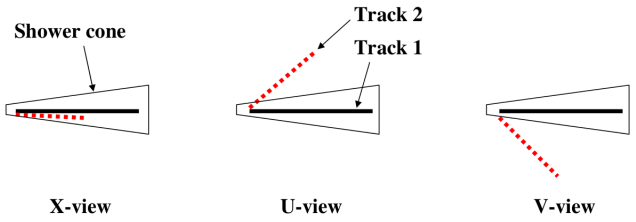

Figure 6.1: Example of NuE-CCQE event taked account on the signal selection.

sixth planes at the beginning shower from an electron candidate, the numbering are from the plane one at the vertex.

The main difference between the dE/dx in the first four planes (dE/dx_{14}) and this quantity (Min$[dE/dx_{26}]$), is that the second one is less sensitive to the possibility of a few planes with high deposited energy near the vertex. For example, in NuE-CCQE ($\nu_e + n \rightarrow e^- + p$), the recoiling proton may leave noticeable energy near the vertex that overlaps with the electron shower cone [42].

Typically these protons are not collinear with the electron, and some of the energy of recoil protons may not be fully contained within the shower cone. But even in these cases, some of the energy may overlap in one view as illustrated in the Figure 6.1.

More benefits beyond of the good resolution is the XU-XV plane configuration, it ensures that such overlaps cannot happen in every plane, and therefore MindE/dx_{26} will select dE/dx from one of the planes without an overlapping electron.

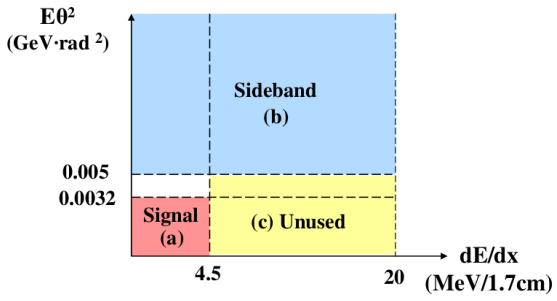

Figure 6.2: Sideband distribution in the $E\theta^2$ vs dE/dx_{1-4}. The picture is taken from the Reference 42.

When a low energy proton makes energy deposition only in first few planes, Min$[dE/dx_{26}]$ is not affected by the small vertex energy. Most NuE-CCQE

events will have Min$[dE/dx_{26}] < 3$ MeV/1.7cm [42].

The main and strong signal cuts on neutrino electron scattering is the dE/dx and $E\theta^2$, these have been requiered to be less than 4.5 MeV/1.7cm and less than 0.0032 GeVrad^2, respectively. The Figure 6.2 shows an scheme of how the sidebans were chosen.

After several studies, on different varibles and sidebans, it is decided to use the same sidebans selection than those used on the previous neutrino electron scatering study in MINERνA Low Energy.

The primary sideband, region (b), is defined to be all events with $E\theta^2 >$ 0.005GeVrad^2 and $dE/dx <$ 20MeV/1.7cm. Very high dE/dx tends to select complicated events which are not representative of the events that are into the background of this analysis.

The region $0.0032 < E\theta^2 < 0.005$GeV rad^2 is not used in the sideband, in order to avoid having a significant signal component in the sideband region. For sideband to avoid the mixed region that has both signal and background.

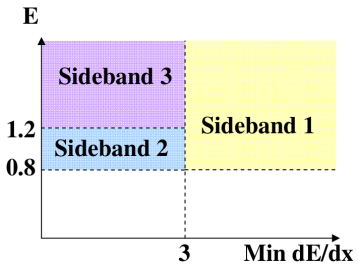

Figure 6.3: Sideband for Neutrino Electron Scattering, it is used the same sideband definition used on the previous Low Energy studies [42, 44].

Region (c), $E\theta^2 < 0.005$ GeV rad^2 and $4.5 < dE/dx < 20$ MeV/1.7cm, is not used because $E\theta^2 < 0.005$GeV rad^2 is a very restrictive requirement that selects a tiny population compared to the sideband, except for the case of the signal reaction.

The primary sideband ($E\theta^2 > 0.005$GeV rad^2) is a sample with many real electromagnetic showers, but most of these events are ν_μ-CC background because of the restrictive cuts in the analysis. Several cuts were dropped from the standard analysis to define the sideband to accept more of these events: the shower end transverse position was not longer required to be < 1050 mm, and the shower transverse spread in the first 1/3 of the shower was not longer

required to be < 20 mm. ν_μ-CC events dominate the events with shower end transverse position > 1050 mm region because these events contain side exiting muons.

The sideband is further divided into three sub-regions so that the sub-regions contain a different mixture of background components. If a particular background component is a small fraction of the overall sideband, it is difficult to constrain this sidebands.

The three sub-regions are shown in the Figure 6.3. This subdivision also helps to enhance shape differences in the distributions used in the fit. Without such shape differences, it is also difficult to constrain the different components that make up the background. The three regions are separated by Electron Energy and by MindE/dx_{26} [42].

6.2 Sideband Tuning

The sideband tuning method is performed by adjusting the normalization of each of the three background processes described above, to make the Monte Carlo simulation agreeable with the data distributions in each one of the three sidebands.

The normalization of ν_e induced processes, $\nu_\mu-$NC and $\nu_\mu-$CC processes, are simultaneously tuned using seven distributions in three sidebands to match normalization and shape of the simulated distributions with data.

The optimal normalizations are determined by a χ^2 fit, comparing the Data and Monte Carlo distributions as a function of the normalization parameters.

The χ^2 minimization is performed by the TMinuit minimization module in ROOT with the MIGRAD. The sideband tuning minimizes χ^2 in the seven distributions of sidebands one through three simultaneously.

The χ^2 used in the minimization, is the sum of the seven individual χ^2 decribed by

$$\chi^2 = \sum_m \sum_i \frac{\left(D_i^{(m)} - MC_i^{(m)}\right)^2}{MC_i^{(m)}}, \tag{6.1}$$

where m is histogram index, i is the bin index in an histogram, D is data histogram, and MC is MC histogram.

Variable histogram binning is used to ensure that the Monte Carlo simulation prediction has at least twenty entries in each bin. The χ^2 is a poor approximation of the true likelihood of the data distribution given the prediction when the number of entries in each bin is too small [42].

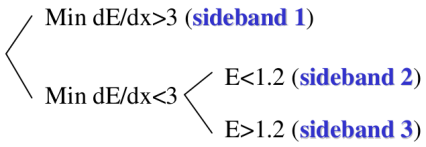

Figure 6.4: Sideband division ranges.

Remembering the division of the sidebands (Figure 6.4), and the use of different distributions helps to enhance shape differences in the distributions to use in the fit.

Such shape differences are necesary to constrain the different components that make up the background. The three regions are separated by Electron Energy and by the energy loss on the planes 2 to 6 at the begin of the shower.

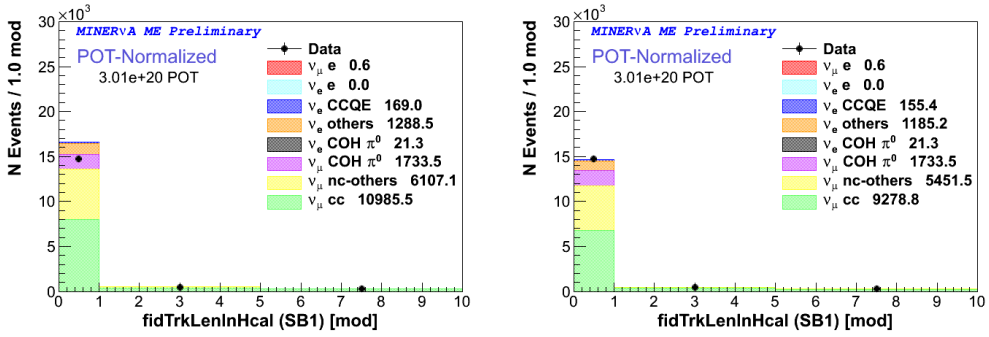

Figure 6.5: Fiducial track length inside of HCal Region for sideband 1. Left: before tuning. Right: after tuning.

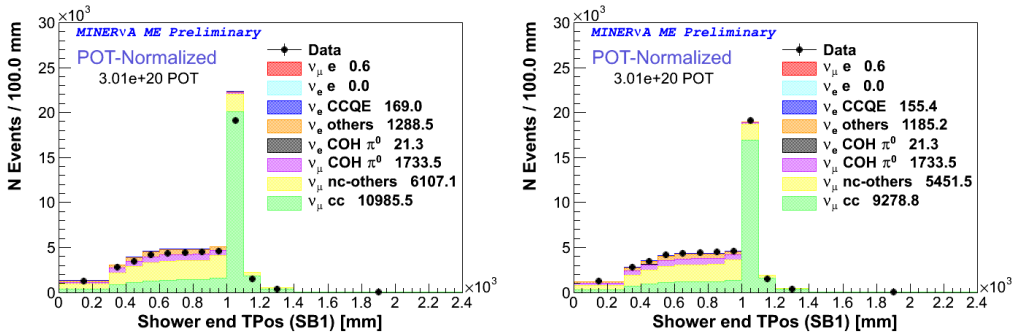

Figure 6.6: Track transversal shower end position for sideband 1. Left: before tuning. Right: after tuning.

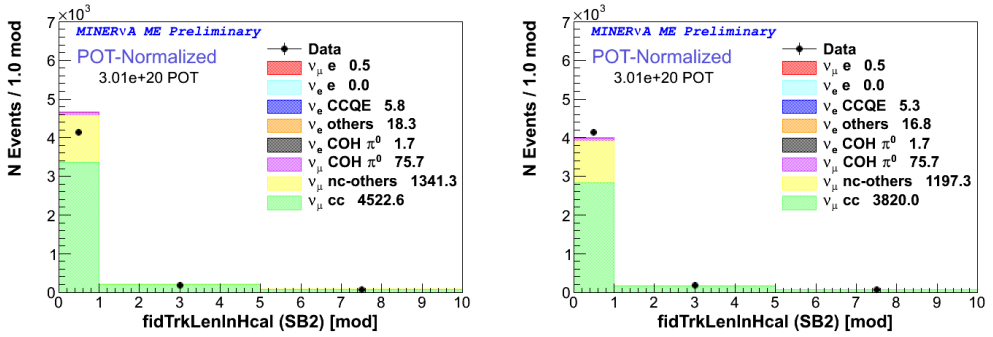

Figure 6.7: Length of the fiducial track inside of HCal REgion for sideband 2. Left: before tuning. Right: after tuning.

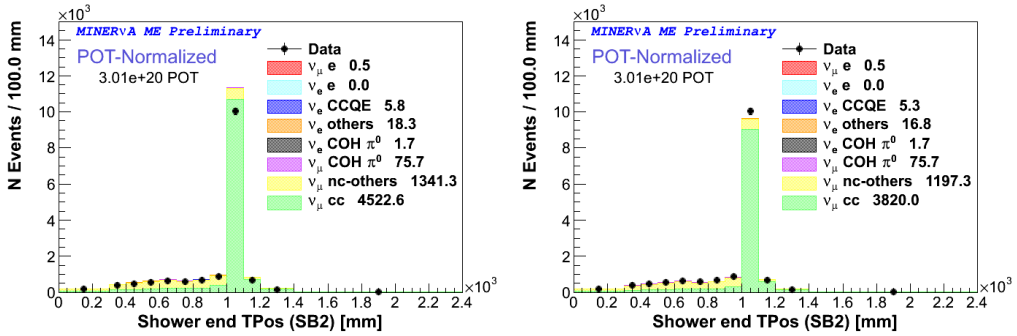

Figure 6.8: Transversal end position of the track for sideband 2. Left: before tuning. Right: after tuning.

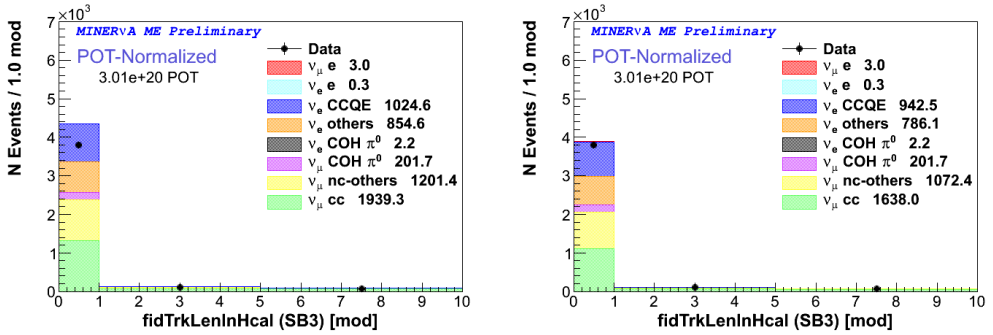

Figure 6.9: Fiducial track longitud inside of HCal Detector for sideband 3. Left: before tuning. Right: after tuning.

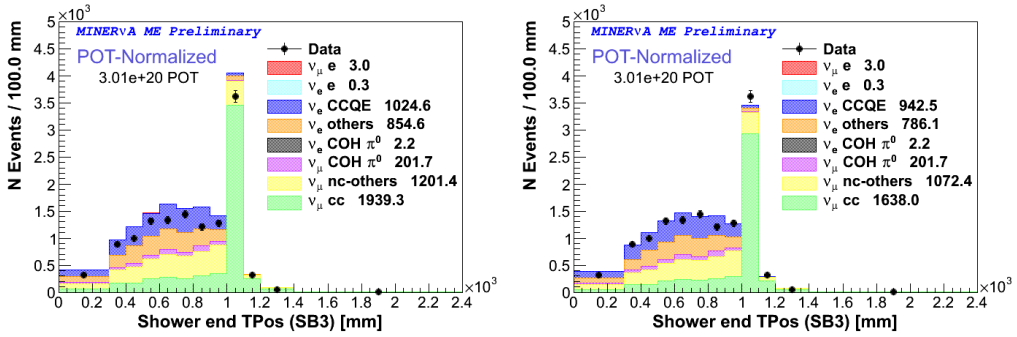

Figure 6.10: Track transversal end position in sideband 3. Left: before tuning. Right: after tuning.

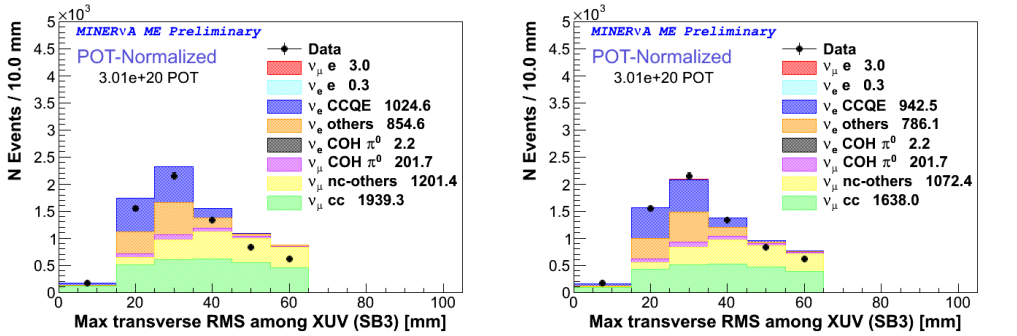

Figure 6.11: Transversal size of the electromagnetic shower for sideband 3. Left: before tuning. Right: after tuning.

Parameters	Tune Value
ν_e	0.920 ± 0.029
ν_μNC	0.893 ± 0.019
ν_μCC	0.845 ± 0.009

Tabla 6.1: Tune/normalization parameters obtained after match Data and MC in the sideband region using 7 distributions.

The normalization tuned parameters are shown on the Table 6.1.

After the extracting the normalization parameters from sideband tuning and applying those making and extrapolation over the signal region, the final Electron Energy spectrum is shown in the Figure 6.12.

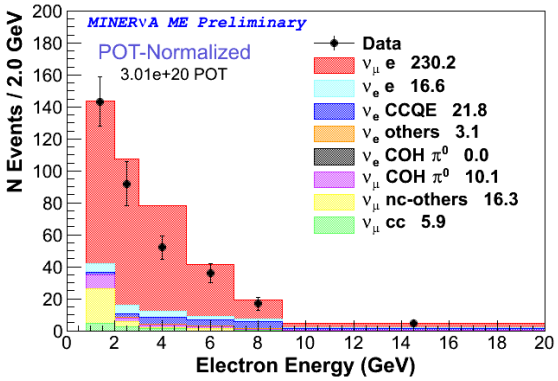

Figure 6.12: Final Electron Energy distribution after sideband tuning.

6.3 Multi-Universe Method

The systematic uncertainties are evaluated on this analysis using the called "multi-universe" method. In this method, each "universe" is a single scenario that incorporates systematic uncertainties on the models of the neutrino flux, MINERνA Detector and underlying reaction cross-sections.

A reweighting of a single Monte Carlo simulation sample is used to simulate each of these universes.

The name multi-universes refers to the creation of a statical ensemble of such individual randomly generated universes. The measurement is repeated in each individual universe and the statistical variation of the measurements is

used to evaluate systematic uncertainties.

The systematic uncertainties are classified as either the uncertainty in the background prediction or the uncertainty in the detector efficiency and acceptance. There are many individual systematic uncertainties that are evaluated. For convenience and clarity of presentation, the largest uncertainties are combined into broad categories.

6.3.1 Energy Scale Uncertainty

The largest uncertainty in the background prediction comes from the background cross section models, although they are signficantly reduced by the sideband tuning procedure, due to the extrapolation of the scale background tuned to the signal region. The uncertainty in the electron energy scale is 1.2%, it was determined by comparing the agreement between data and Monte Carlo for the Michel Electron candidates.

The applicability of this energy scale across a wide array of energies and for electromagnetic showers ideally should be confirmed using samples of $\pi^0 \to \gamma\gamma$ decays and Michel electrons from $\mu^{\pm} \to e\nu\nu$ decays of muons stopping in the detector, as well as in test beam measurements using a smaller version of the MINERνA Detector [40].

It is said ideally because in Low Energy this was the followed process, but due to that in Medium Energy this was the first analysis, it was just used the Michel Electron information. The Michel Electrons analysis in Medium Energy is shown in the Appendix section.

6.3.2 Angle Uncertainty

The 1 mrad of uncertainty in the neutrino beam angle direction with respect to the detector axis is determined by comparing the data and simulation for high energy ν_μ Charged Current events that have very low hadronic energy.

The neutrino beam angle direction was determined using the Charged Current Inclusive Data and MC samples for Medium Energy. Based on that study, a correction of 3 mrad is made on the angle in the vertical and 1 mrad for the horizontal direction.

The process to determine the neutrino beam angle direction is described on the Appendix section.

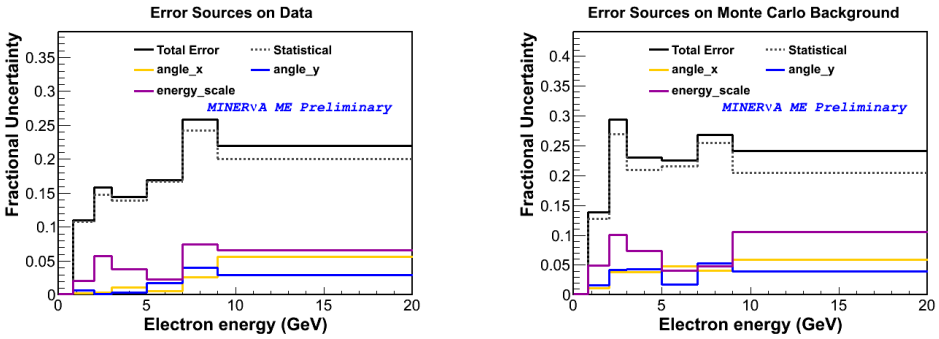

Figure 6.13: Fractional systematic uncertainties on Data and Monte Carlo background as a function of the Electron Energy after tuned background.

On the Figure 6.13 the systematics for Data and predicted background are shown.

The Figure 6.14 shows the angular and energy scale systematics in data after the background subtraction.

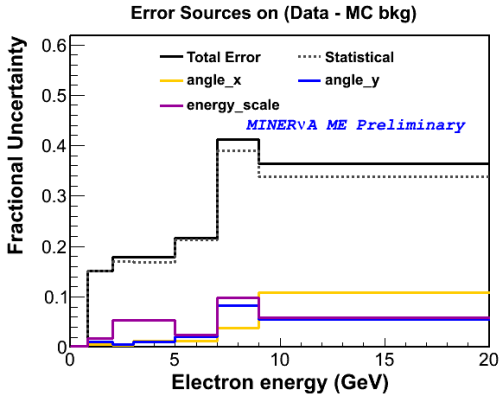

Figure 6.14: Fractional systematic uncertainties on Data after background subtraction and sideband tuning as function of the Electron Energy.

6.3.3 Flux Uncertainty

All systematic uncertainties on neutrino interactions are simulated within GENIE by varying individual parameters, but in the final evaluations, these uncertainties are combined into a single GENIE parameter systematic [42].

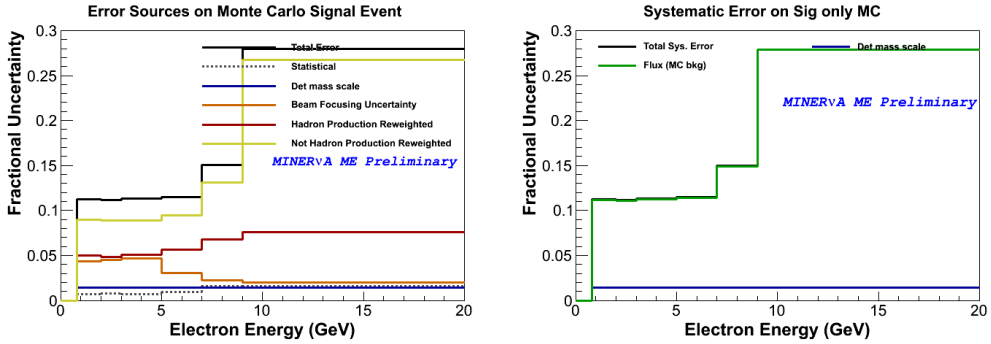

Figure 6.15: Flux uncertainties for signal prediction after tuned background. Left: individual flux uncertainty contribution. Right: grouped flux uncertainties.

There are also large uncertainties associated with the flux of neutrinos on the detector. These are grouped into three categories. Focusing uncertainties, NA49 hadron production uncertainties and Tertiary beam uncertainties.

The Focusing uncertainties are uncertainties associated with the beam optics. This includes uncertainties from alignment of two horns, uncertainties in the horn current, and uncertainties on the current distribution within the horn [31, 42].

As it was explained before on the Simulation Chapter, the MINERνA Experiment uses data from the NA49 hadron production experiment that measures pion and kaon rates produced from interactions of protons on thin carbon targets. If the neutrinos come from such measured interactions, the rate is given by the NA49 measurements and the uncertainties of that data are used as an uncertainty in the flux.

Approximately 60% of neutrinos are produced by processes that use this data to constrain the flux, these uncertainties are known as NA49 uncertainties.

The primary reactions not constrained by this data are reactions where there are multiple interactions in the target or in other material such as horns and the decay pipes that create the particles that decay into neutrinos.

It is used the term Tertiary to cover the uncertainties on such processes since the most common case of such reactions is production of secondary particles in interactions of primary protons in the carbon target, which then result in a

tertiary meson that decays into neutrinos.

The flux uncertainties are incorporated by varying the parameters associated with hadron production and beam focusing in the flux model. The non-CCQE interaction model uncertainties are incorporated by varying the underlying parameters in the cross section models for processes such as resonance production and coherent scattering.

The Figure 6.15 shows the uncertainties asociated with the flux.

To corroborate the systematic uncertainties in the multi-universe method, again the sideband tuning was performed on each universe. This provides a way to measure how systematic uncertainties are reduced by the data constraint in the sideband tuning [42].

A simplest example of an uncertainty that is expected to vanish in sideband tuning is the normalization uncertainty, such as one due to uncertainty in the scintillator mass in the detector. If the Monte Carlo normalization is different than reality, the sideband tuning will alter the Monte Carlo normalization to match the data.

The flux uncertainties, although they do have some variation with neutrino energy, have an overall uncertainty independent of energy as their primary effect. Therefore, much of the flux uncertainty will be reduced by sideband tuning. In the Figure 6.16 it is possible to see the reduction effect from the flux before and after tuned the background.

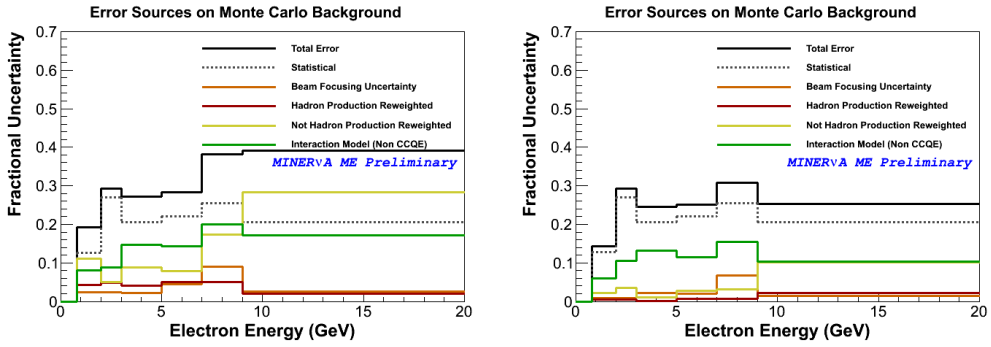

Figure 6.16: Flux uncertainties just for background prediction as function of Electron Energy. Left: before tuned background. Right: after tuned background.

6.3.4 The Q^2 Shape Correction

The most important systematic uncertainty for electron energies below 7 GeV comes from the fact that the ν_e CCQE cross section shape as a function of Q^2 is not known precisely, and for those electron energies the background at low Q^2 must be extrapolated using events at high $E\theta^2$, which are also at high Q^2.

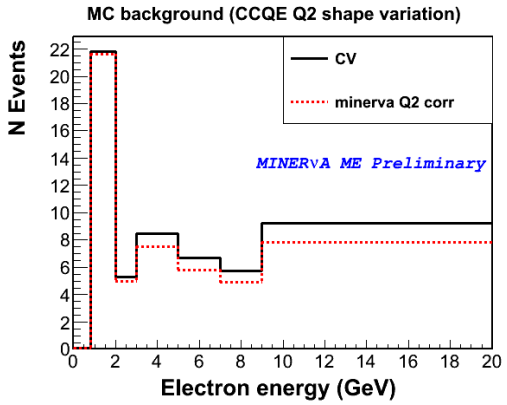

Figure 6.17: The Q^2 shape variation in Medium Energy.

The MINERνA Experiment measured a different cross section shape versus Q^2 than what is in the standard GENIE neutrino event generator, on this case the systematic is evaluated by taking the difference between the shape of the MINERνA measured cross section as a function of the Q^2 and the one predicted by GENIE.

At higher electron energies this uncertainty no longer dominates and the flux and the electron energy scale becomes the largest unertainties.

6.3.5 Reconstruction Efficiency Uncertainty

The reconstruction efficiency uncertainty is determined by assuming that the reconstruction efficiency uncertainty for electrons is the same as it is for muons, since both particles tracks are seeded using the same technique.

The reconstruction efficiency uncertainty for muons is determined by comparing the data and simulation for the efficiency of matching a muon track in the MINERνA Detector once a track is found in the MINOS Detector that extrapolates into MINERνA. The discrepancy between data and simulation is treated as the systematic uncertainty.

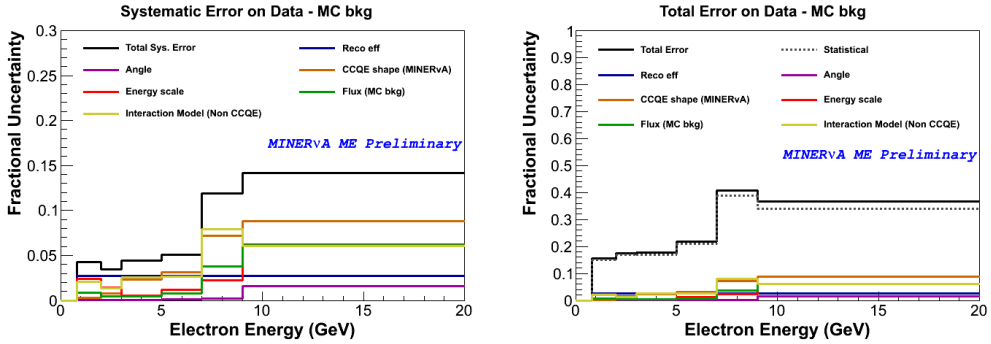

Figure 6.18: Final fractional systematic uncertainties as a function of the electron energy, after applying all cuts, sideband tuning and background subtraction.

The systematic uncertainty, shown in Figure 6.18, is evaluated by randomly changing the underlying simulation prediction according to the various uncertainties, refitting the background scale factors, and then subtracting the background, extracting the electron energy spectrum, and correcting for detector acceptance.

6.4 Background Subtraction

The utility of the Monte Carlo simulation is to predict the signal and background distributions, with it, it is easy to apply cuts and identify the background composition.

The next steps in the signal selection and the sideband tuning is to measure the real Neutrino Electron Scattering events into the final sample. To do this, it is necesary to subtract the predicted background on data and Monte Carlo.

In the background subtraction process, it is used the remaining predicted background after applying all the cuts, if the subtraction to the Monte Carlo is made, then it is conserved only the Neutrino Electron Scattering events, and so due to that the Monte Carlo is a prediction of the Nature via Physics Models then it is subtracted the background content of the Data.

The background subtraction is made bin by bin. In the Figure 6.19 is shown the predicted signal and background, from where it is subtracted it bin by bin on data and Monte Carlo at the same time.

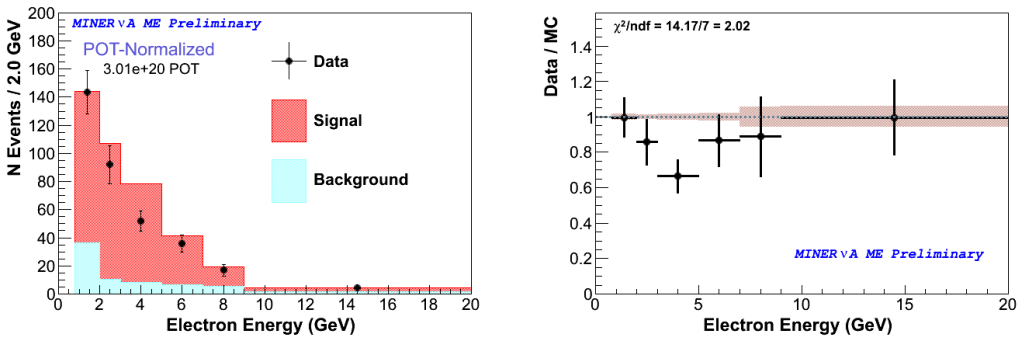

Figure 6.19: Right: Electron Energy after all cuts, all the background process are considered as only one background. Left: Ratio between Data and Monte Carlo prediction after sideband tuning.

Figure 6.20 shows the Electron Energy after the background subtraction on data and Monte Carlo.

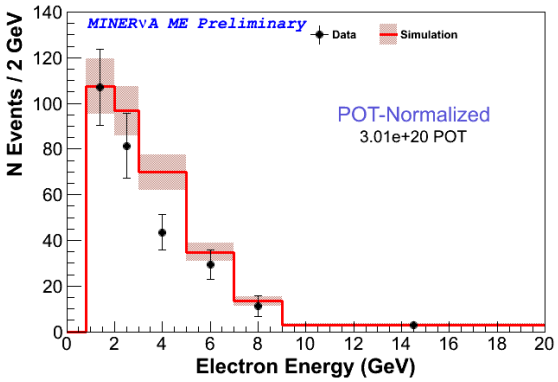

Figure 6.20: Electron Energy after background subtraction procedure. The agreement remains after the subtraction.

6.5 Efficiency Studies

As it was explained before, the Neutrino Electron Scattering process has very low rate, almost $\sim 1/2000$ of the cross section for neutrino-nucleus interaction, so it is mandatory not wast signal events, then it is requiered to use high efficience cuts to keep all the $\nu - e$ events.

The final data sample used in this thesis is composed by 4 playlists, on this case to study the efficiency is needed a high statistics sample, but due to the low probability of the neutrino electron elastic interaction, then 4 high statistics samples were generated just for our interaction channel.

The sizes of each high statistics signal sample are on the Table 4.1, each size is almost 300 times the data sample. The efficiencies in each playlist are shown on the Figure 6.21.

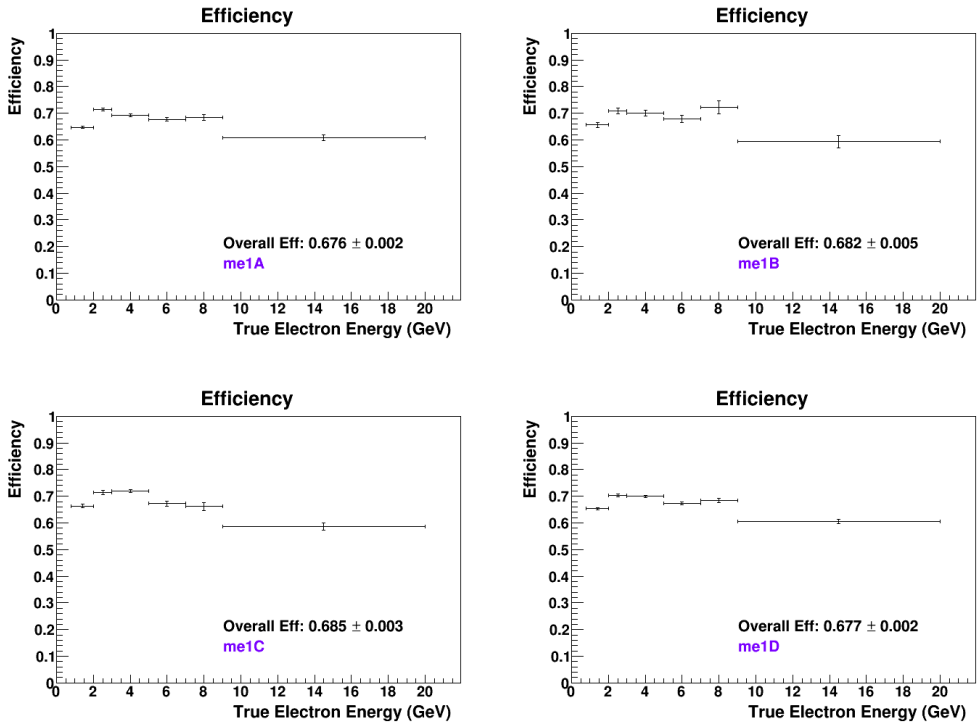

Figure 6.21: Efficiency as function of the True Electron Energy for each one of the playlists.

The final efficiency for the entire high statistics signal sample was calculated via the Equation 6.2, there, it is used the POT size from each sample as a weight.

$$\epsilon_{all} = \frac{POT_{me1A}\epsilon_{me1A} + POT_{me1B}\epsilon_{me1B} + POT_{me1C}\epsilon_{me1C} + POT_{me1D}\epsilon_{me1D}}{POT_{me1A} + POT_{me1B} + POT_{me1C} + POT_{me1D}}. \tag{6.2}$$

The Figure 6.22 shows the efficiency for each one of the single cuts. The scheme of 21 cuts are on the Appendix Section. Almost all the cut have an

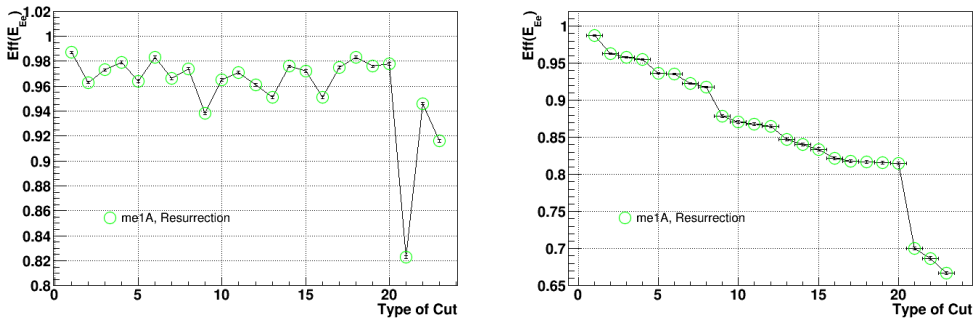

Figure 6.22: Left: Single cut efficiency, almost all the efficiencies are over 90%, including the main signal isolator cut ($E\theta^2$). Right: accumulative Efficiency. The final efficiency is $\sim 67\%$.

efficiency greater than 95%, except for the cuts: Peak in ECal and Q^2, both have an efficiency around of 94%; the most strong cuts are dE/dx and $E\theta^2$ that have an efficiency of $\sim 86\%$ and $\sim 92\%$ respectively.

On the Figure 6.22, the accumulative efficiency is shown, so it means, that is the efficiency after applying the previous cuts. The efficiency goes down by accumulative cuts, but it still remain high ($\sim 80\%$) after applying the first 20 cuts.

When the dE/dx_{1-4} cut is applied, the efficiency drops until $\sim 71\%$ and after applying all the cuts, the final efficiency is $\sim 68\%$.

The Figure 6.23 shows the efficiency as function of the True Electron Energy, it is seen how it looks almost flat for the range [0.8, 9.0] GeV, and fall a litle bit for high energies; 9 to 20 GeV.

6.5.1 Efficiency Correction

After background subtraction on data and Monte Carlo, the next step is to apply the efficiency correction, this means, apply the efficiency of the cuts as function of true electron energy over final reconstructed electron energy.

The goal of the efficiency correction is to predict the real number of neutrino electron scattering events before applying the selection cuts. Figure 6.24 shows the electron energy after applying the efficiency correction, the data and the Monte Carlo prediction agree.

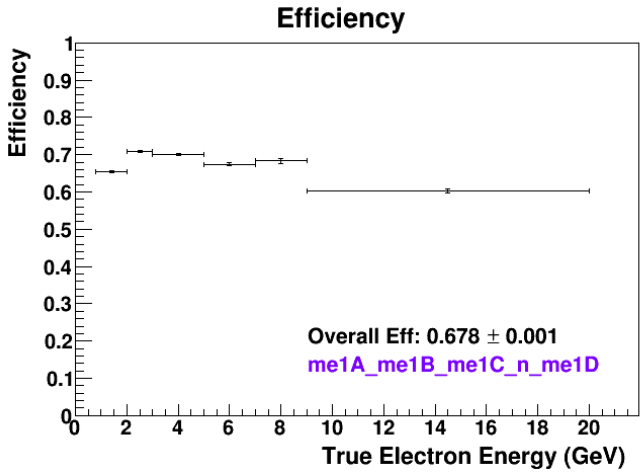

Figure 6.23: Overall Efficiency as function of the True Electron Energy.

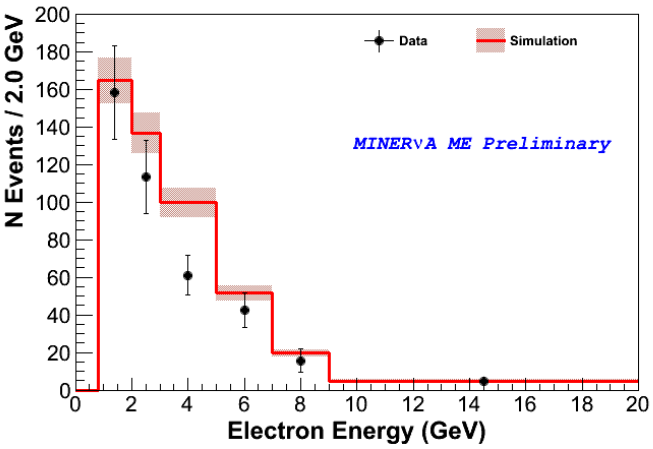

Figure 6.24: Electron energy after sideband tuning, background subtraction and efficiency correction.

Chapter 7

Flux Constraint for MINERνA Medium Energy

The Electron Energy spectrum may be like a tool to constrain the overall normalization and shape of the neutrino flux.

This can be accomplished by noting that Bayes Theorem, that relates the probability of a particular flux model (M) given an observed electron spectrum ($N_{\nu e \to \nu e}$) to the a priori model and the probability of the data given by the model

$$P(M|N_{\nu e \to \nu e}) \propto P(M)P(N_{\nu e \to \nu e}|M), \tag{7.1}$$

assuming a Gaussian approximation of the Poisson distributed data, the probability of the data spectrum given by the model is proportional to

$$P(N_{\nu e \to \nu e}|M) \propto e^{-x_M^2}, \tag{7.2}$$

here χ^2 is the chi-square statistic comparing the observed Electron Energy distribution to that predicted by model M. For this procedure it is assumed that the experiment has a valid probability distribution for its a priori flux prediction, and that the probability to see at least the difference between the mean prediction and the actual measurement is not negligibly small.

The Figure 7.1 shows the probability distribution for the number of Neutrino Electron Scattering events predicted, and it is obtained making random variations in the parameters of the simulation.

The combined randomly variations on flux parameter are shown in the Figure 7.2. The probability distribution (black) of the predicted number of Neutrino Electron Scattering events in the simulation provides errors in the neutrino flux model and the modified probability distribution (red) given the observed

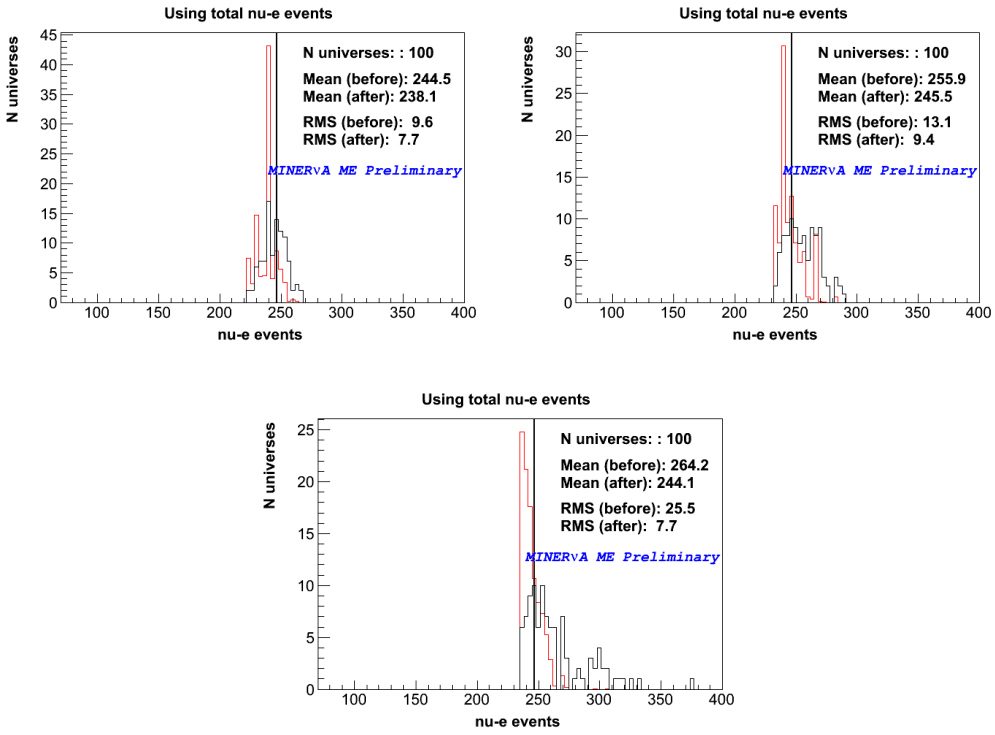

Figure 7.1: Number of $\nu e \rightarrow \nu e$ predicted events obtained from randomly varying flux parameters. From left to right variations on Flux Focusing, Flux NA49 and Flux Tertiary.

electron energy spectrum.

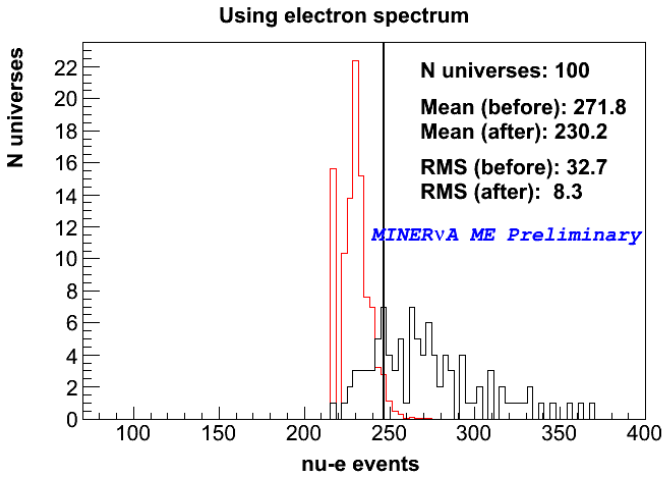

Figure 7.2: Probability distribution (back) of the predicted $\nu e \to \nu e$ events and the probability distribution (red) for the observed Electron Energy spectrum.

The probability distribution showed on Figure 7.2, gives the observed Neutrino Electron Scattering spectrum, that was constructed by weighting the entry corresponding to a given universe by $e^{\chi_i^2}$. Where the exponent tell us the difference between the predicted Neutrino Electron Scattering energy spectrum in the universe i and that observed in the data, i.e. this is an approximation of the likelihood method.

At the same Figure 7.2 the mean of the second, "constrained", distribution is 14.7% lower than the original distribution, and the RMS is reduced by 74%.

The same weights applied to produce this distribution can be used to constrain any other prediction that is calculable by the simulation, for example the flux distribution.

In few words, the constraint method uses two sets of probabilities: Total number of events in all bins and the number of events in each individual bins (spectrum). Then each universe gets a weight equal to its probability, the weights are normalized to conserve number of universes.

To use the constrain method, to get the constrained value of some quantity, it will be plotted in the universes applying the weights. Then the new mean and width of histogram gives the constrained value and uncertainty.

Te main idea of the flux constrain method is described in the Figure 7.3.

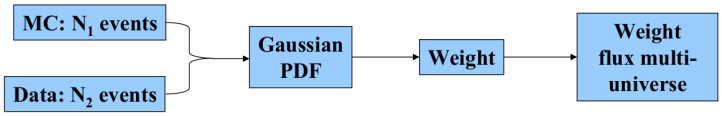

Figure 7.3: Flux Constrain Method representation.

Then the new flux prediction, that includes the constraint from Neutrino Electron Scattering, i.e. the original flux distribution weighted by the mean from the probabilities distributions is shown on Figure 7.5.

This measurement (new flux prediction) can be used by other experiments operating in the NuMI beam which use a similar multi-universe method of propagating neutrino flux uncertainties and that are able to produce a predicted number of Neutrino Electron Scattering events with an electron enegy above 0.6 GeV in the fiducial mass and location given each of their simulated universes [53].

The effect of the new flux prediction over the Electron Energy espectrum for Neutrino Electon Scattering can be seen in the Figure 7.4.

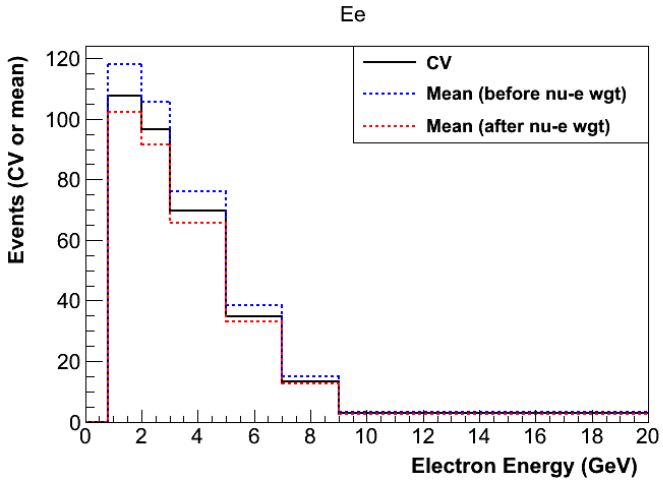

Figure 7.4: The Electron Energy distributions for the $\nu e \rightarrow \nu e$ events before and after the flux constrain.

An the ratio between the Electron Energy distributions after and before the flux constrain have been applied, is in the Figure 7.5.

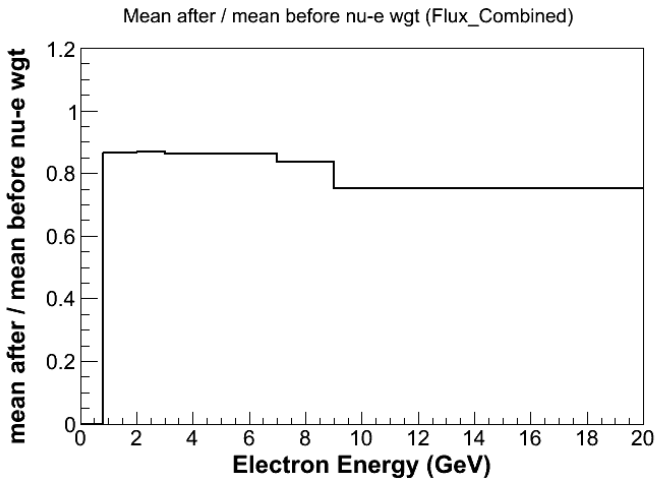

Figure 7.5: Ratio of the Electron Energy after and before the flux constrain.

Chapter 8

Results

8.1 Data and Monte Carlo

The energy spectrum for the outgoing electron coming from the Neutrino Electron Elastic Scattering is shown on the Figure 8.1, this plot is after the Sideband tuning, i.e, after tuned background prediction was done. At this point there is the signal events with a tuned background.

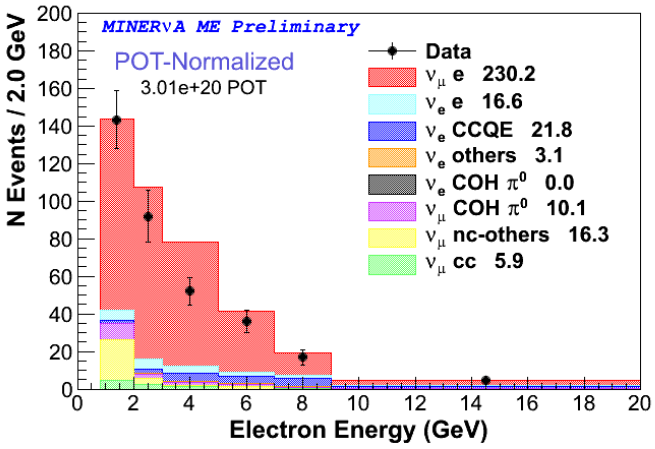

Figure 8.1: Neutrino Electron Elastic Scattered energy spectrum, after sideband tuning.

The comparison between the measured and the prediction for Electron Energy spectrum is shown in the Figure 8.2.

Since the Neutrino Electron Scattering cross section has not a significant uncertainty, then the uncertainty on the predicted energy spectrum comes di-

rectly from the prediction of the neutrino flux [42].

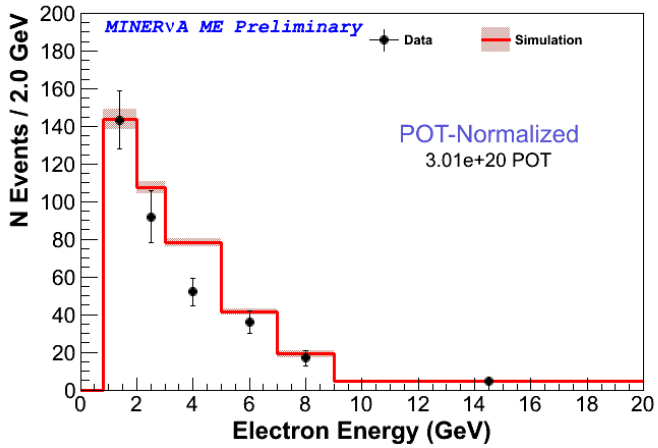

Figure 8.2: Monte Carlo electron energy error band after sideband tuning. There is a good agreement between Data and Simulation.

As it was mentioned on the Sideband Tuning Section, it will be a good tuning if the desagreement between Data and Monte Carlo comes from an incomplete or wrong modeling, therefore the background tuning compensates the mismodeling on Neutrino Electron Scattering. The small disagreement between Data and Monte Carlo on the Figure 8.2, would therefore be an indication of an incorrect neutrino flux prediction.

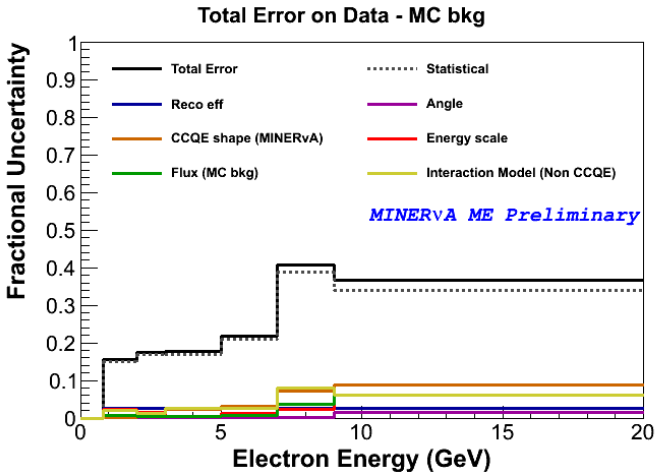

Figure 8.3: Total uncertainties on Data as function of Electron Energy, after background subtraction and tuned.

Sources	Events	Fraction [%]
Flux (MC-Bkg)	1.1	0.56
GENIE (non-CCQE)	4.3	2.12
CCQE	4.6	2.23
Beam Angle	0.4	0.17
Energy Scale	4.0	1.91
Reco Eff	5.5	2.73
Total	9.3	4.57

Tabla 8.1: Final systematics uncertainties contribution sources.

The uncertainties in the Neutrino Electron Scattering has different sources, as it was explanied in the previous sections. The Figure 8.3 shows the uncertainties on data after the backgroun subtraction, on such plot the uncertainties on angle "x" and "y" were grouped just as one uncertainty. The same procedure was followed for the flux uncertainties.

The Fractional systematics uncertainties after the background subtraction and sideband tuning is shown in the Table 8.1.

The measured and predicted number of Neutrino Electron Scattering events in the sample, performed by predicted background subtraction from the sample, and correcting it for the signal efficiency is in the Figure 9.2, this is the final resulting Electron Energy spectrum.

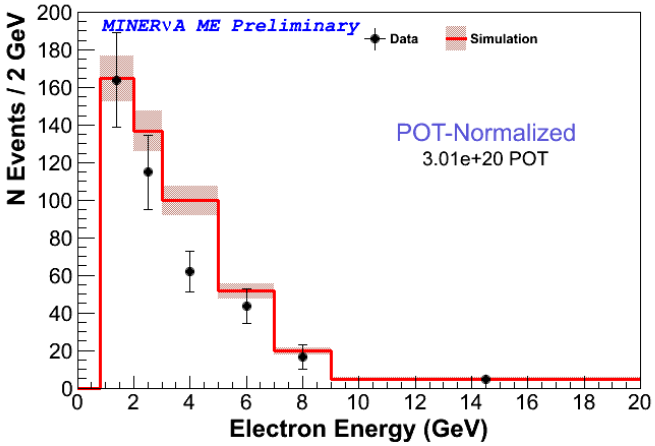

Figure 8.4: Electron Energy after sideband tuning, background subtraction and efficiency correction.

	Events	± Statistics	± Systematics	TOTAL
Data	262.000	16.186		
MC_{Bkg}	57.295	4.553	0.077	
Bkg Subtracted				
Data - MC_{Bkg}	204.705	16.815	9.329	± 19.229
	204.705	8.21 %	4.55 %	± 9.39 %
Aft Eff Corr				
$\nu e \rightarrow \nu e$	303.917	25.125	14.076	± 28.799

Tabla 8.2: Final results with uncertainties, before and after the background subtraction. All the results come after tuned background.

The comparison of the Electron Energy spectrum before and after the efficiency correction is shown in the Figure 8.5.

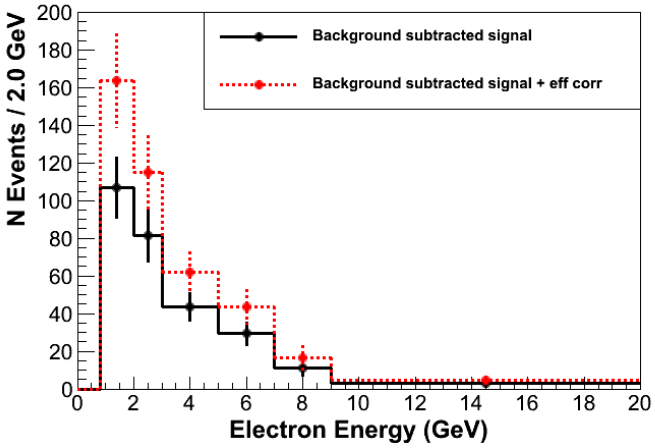

Figure 8.5: Comparison of the electron energy before and after sideband tuning, background subtraction and efficiency correction.

The total rate of $\nu e \rightarrow \nu e$ scattering events in the fiducial volume, estimated from the measured Neutrino Electron Scattering events, i.e, after background subtraction and after sideband tuning, are in the Table 8.2, the results come before and after efficiency correction.

Chapter 9

Conclusions

To detect the elusive neturinos is necesary to run for a long time an intense neutrino beam interacting with a massive detector. Up the moment, in the first two years in the Medium Energy Forward Horn Current configuration, the MINERνA Experiment have taken $\approx 6 \times 10^{12}$ POT, but the data used on this thesis is just $\sim 1/2$, i.e., just 1 year of data.

Neutrino Electron Scattering may be the most rare process in the MINERνA Experiment, due to the small cross section, this is $\sim 1/2000$ compared with the cross section of the neutrino nucleus scattering. The Neutrino Electron Scattering has an appearance rate of 1 event every 30hrs in the Medium Energy forward beam configuration.

Unfortunately, some νe candidate events are rejected by the dE/dx, this is the more strong cut on this analysis, due to the electron - photon overlapping.

The results obtained on this thesis provide a measurement of the rate of Neutrino Electron Scattering events, which is in good agreement with the flux pediction, and has comparable precision to the prediction.

As it was predicted, on the electron energy distribution the ν_μ dominates the flux, it can seen on the Figure 9.1.

The Neutrino Electron Scattering prediction has an stronger contraint on the high energy neutrino flux at lower energies, that is because the particles focused from the proton-graphite interaction are more energetic, this means, the pions and kaons travel more distance before decaying into neutrinos, it maybe gives a different beam angle.

It can be seen in the Figure 8.2 how each bin has large uncertainties, on this

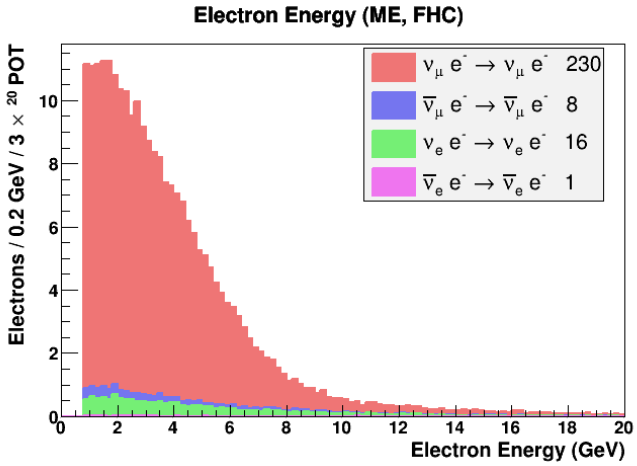

Figure 9.1: The Neutrino Electron Scattering energy spectrum. This plot is coming directly from the GENIE sample.

case, the ability of this result to contraint the neutrino flux as a function of the energy is marginal.

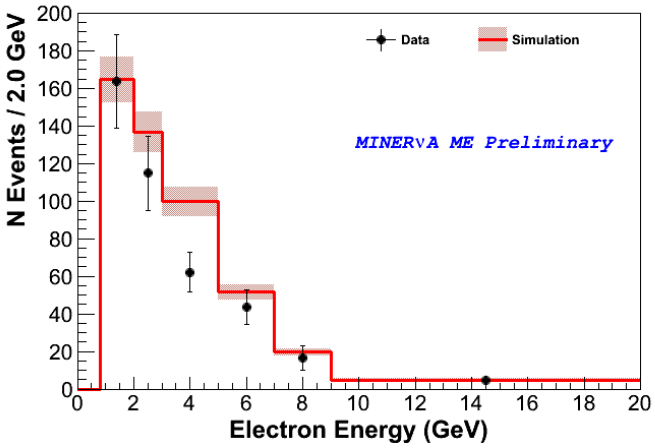

Figure 9.2: Electron Energy after sideband tuning, background subtraction and efficiency correction.

There is a barely significant indication that the rate of events observed below 3 GeV electron energy is less the nominal flux predicted. This indicates that there is slightly less flux at lower neutrino energies, but again, the observation is not significant [42].

Due to main trace of the Neutrino Electron Elastic Scattering is very for-

ward electron, the well understood process and the low uncertainty, the method described on the present thesis, can be used as a cheaper and no invasive way to contraint the neutrino flux on the actual and future neutrino oscilation experiments.

This measurement is an important proof of this technique that could be used for a future long baseline experiment, such as the DUNE Experiment.

This process involves scattering off electrons rather than nuclei, and provides a precise flux prediction, given any near detector technology with sufficient angular resolution, energy reconstruction and mass to isolate statistically a significant sample of these events.

Chapter 10

Perspectives

10.1 Full Medium Energy

The MINERνA Experiment will continue operating in the medium energy (ME) run at last for 2 years more. Neutrino beam peak energies of LE and ME are about 3.5 and 6.5 GeV, respectively, as shown in Figure 3.1.

For the full Medium Energy, it is expected to have a significant neutrino electron elastic scatering sample, because the neutrino-electron total cross section is proportional to the neutrino energy and because the expected number of protons on target should be $10 \times 10^{20} POT$, this is 3 times the size of the exposure used in this analysis. And 3 times the Low Energy sample.

An important part of the machinery developed for this analysis is the tuning of backgrounds on data using sideband samples. This suggests that uncertainties on the backgrounds will decrease with increased statistics. Our preliminary Monte Carlo simulation studies suggest that the signal-to-background ratio remain similar to the Low Energy studies.

For the full ME sample, it is expected to have approximately 1100 signal and 300 background events [42]. That should provide a flux integrated constraint with $3-4\%$ uncertainty, which is much smaller than the uncertainty of the flux prediction itself.

10.2 Medium Energy vs Low Energy

The Low Energy Forward beam configuration sample is almost the same size of the data sample used on this thesis, with the actual beam configuration it has

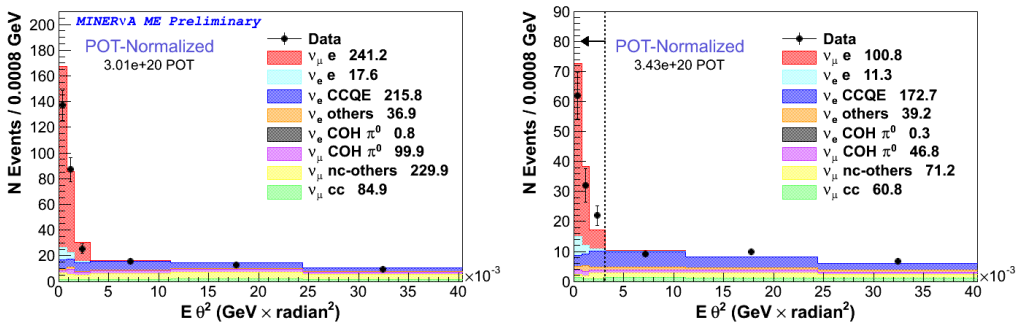

Figure 10.1: The golden plot for Neutrino Electron Scattering - the kinematic contraint- $E\theta^2$. Left: Medium Energy result. Right: Low Energy result.

been measured almost three times the number of Neutrino Electron Scatering candidate events.

The physical explanation for this result is due to that the Neutrino Electron scattering cross section has energy dependence, so the cross section increases slightly with the neutrino energy.

The Neutrino Electron Scattering analysis in Medium Energy was done using almost the same machinery developed for Low Energy analysis. Due to experimental lack of ability to distinguish between neutrino flavors, all the neutrino flavors where included as one neutrino type.

The difference in magnitude of cross section for the different neutrinos flavors interacting elastically with electrons, in both analysis (LE and ME) have not been taked into account, it is considered that such effect is low due to the main composition of the neutrino beam in ME and LE is $\sim 94\%$ of the ν_μ.

On the next Figures 10.1 and 10.2, are shown the $E\theta^2$ and Electron Energy distributions from the Low Energy [44] and Medium Energy analysis, both are after sideband tuning.

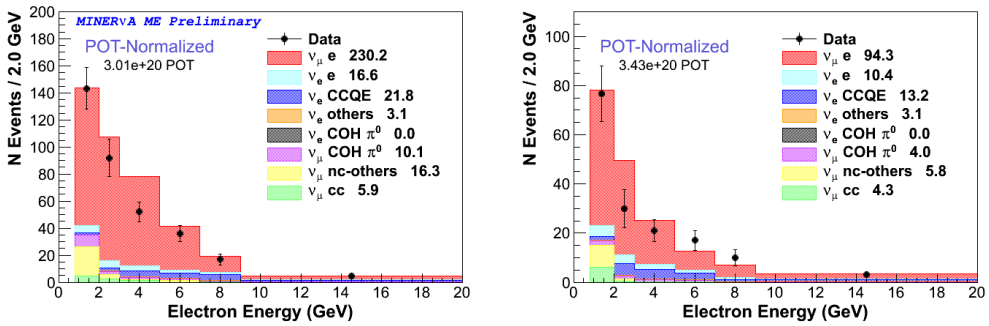

Figure 10.2: Electron Energy spectrum for Neutrino Electron Scattering after sideband tuning. Left: Medium Energy run. Right: Low Energy run.

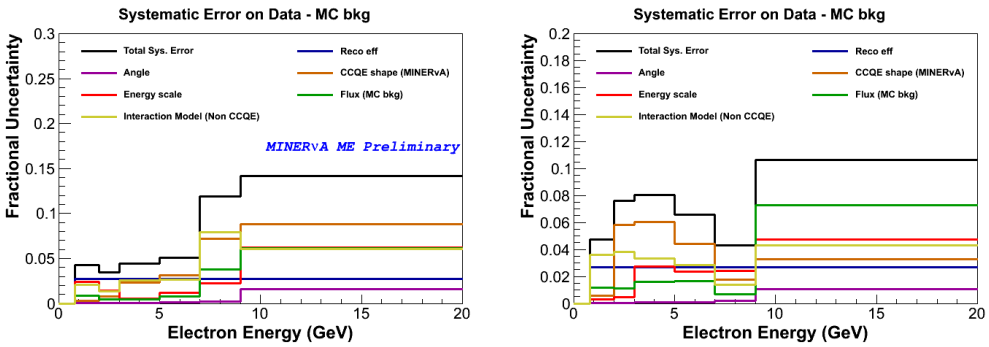

Figure 10.3: Final systematics uncertainties on data after background subtraction, as function of Electron Energy. Left: Medium Energy analysis. Right: Low Energy analysis.

Appendix A

Units and Notation

It is used the natural units

$$h = c = 1 \tag{A.1}$$

It is noted that

$$[h] = ML^2T = 6.582 \times 10^{-22} MeV - s \tag{A.2}$$

$$[c] = LT^{-1} = 3 \times 10^{10} cm/s \tag{A.3}$$

$$[hc] = 197 \times 10^{-13} MeV - cm \tag{A.4}$$

If $h = c = 1$, then

$$v = \frac{c^2 p}{E} = \frac{p(MeV/c)}{E(MeV/c^2)} (\text{in c units}). \tag{A.5}$$

With $M = 1$ GeV,

$$L \sim \frac{1}{GeV} = \frac{hc}{1000 MeV} \approx 2 \times 10^{-14} cm \tag{A.6}$$

$$T \sim \frac{1}{GeV} = \frac{h}{1000 MeV} \approx 6.58 \times 10^{-25} s \tag{A.7}$$

$$1 MeV = 1.6 \times^{-6} erg = 1.6 \times^{-13} J \tag{A.8}$$

$$1 gm = 5.61 \times^{23} GeV \tag{A.9}$$

The position is indicated by a 4-vector $x(\mu = 0, 1, 2, 3)$:

$$x^\mu = (ct, \mathbf{x}) = (t, \mathbf{x}) \tag{A.10}$$

$$x_\mu = (ct, -\mathbf{x}) = (t, -\mathbf{x}) = g_{\mu\nu} x^\nu \tag{A.11}$$

$$x^2 = x_\mu x^\mu = t^2 - \mathbf{x}^2 = 0 \tag{A.12}$$

with $g_{\mu\nu} = 0$, $\mu \neq \nu$, $g_{00} = 1$, $g_{22} = g_{33} = -1$. On the light cone

$$x^2 = 0 \Rightarrow t^2 - \mathbf{x}^2 = 0 \tag{A.13}$$

The energy E and momentum $\mathbf{p}$ are represented by 4-vector p:

$$p^\mu = (E/c, \mathbf{p}) = (E, \mathbf{p}) \tag{A.14}$$

$$\partial_\mu = \frac{\partial}{\partial x^\mu} \approx (\frac{\partial}{\partial t}, \nabla) \tag{A.15}$$

$$\partial^\mu = \frac{\partial}{\partial x_\mu} \approx (\frac{\partial}{\partial t}, -\nabla) \tag{A.16}$$

$$\partial^\mu \partial_\mu = \frac{\partial^2}{\partial t^2} - \nabla = \Box^2 \tag{A.17}$$

$$p^2 = p_\mu p^\mu = p_0^2 - \mathbf{p}^2 = E^2 - \mathbf{p}^2 \tag{A.18}$$

For a particle on the mass shell

$$E^2 = \mathbf{p}^2 + m^2 \tag{A.19}$$

i.e.,

$$p^2 = p_\mu p^\mu = m^2 \tag{A.20}$$

The scalar product

$$pq = p^\mu q_\mu = E_p E_q - \mathbf{p} \cdot \mathbf{q} \tag{A.21}$$

Appendix B

Electromagnetic Showers

One of the physical process that play a role in particle detection is the electromagnetic shower development, this is well understood.

On the media electrons and positrons lose energy via two mechanism: ionization and radiation. Each one has its action range, the first process dominates at low energy, the second one at high energy.

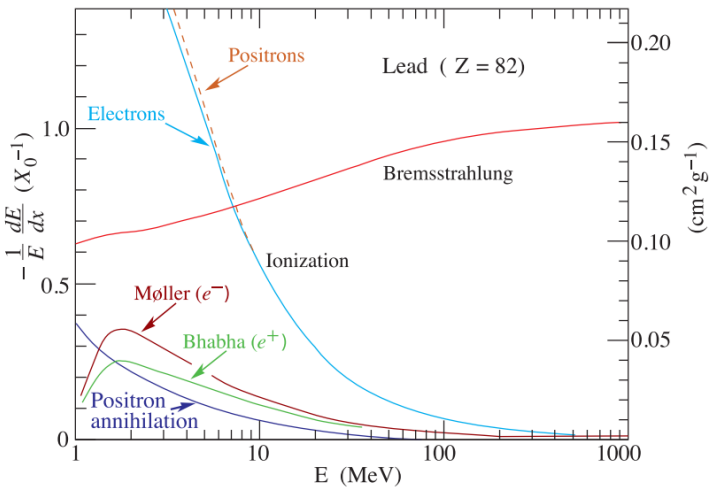

Figure B.1: Fractional energy loss in Lead as a funtion or positron energy [7].

The energy loss of charged particles from ionization, often referred as dE/dx, is an excellent particle identifying discriminant for particles that passes through material. Not only is this energy loss the effect of many small interactions, typically ionizing thousands of atoms per gram/cm^2, and therefore less subject to stochastic fluctuation, it also depends strongly on momentum as the particle slows down from ultra-relativistic and therefore the pattern of dE/dx as the

particle stops is sensitive to its mass.

From the Figure B.1, it is seen the interacting mechanism of the photons, these interact either through the Photoelectric Effect, Compton Scattering or Pair Production.

Other plot that describes the energy loss mechaninism is the Figure B.2. There the photoelectric effect dominates at low energies, pair production at high energies. The relative cross sections are also Z dependent.

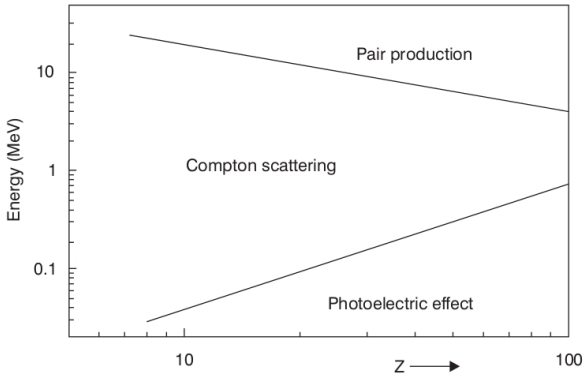

Figure B.2: Charged particle energy loss process: photoelectric effect, Compton scattering and pair production, as a function of the number Z of the absorber-material [46].

The angular distribution is more or less isotropic for the photon and Compton electrons, but highly directional for the e^+e pairs produced in pair production. At energies of 1 GeV and higher, electrons and photons initiate electromagnetic showers in the materials they penetrate.

Electrons loses their energy predominantly by radiation, the most energetic photons produced in this process convert into e^+e pairs, which radiate more γs, etc.

The number of shower particles produced in this particle multiplication process reaches a maximum at a certain depth inside the absorber, and gradually decreases beyond that depth, see Figure B.3.

The depth of the shower maximum increases (logarithmically) with the energy of the incoming electron. Because of the particle multiplication, the total amount of material needed to contain electromagnetic showers is relatively

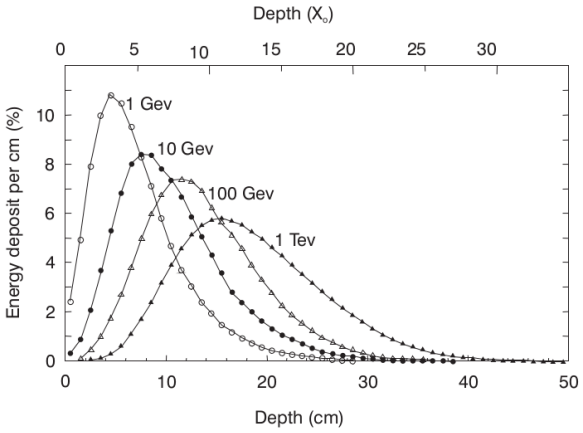

Figure B.3: The energy deposited as a function of depth for different electron enegies, the showers are developing in a block of copper [46].

small.

The lateral development of electromagnetic showers is governed by two types of processes:

- Electrons and positrons move away from the shower axis because of multiple scattering.

- Photons and electrons produced on isotropic processes (Compton scattering, photoelectric effect) move away from the shower axis.

The first process dominates in the early stages of the shower development, the second one is predominantly beyond the maximum shower. Both processes have their own characteristic, exponential scale.

The shower development can be described more or less independently of the details of the absorber material in terms of the radiation length (for the longitudinal development) and the Moliere radius (for the lateral development). Both units are defined for the asymptotic energy regime (> 1 GeV).

The radiation length (X_0) is the ratio of the electron energy and the specific energy loss by radiation. Therefore, a high-energy electron loses on average 63% ($1 - e^{-1}$) of its energy when it traverses $1X_0$ of material. The mean free path of a high-energy photon amounts to $9X_0/7$.

The Moliere radius (ρ_M) is defined through the ratio of the radiation length and the critical energy. Expressed in g/cm^2 , X_0 scales as A/Z^2 and $_M$ as A/Z.

Therefore, ρ_M is much less material dependent than X_0 [46].

The radiation length has a fundamental different meaning for electrons and photons. Therefore, showers initiated by high-energy electrons and by photons developed in the beginning quite differently. When they encounter material, high-energy electrons start to radiate immediately. On their way through a few mm of material, they may emit thousands of Bremsstrahlung photons. On the other hand, high-energy photons may or may not convert in the same amount of material.

In the latter case, they do not lose any energy, and when they convert early on, they may lose as much as, or even more than, electrons in the same amount of material. In the same amount of material, electrons lose on average a larger fraction of their energy than photons, but the spread in the energy losses by photons is larger.

The differences may be understood from the fact that the particle multiplication continues down to lower energies in high-Z material and decreases more slowly beyond the shower maximum. For example, a given high-energy electron produces 3 times more positrons when showering in Lead than in Aluminium.

As a result, it is needed more X_0 of Lead than of Aluminium to contain this shower at the 99% level. Also, the shower maximum is located at a greater depth in Lead. For 99% containment, the difference between high-Z and low-Z absorber materials may be as much as $10X_0$.

An electromagnetic shower has a characteristic longitudinal energy profile determined by the shower cascade processes. When electromagnetic particles such as electron, positron and photon traverse in a medium, carrying an energy > 1 GeV, they produce electromagnetic showers via successive Bremsstrahlung, $e^{\pm} \rightarrow e^{\pm}\gamma$e, and pair production, $\gamma \rightarrow e^{+}e^{-}$ in the fields of the atoms in the target [42].

The number of showering particles increases exponentially like a cascade until the energies of the particles drop below the energies where such multiplicative reactions dominate, this energy is called the Critical Energy, E_c .

The longitudinal energy deposition profile, which is proportional to the number of charged showering particles ($e^{\pm}$) at each point in the shower, follows the same pattern.

The Cascade Model is based upon the following restrictions [45]:

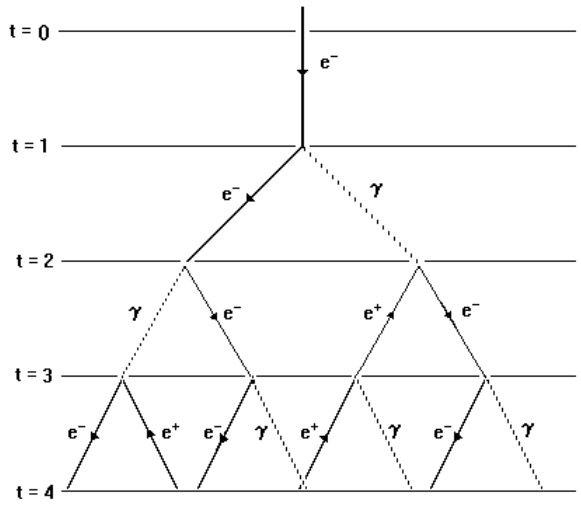

Figure B.4: Electromagnetic shower representation, via Cascade Model.

- The incoming charged particles has an Starting Energy E_0 that is much greater than the Critical Energy E_C, below it ionization losses predominate over pair production; $E_0 >> E_C$.

- Each electron with $E_0 > E_C$ travels one radiation lengths and then gives one half of its energy to a Bremsstrahlung photon.

- Each photon produced with energy $E > E_C$ travels one radiation length creates an electron-positron pair with each particle carrying away half the energy of the original photon.

- Electrons with $E < E_C$ cease to radiate and then lose the rest of their energy by collisions.

- At high energy the probabilities for Bremsstrahlung and pair production are assumed to be independent of Z (atomic number) when distances are measured in radiations length.

- The theoretical cross secctions are based on Born approximation and are most reliable for low Z materials. Deviations in large Z materials are proportional to Z^2.

- The difference in the cross section for high energy electron and positrons are neglected.

- The asymptotic formulas for radiation and pair production are asumed valid.
- The Compton effect and the collision process are neglected at high energy.

The model is schematically shown in the Figure B.4. The simple branching model suggest that after t radiation the shower will contain 2^t particles. There will be roughly equal numbers electrons, positrons and photons, each with an average energy given by

$$E(t) = \frac{E_0}{2^t}. \tag{B.1}$$

Then, the cascade process will stop abruptly when $E(t) = E_C$. The thickness of absorber at which the cascade ceases, t_{Max} can be writen in terms of the initial and critical energies:

$$t_{Max} = \frac{\ln(E_0/E_C)}{\ln 2}. \tag{B.2}$$

The critical energy is the intersection between ionization and bremsstrahlung process, for Lead it is showed in the Figure B.1.

From the model, it is extracted that the maximum shower depth varies as the logarithm of the primary energy decribed by Equation B.2, as a feature that emerges from more sophisticated models of the process and is observed experimentally. It also predicts that the shower curve should rise rapidly to a peak value and the fall to zero.

The broad peak of the experimental curve can be interpreted in terms of a spread of energies of the incoming particles. Experiments also show that the curve does not eventually drop to zero, but instead has a long tail. The long tail can be interpreted as being due to muon interactions producing knock-on electrons capable of making a contribution to the cascade process [45].

Electromagnetic shower development is stochastic, but on average the longitudinal energy profile of the shower is given by a photon distribution,

$$\frac{dE}{dt} = Eb\frac{(bt)^{a-1}e^{-bt}}{\Gamma a}, \tag{B.3}$$

where t is the distance measured in units of radiation lengths, E is the initial energy and a and b are free parameters that can be empirically determined for each material.

The dE/dt distribution reaches its maximum when

$$t_{Max} = \frac{a-1}{b} = \mathrm{In}y + C, \tag{B.4}$$

where $y = E/E_c$ and $C = 0.5$ for electrons and $+0.5$ for photons. The critical energy, E_c, for carbon (Z=6) is 111 MeV according to the following empirical formula

$$E_c = \frac{800 \text{ MeV}}{Z + 1.2}. \tag{B.5}$$

For electrons in Carbon between 1 to 10 GeV, $y = E/E_c$ ranges from 9 to 100. b is nearly constant for a given detector material but has a slight dependence on y [45] that is shown in Figure B.5. For y values of 9 to 100, b ranges 0.64 to 0.7 for Carbon.

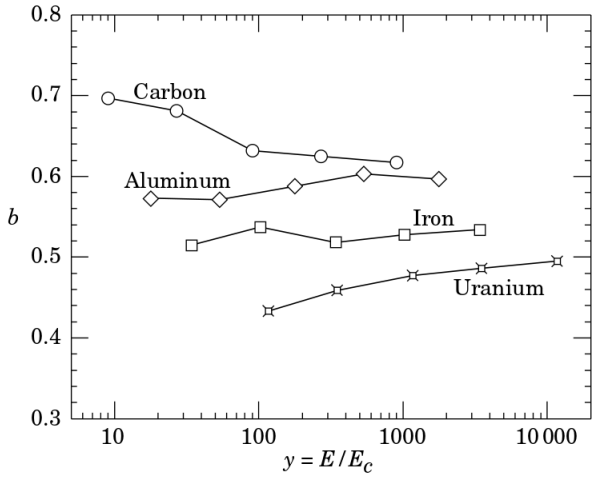

Figure B.5: b values for different materialas at different y ranges [7].

The dE/dx value at shower maximum ($t = (a-1)/b$) is

$$\left(\frac{dE}{dt}\right)_{Max} = \frac{Eb}{\Gamma a}\left(\frac{a-1}{e}\right)^{a-1}. \tag{B.6}$$

Define the vertex to shower maximum average slope as

$$\frac{(dE/dx)_{Max}}{x_{Max}} = \frac{Eb}{\Gamma a}\left(\frac{a-1}{e}\right)^{a-1}\frac{1}{t_{Max}X_0}. \tag{B.7}$$

The Figure B.6 shows a typical longitudinal energy profile for an electron shower. The figure was taken from the Reference 42.

Photon initiating shower development is shown schematically in Figure B.7. Note that the photon is not visible in the detector until it creates charged particles by pair production, or undergoes Compton scattering from atomic electrons.

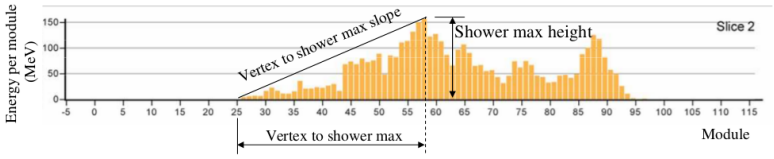

Figure B.6: Electron shower longitudinal energy profile [42].

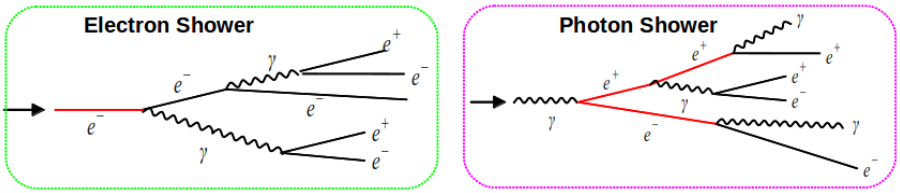

Figure B.7: Electron and photon shower longitudinal development profile.

If the interaction vertex is known, for example, by a muon track from $\nu_\mu CC$ reaction, and an electromagnetic shower starts at some measurable distance from the vertex and the shower direction points back to the vertex, it is almost certainly due to a photon.

For lateral shower containment, material differences are smaller than longitudinally. In addition, there is no energy dependence. A given long cylinder will thus contain the same fraction of the energy from 1 GeV electromagnetic showers as from 1 TeV ones.

For example, in Lead more than 40% of the shower energy is deposited by particles with energies below 1 MeV, while the critical energy is more than 7 MeV. Only one quarter of the energy is deposited by positrons, the rest by electrons.

This illustrates that Compton scattering and photoelectron production are very important processes for understanding calorimetry. Both processes dominate at energies far below the critical energy and are therefore not properly described by scaling variables such as X_0 and ρ_M [46].

Appendix C

Kinematic Constrain

The variables s, t, and u are, defined as follows:

$$s = (p_A + p_B)^2, \tag{C.1}$$

$$t = (p_A + p_C)^2, \tag{C.2}$$

$$u = (p_A - p_D)^2, \tag{C.3}$$

where p_A, p_B, p_C, and p_D are the 4-momentum vectors for the particles A, B, C, and D. Three variables are not independent. The are constrained by the next relation:

$$s + t + u = m_A^2 + m_B^2 + m_C^2 + m_D^2. \tag{C.4}$$

Using those equations, it is possible to apply over own reaction $\nu e \rightarrow \nu e$, where the $p_{/nu}$ and p_e represents the 4-momentum for the initial neutrino and electron, respetively. p'_ν and p'_e are the 4-momentum of neutrino and electron after the collision. And the Center of Mass (CM) frame, t is calculated as

$$t = (p_\nu + p'_e)^2, \tag{C.5}$$

$$t = 2p_\nu \cdot p'_e, \tag{C.6}$$

$$t = 2E_\nu + E'_\nu(1 - cos\theta'), \tag{C.7}$$

$$t = \frac{s}{2}(1 - cos\theta'). \tag{C.8}$$

Where θ' is the scattering angle in the CM frame. The electron rest mass was ignored, as the interesting scattering is highly relativistic, so $E_e >> m_e$.

The inelasticity y es defined as

$$y = \frac{p_B \cdot q}{p_B \cdot p_A}. \tag{C.9}$$

Here q is the 4-momentum transfer. If y is calculated at the lab frame, then

$$y = \frac{p_B \cdot (p_A - p_C)}{p_B \cdot p_A}. \tag{C.10}$$

Making the sustitution for the correspond 4-momentum:

$$y = \frac{(E_B, 0) \cdot (E_A - E_C, \mathbf{p}_A - \mathbf{p}_C)}{(E_B, 0) \cdot (E_A, \mathbf{p}_A)}, \tag{C.11}$$

$$y = \frac{E_B(E_A - E_C)}{E_B E_A}. = \frac{\nu}{E} \tag{C.12}$$

Here $\nu = E_\nu - E'_\nu$, where E_ν and E'_ν represent the initial and final neutrino energies. The physical meaning of the inelasticity is the energy loss fraction of incoming neutrino.

Now, using the Equation C.11 to determine the energy loss fraction at the CM frame

$$y = \frac{(E, -\mathbf{p}) \cdot (0, \mathbf{p} - \mathbf{p}')}{(E, -\mathbf{p}) \cdot (E, \mathbf{p})}, \tag{C.13}$$

$$y = \frac{\mathbf{p}) \cdot \mathbf{p}' - |\mathbf{p}|^2}{2E^2}, \tag{C.14}$$

$$y = \frac{cos\theta' - 1}{2}. \tag{C.15}$$

From equations C.8 and C.15

$$t = -sy. \tag{C.16}$$

With Equation C.3, u in the lab frame

$$u = (p_\nu - p'_e)^2. \tag{C.17}$$

Here p_ν is the incoming neutrino 4-vector, p'_ν is the neutrino 4-vector after collision, and p'_e is recoil electron 4-vector.

$$u = m_\nu^2 + m^2 e - 2\mathbf{p}_\nu \cdot \mathbf{p}'_e, \tag{C.18}$$

$$u = -2(E_\nu, \mathbf{p}_\nu) \cdot (E'_e, \mathbf{p}'_e), \tag{C.19}$$

$$u = -2(E_\nu E'_e - p_\nu p'_e cos\theta), \tag{C.20}$$

$$u = -2E_\nu E'_e(1 - cos\theta). \tag{C.21}$$

Due to that in the case where $E_e >> m_e$, so $s + t + u = 0$, and from the Equation C.16,

$$s + t = -u, \tag{C.22}$$

$$s(1 - y) = 2E_\nu E'_e(1 - cos\theta). \tag{C.23}$$

Using the Equation C.1,

$$s = ((E_\nu, \mathbf{p}_\nu) + (E_e, \mathbf{p}_e))^2, \tag{C.24}$$

$$s = -2(E_\nu E_e - p_\nu p'_e cos\theta), \tag{C.25}$$

$$s = 2m_e E_\nu. \tag{C.26}$$

So,

$$2m_e E_\nu(1 - y) = 2E_\nu E'_e(1 - cos\theta), \tag{C.27}$$

$$m_e(1 - y) = E'_e(1 - cos\theta). \tag{C.28}$$

Making the expansion for small dispersed angles

$$1 - cos\theta = 1 - \left(1 - \frac{\theta^2}{2!} + \frac{\theta^4}{4!} - ...\right) = \frac{\theta^2}{2}. \tag{C.29}$$

Now, an expression in a simple from

$$2m_e(1 - y) = E'_e\theta^2. \tag{C.30}$$

Where E'_e is the electron energy at the lab frame or recoil electron energy, θ is the recoil electron angle, m_e the electron rest mass, and y the inelasticity.

Since, the fraction energy loss by the neutrino, i.e. $0 < y < 1$

$$E\theta^2 = 2m_e. \tag{C.31}$$

$$2m_e(1 - y) = E'_e\theta^2. \tag{C.32}$$

Appendix D

Angle Beam Correction

The angle beam direction has big relevance in the Neutrino Electon Scattering, it is due to that the Q^2 and $E\theta^2$ variables have angular dependence, i.e a wrong beam angular direction will modify the limit of the cut and it could imply a wrong signal selection.

To get the angle beam direction in Medium Energy, the same process from Low Energy was followed, but this time selecting muons at more high energy, so the angle was determined using the ME Reconstructed Charged Current Inclusive (CInclusiveReco) Data and Monte Carlo samples.

The final sample used to determine the beam angle direction meets the typical CC Inclusive cuts: fiducial events, Total energy (neutrino energy) below 120 GeV, Muon energy between 30 GeV and 120 GeV, the events should match in MINOS Near Detector, Helicity (muon or anti-muon) cut and the dead time cut.

The Figure D.1 shows the beam angle direction distributions on x and y axis in the MINERνA Detector frame for ME data and MC, each plot covers a 100 MeV range of Neutrino Recoil Energy up to 500 MeV.

The Recoil Energy is defined by the Equation D.1

$$\nu_{RE} = E_{\nu} - E_{Lepton}. \tag{D.1}$$

On the plots from the Figure D.1 a Gaussian fit is applied to data and MC, with the mean and sigma indicated. The errors showed are statistical only.

The event samples corresponds only for the first year of Medium Energy run, i.e. minervame1A to minervame1D. Ideally it should have been used all the information from ME run an apply a more energetic requirement over the muons, but untill the moment just four playlist have been processed with the

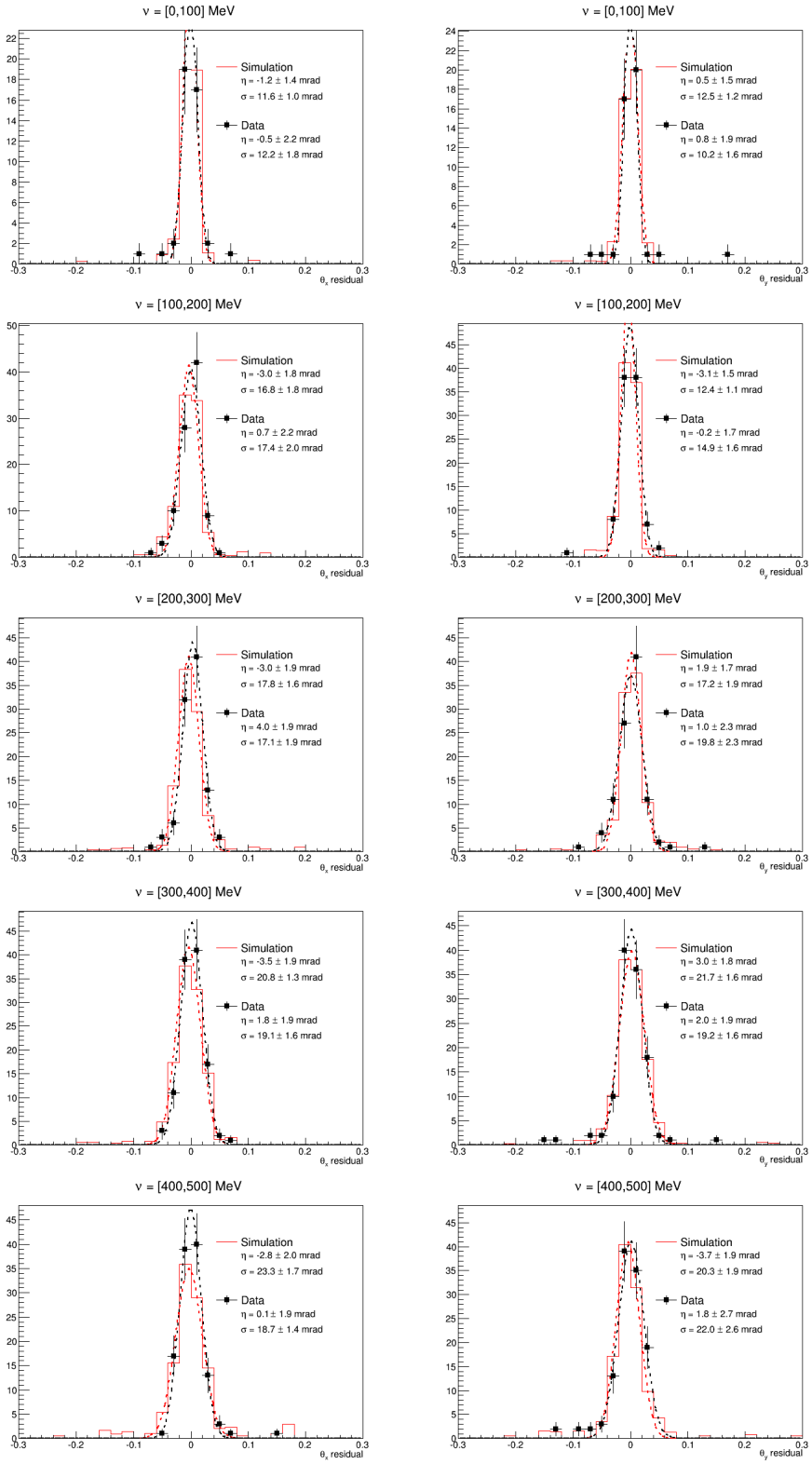

Figure D.1: Medium Energy beam angle direction measured in the MINERνA Detector coordinate system. For each one of the neutrino recoil energy bining.

	θ_X (mrad)	θ_Y (mrad)
Data	1.3520 $\pm$ 0.8957	0.9179 $\pm$ 0.9092
MC	-2.4797 $\pm$ 0.7799	-0.3316 $\pm$ 0.7439

Tabla D.1: ME beam angle direction at MINERνA Detector frame.

CC Inclusive machinery.

The mean and asociated error from the Gaussian fits in the Figure D.1 is shown in the plot D.2. If a horizontal line is fitted to the data and simulation, the angle beam direction is shown in the Table D.1.

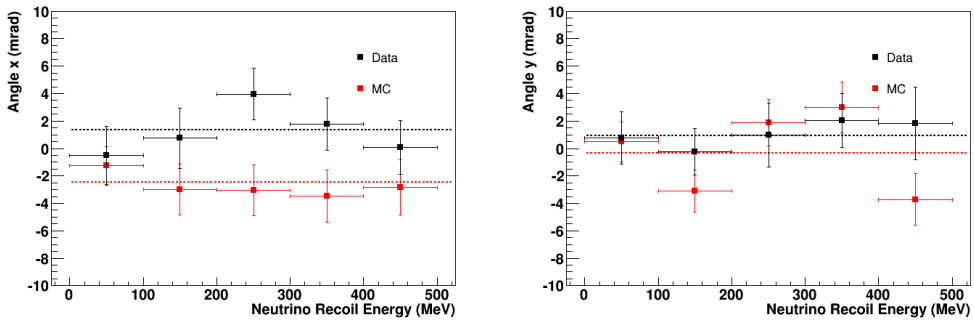

Figure D.2: ME bean mean direction for data and MC in x and y axis.

The physical meaning of the Figure D.2 is that these values corresponds to a bias in the data and simulation respect to the detector frame. To match the data with the prediction events, just the subtraction between directions should be made.

Those points are showed in the Figure D.3, and after applying a horizontal fit over those values, the angle beam correction (correction on bias) is -3.8944 ± 1.2089 mrad for angle in $x - axis$ and -1.2223 ± 1.1817 mrad in $y - axis$.

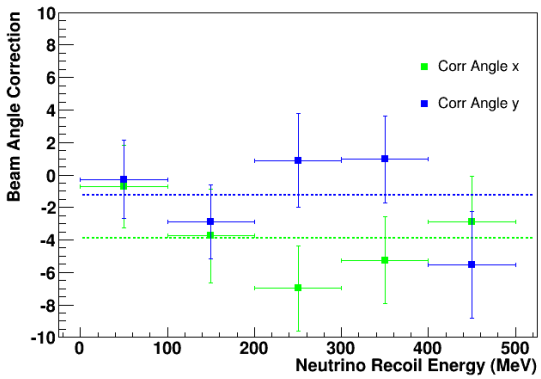

Figure D.3: Beam angle correction needed in Medium Energy to match the neutrino beam direction in Data with Monte Carlo.

Appendix E

Michel Electrons

The Michel Electron is produced by the decay of stopping muon (anti-muon) or from a decay chain of stopping $\pi^{\pm}$, as follows:

$$\mu^{+} \rightarrow \nu_{\mu} + \nu_{e} + e^{+}. \tag{E.1}$$

$$\mu^{-} \rightarrow \nu_{\mu} + \nu_{e} + e^{-}. \tag{E.2}$$

The response of the detector to Michel Electrons at different locations can provide a cross-check of the relative calibration. The overall electromagnetic energy scale can also be checked by comparing the Michel Electron spectrum in data and MC simulation.

In general a Michel Electron is identified by a delayed signal near the end-point of a stopped muon track. However, stopped muons or pions from neutrino interactions occurring in the detector also produce Michel Electrons.

Finding a Michel Electron from a short length stopped track is difficult since reconstruction of the short track is more challenging. Besides the difficulty of short track pattern recognition from small number of hits, the short track is often produced with a high angle where the track reconstruction is poor. Also, short stopped track may be spatially nearby other tracks from the same neutrino interaction [44].

Thus, it is difficult to match the Michel Electron with the end point of short tracks. But the event rate of unmatched Michel Electrons is higher than Michel Electrons from rock muons. It is found that the unmatched Michel Electron sample has very small background near the Michel Electron energy peak.

Thus, this unmatched Michel electron sample serves as a high statistics calibration sample. The Figure E.1 shows the comparisons between Data and MC

for each one of the Data playlist, instead the Monte Carlo sample corresponds just to the first playlist.

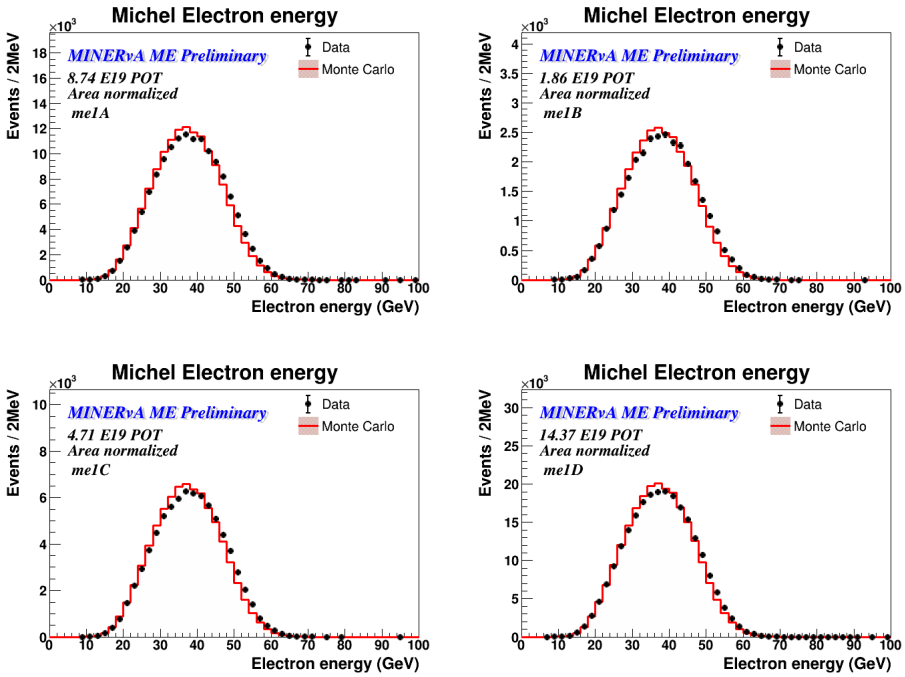

Figure E.1: Michel Electons energy distributions for each one of the Medium Energy Data playlists.

Another calibration cross-check between Data and MC is the Michel Electrons energy loss, in this case just to follows the the Neutrino Electon Scattering energy loss convention, there is energy loss in the first 4 planes at the begin of the Electromagnetic Shower, those distributions are showed in the Figure E.2.

The Figure E.3 shows the comparison between Data and Monte Carlo for all the Medium Energy playlists at the same time, the plots show a good agreement.

Using all the ME data sample is possible to get the Michel Energy and dE/dx time dependence for both samples; data and Monte Carlo, each point in the Figure E.4 corresponds to 1000 Michel Electron events taken over the time.

Applying a horizontal fit over the Michel Electrons energy and dE/dx time dependence points, is possible to get the mean value for this quantities over the time, i.e the energy and dE/dx stability. The Table E.1 shows the fitting parameters for Data and Monte Carlo.

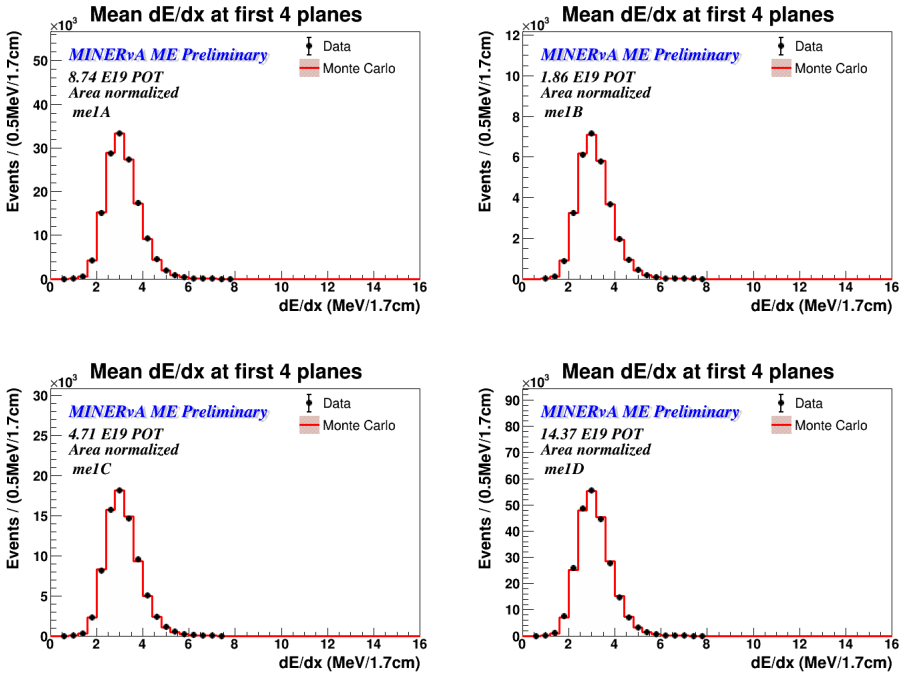

Figure E.2: Michel Electon energy loss in the first 4 planes for each one of the Medium Energy Data playlists.

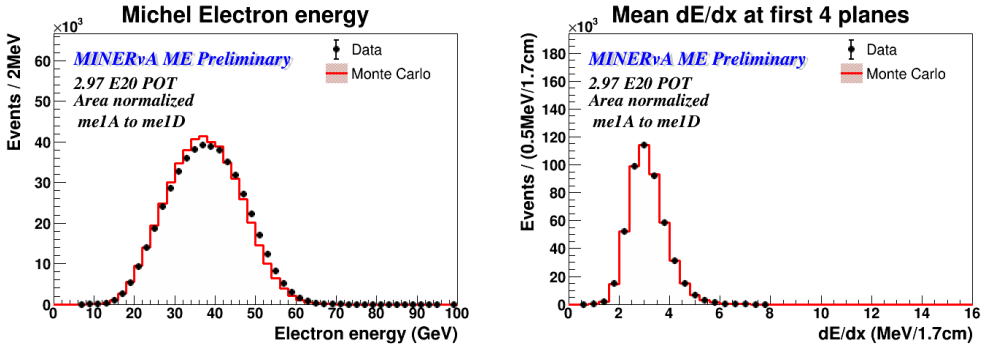

Figure E.3: Michel Electron energy and energy loss distributions for full ME Data sample.

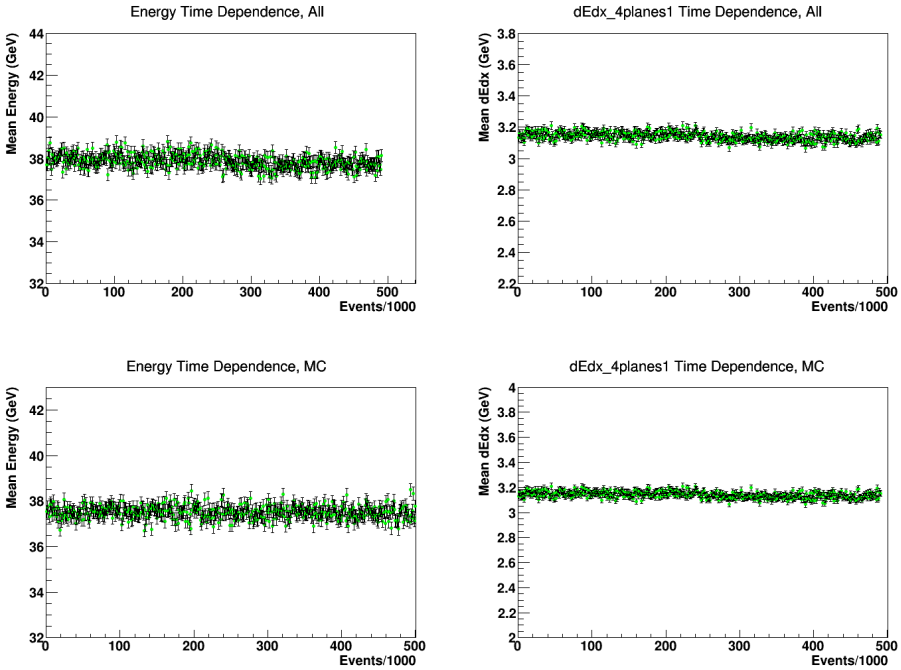

Figure E.4: Michel Electron energy and energy loss over the time for all the information available in Medium Energy run. The energy scale and energy loss is constant over the time, i.e. it is stable.

playlists	Energy [MeV]	dE/dx [Mev/1.7 cm]
Data		
me1A	37.979 ± 0.026	3.152 ± 0.002
me1B	37.957 ± 0.055	3.145 ± 0.006
me1C	38.029 ± 0.035	3.152 ± 0.003
me1D	37.725 ± 0.021	3.129 ± 0.002
Total		
All Data	37.981 ± 0.022	3.151 ± 0.002
All MC	37.532 ± 0.020	3.126 ± 0.002

Tabla E.1: Energy scale for Michel Electrons in Data and Monte Carlo Medium Energy samples.

Appendix F

The MINERνA Collaboration

Figure F.1: The MINERνA Collaboration at anual summer meeting, June 2015.

J. Felix, M.A. Ramirez, E. Valencia, G. Zavala
Universidad de Guanajuato

G. Tzanakos
University of Athens

J. Cravens, M. Jerkins, S. Kopp, J. Ratchford
University of Texas at Austin

D.A. Martinez Caicedo, M.F. Carneiro, C.M. Castromonte, H. da Motta, G.A. Fiorentini, A. Ghosh, K. Hurtado, J.L. Palomino, H. Yepes?Ramirez
Centro Brasileiro de Pesquisas Físicas

D.W. Schmitz
University of Chicago

J. Mousseau, B. Osmanov, H. Ray, D. Rimal, M.Wospakrik
University of Florida

L. Bellantoni, M. Betancourt, D. Boehnlein, R. DeMaat, N. Grossman, D.A. Harris, M. Kiveni, J.G. Morf\'{i}n, J. Osta, E. A. Paschos, G.N. Perdue, L. Rakotondravohitra, P. Rubinov, E.L. Snider, J.T. Sobczyk, R. Stefanski
Fermilab

A. Bravar, Y. Karadzhov
University of Geneva

M.E. Christy, M. Datta, C.E. Keppel, W. Tan, T. Walton, L. Y. Zhu
Hampton University

A. Butkevich, S.A. Kulagin
Inst. Nucl. Reas. Moscow

G. Niculescu, I. Niculescu
James Madison University

E. Maher
Mass. Col. Lib. Arts

L. Fields, B. Gobbi, J.A. Hobbs, C.E. Patrick, L. Patrick
Northwestern University

H. Schellman
Oregon State University

N. Tagg
Otterbein University

S. Boyd, S.A. Dytman, B. Eberly, Z. Isvan, C.L. McGivern, B. Messerly, D. Naples, V. Paolone, L. Ren
University of Pittsburgh

M. J. Bustamante , E. Endress, A.M. Gago, S.F. Sánchez , J.P. Vel\'{a}squez
Pontificia Universidad Catolica del Peru

R. Napora
Purdue University Calumet

S. Avvakumov, A. Bercellie, A. Bodek, R. Bradford, H. Budd, J. Chvojka, M. Day, G.A. D\'{i}az , R. Fine, T. Golan, A. Gomez, A. Higuera, J. Kleykamp, H. Lee, L. Loiacono, S. Manly, C.M. Marshall, K.S. McFarland, A.M. McGowan, A. Mislivec, J. Park, P.A. Rodrigues, D. Ruterbories, J. Wolcott
University of Rochester

T. Le, R.D. Ransome, E.C. Schulte, B.G. Tice
Rutgers University

O. Altinok, H. Gallagher, T. Kafka, W.A. Mann, W. P. Oliver
Tufts University

C. Simon, B.P.Ziemer
University of California at Irvine

J. Demgen, R. Gran, M. Lanari, E. Miltenberger
University of Minnesota at Duluth

G. Salazar, C.J. Solano Salinas
Universidad Nacional de Ingeniería

Nuruzzaman, W.K. Brooks, R.Galindo, G. Maggi, J. Miller, C. Pe\~{n}a
Universidad Técnica Federico Santa María

L. Aliaga, J. Devan, M. Kordosky, J.K. Nelson, A. Norrick, J. Walding, D. Zhang
College of William and Mary

Bibliography

[1] M.K. Sundaresan, Handbook of Particle Physics, CRS Press, (2001) USA.

[2] D. K. Perkins, Introduction to High Energy Physics, Addison Wesley (2000) USA.

[3] W. R. Frazer, Elementary Particles, Prentice Hall (1966) USA.

[4] http://www.cobra-experiment.org/

[5] Celebrating the Neutrino, Los Alamos Science 25, 1 (1997).

[6] Fayyazuddin and Riazuddin, A Modern Introduction to Particle Physics, 2nd Edition, World Scientific Publishing, (2000), Singapore.

[7] F. Halzen, Quarks and Leptons: An Introduction Course in Modern Particle Physiscs, John Wiley and Sons, (1984) USA.

[8] Yung-Kuo Lim, Problems and Solutions of Atomic, Nuclear and Particle Physics, World Scientific, (2000), Singapore.

[9] Aram Kotzinian, 2004 Theory.

[10] Particle Data Group, Phys. Lett. B, 592 (2004).

[11] Arfken and Weber, Mathematical Methods for Physicists, 5th Edition, Harcourt/Academic Press (2001) USA.

[12] J. Félix, Acta Universitaria, 17, 2, 28 (2007).

[13] G. 't Hooft, Phys. Letters 37B (1971) 195.

[14] F. J. Hasert et al, Phys. Rev B 46 (1973) 121.

[15] J. A. Formaggio et al, Rev. Mod. Phys. 84 (2012) 1307.

[16] W.J. Marciano et al, J. Phys. G: Nucl. Part. Phys. 29 (2003) 2629.

[17] H. J. Steiner, Phys. Rev. Letters Vol 24, Num 13, (1970) 746.

[18] L. M. Sehgal, Nucl. Phys. B70, (1974) 61.

[19] P. Vogel and J. Engel, Phys. Rev. D, Vol 39, Num 11, (1989) 3378.

[20] P. Vilian, CHARM II Collab. Nucl. Phys. B 19, (1991), 306.

[21] P. Vilian et al, CHARM II Collab. Phys. Lett. B 281 (1992), 159.

[22] P. Vilian et al, CHARM II Collab. Phys. Lett B 302 (1993) 351.

[23] G. Radel et al, (to appear in Mod. Phys. Lett A).

[24] P. vilian et al, CHARM II Collab. Phys Let B 335 (1994) 246.

[25] R. Imlay et al, J. Phys. G: 29 (2003) 2647.

[26] A. Gouvea et al, Phys. Rev. D 74 (2006) 033004.

[27] M. Deniz et al, TEXONO Collab. arXiv:0810.0809v1 [hep-ex] 6 Oct 2008.

[28] L.B. Auerbach et al, LSND Collab. arxiv:hep-ex/0101039v1 22 Jan 2001.

[29] Fermilab, Joint Experimental - Theoretical Seminar, December 20, 2013. Direct Measurement of the NuMI Flux with Neutrino-Electron Scattering in MINERvA.

[30] http://www-numi.fnal.gov/

[31] L. J. Loiacono, Measurement of the Muon Neutrino Inclusive Charged Current Cross Section on Iron Using the MINOS Detector. PhD thesis, The University of Texas at Austin. FERMILAB-THESIS-2010-71.

[32] D. G. Michaels et al., MINOS Collaboration Nucl. Instr. and Meth. A596 (2008) 190.

[33] S. E. Kopp, "Accelerator neutrino beams", Phys. Rept. 439 (2007) 101â159, arXiv:physics/0609129.

[34] S. E. Kopp et al, Nucl. Instr. Meth. A 568 (2006) 503â519.

[35] The Minerva collaboration,The Minerva Technical Design Report, Version 1.3, (2006).

[36] B. G. Tice, Measurement of Nuclear Dependence in Inclusive Charged Current Neutrino Scattering. PhD Thesis, FERMILAB-THESIS-2014-01.

[37] B. M. Eberly, Characterization of Final State Interaction Strength in Plastic Scintillator by Muon-Neutrino Charge, Pittsburgh University, FERMILAB-THESIS-2014-18.

[38] A. Higuera-Pichardo, Search for Charged Current Coherent Pion Production by Muon-Neutrino in the MINERνA Experiment, PhD Thesis, Universidad de Guanajuato.

[39] E. Valencia-Rodriguez, Estudio, Simulación y Caracterización del Espectrómetro Magnético del Experimento MINERvA (FNAL E-938), Ms Thesis, Universidad de Guanajuato.

[40] Nucl.Instrum.Meth. A789 (2015) 28-42.

[41] G. N. Perdue et al, Nucl. Instr. and Meth A694 (2012) 179.

[42] J.Park, MINERvA Technical Note No. 041, DocDB document 9407.

[43] J. Park Electromagnetic Final states in MINERνA.

[44] J. Park, Neutrino-Electron Scattering in MINERνA for Constraining the NuMI Neutrino Flux, PhD Thesis, FERMILAB-THESIS-2013-36.

[45] V. S. Kaushik, Electromagnetic Showers and Shower Detectors, Internal Documents, University of Texas at Arlington.

[46] Richard Wigmans, Calorimetry, 2003 ICFA Instrumentation School Proceeding.

[47] Hadronic Shower, http://rkb.home.cern.ch/rkb/PH14pp/node80.html

[48] Nucl. Inst. and Meth. A743 (2014) 130.

[49] R. Zwaska et al, Instrum. Meth. A 568 (2006) 548â560.

[50] S. M. Bilenky, "Neutrino. History of a unique particle", arXiv:1210.3065.

[51] A. de Gouvea et al, "Neutrinos", arXiv:1310.4340.

[52] Zhin-Zhong Xing, "Neutrino Physics", 1st Asia-Europe-Pacific School of High-Energy Physics, arXiv:1406.7739.

[53] http://arxiv.org/abs/1509.05729.